Universidad de Valparaíso
CHILE
Doctorado en Ciencias mención
Biofísica y Biología Computacional

Facultad de Ciencias

THE VOLTAGE SENSOR OF THE VOLTAGE-GATED PROTON CHANNEL (H_V1)

Tesis entregada a

LA UNIVERSIDAD DE VALPARAÍSO

en Cumplimiento Parcial de los requisitos para optar al grado de
Doctor en Ciencias con Mención en Biofísica y Biología Computacional

Facultad De Ciencias

Por
Emerson Mauricio Carmona Rojas
Agosto, 2020

Dirigida por:
Carlos González León y Ramón Latorre de la Cruz

Universidad de Valparaíso
CHILE
Doctorado en Ciencias mención Biofísica y Biología Computacional

Facultad de Ciencias

FACULTAD DE CIENCIAS
UNIVERSIDAD DE VALPARAÍSO

INFORME DE APROBACION
TESIS DE DOCTORADO

Se informa a la Facultad de Ciencias que la Tesis de Doctorado presentada por:

EMERSON CARMONA ROJAS

Ha sido aprobada por la comisión de Evaluación de la tesis como requisito para optar al grado de Doctor en Ciencias con mención en Biofísica y Biología Computacional, en el examen de Defensa de Tesis rendido el 13 de agosto de 2020

Director/a de Tesis:

Dr.
Carlos González León .....

Co-Director de Tesis:

Dr.
Ramón Latorre de la Cruz .....

Comisión de Evaluación de la Tesis

Dr.
Osvaldo Álvarez Araya .....

Dr.
Alan Neely .....

Dr.
Francisco Bezanilla .....

AGRADECIMIENTOS

Tengo que agradecer a muchas personas que me han ayudado y de las que he aprendido durante esta etapa de mi formación. Tengo que comenzar por agradecer a mi familia, que desde el comienzo de esta aventura me ha apoyado. A mi madre, María Rojas, por enseñarme desde muy pequeño que en la vida debes seguir tus sueños, y perseverar a pesar de las adversidades. A ti te debo todo lo que soy, no solo en la ciencia, sino también a nivel personal. A Alejandro Miranda, que es parte muy importante de mi familia, y se ha convertido en un padre para mí. Gracias por todo el soporte que nos has dado. A mi hermano, Edgard Carmona, gracias por tu alegría y por compartir tu tiempo conmigo, a pesar de la distancia y de lo ocupado que siempre estás. Aunque eres mi hermano menor, he aprendido y sigo aprendiendo muchas cosas de ti.

Sin lugar a duda, tengo que agradecer a todos los mentores que he tenido la oportunidad de conocer durante esta larga aventura que es la formación científica. A mi querido profesor de química, Oscar Rozas, que me hizo finalmente decidir dedicarme a hacer ciencia como mi profesión. A Juan Reyes, que me recibió en su laboratorio y fue mi mentor durante mi pregrado. Juan y José Pino fueron los científicos con los que di mis primeros pasos en investigación, con lo que confirmé que era esto lo que quería hacer el resto de mi vida. Por supuesto, tengo que agradecer especialmente a Carlos González, mi tutor de tesis. Gracias por toda la paciencia, por todas las enseñanzas, y por toda la locura que aportaste a mi formación. Gracias por todo el apoyo y las oportunidades que me han permitido estar terminando esta etapa hoy, y con las que afrontaré los siguientes desafíos. Agradezco también a Osvaldo Álvarez, un gran maestro del que he aprendido mucho y admiro profundamente, tanto por su calidad científica como humana. Gracias a Alan Neely, por sus enseñanzas en el área de los

modelos y simulaciones, pero por sobre todo por sus consejos y conversaciones, que valoro tremendamente. Tengo que agradecer también a Ramón Latorre, que ha sido y seguirá siendo una inspiración al decidir regresar a Chile y participar de la formación de tantos biofísicos chilenos, de los que me siento muy orgulloso de pertenecer. Gracias a Francisco Bezanilla por haber aceptado ser parte de mi comisión de tesis, y por ser también una fuente de inspiración por su excelente ciencia y su infinita energía y entusiasmo. Agradezco con mucho cariño a Luis Cuello y (Doris) Marien Cortés, que me recibieron en su laboratorio durante mi pasantía doctoral y con los que emprenderé el siguiente paso de mi formación científica. Gracias a ambos por todo lo que me enseñaron de ciencia y de la vida en esos meses de estadía. Gracias a Peter Larsson que, aunque no fue parte de mi comisión de tesis, aportó muchas enseñanzas a mi formación. También agradezco a los biofísicos más jóvenes que aportaron a mi formación. Para mí, ellos son parte del futuro de la ciencia chilena, entre los que tengo que destacar a José Antonio Gárate y Christian Wilson.

Finalmente, no puedo olvidar a los grandes amigos que he tenido la oportunidad de conocer durante estos años, y que agradezco a la vida haberme encontrado y seguir haciéndolo, y que lamentablemente no tengo espacio suficiente para nombrarlos a todos. Tengo que destacar a los que además son mis colegas latinoamericanos, Marcelo Ozu, Natalia Calienni, Miguel Cuaxospa, Richard García, Gustavo Scanavachi, Ludmila Leroy y Gretchen Macias, con los que espero poder trabajar en el futuro para enaltecer la biofísica latinoamericana.

Incuestionablemente, lo más importante en esta etapa, como cualquier otra en la vida, son las personas con las que nos encontramos.

INDEX

LIST OF TABLES

LIST OF FIGURES

ABBREVIATION LIST

CiH_v1: *Ciona intestinalis* voltage-gated proton channel

DNA: deoxyribonucleic acid

ΔpH: $pH_{out} – pH_{in}$

EGTA: ethylene glycol-bis(β-aminoethyl ether)-N,N,N′,N′-tetraacetic acid

G-V: conductance versus voltage

HEPES: 4-(2-hydroxyethyl)-1-piperazineethanesulfonic acid

HEPBS: N-(2-Hydroxyethyl)piperazine-N'-(4-butanesulfonic acid)

H_v1: voltage-gated proton channel

hH_v1: human voltage-gated proton channel

MCMC: Markov chain Monte Carlo

MES: 2-(N-morpholino)ethanesulfonic acid

MTS: methanethiosulfonate

NADPH: reduced nicotinamide adenine dinucleotide phosphate

NMDG: N-methyl-D-glucamine

NMR: nuclear magnetic resonance

NOX: NADPH oxidase

PCR: polymerase chain reaction

P_{H^+}: permeability to protons

pH_{in}: internal pH

pH_{out}: external pH

PKC: protein kinase C

PMA: 12-myristate 13-acetate

P_{Na^+}: permeability to sodium

Q-V: charge versus voltage

RNA: ribonucleic acid

VSP: voltage-sensing phosphatase

VSD: voltage sensor domain

VSOP: voltage-sensor domain-only protein

VCF: voltage-clamp fluorometry

NOTE TO THE READER

This thesis's principal objective was to gain further understanding of how the voltage-gated proton channel (H_v1) works. I approached this broad question studying in detail the H_v1 voltage sensor domain (VSD). I studied how the VSD is coupled with the permeation pathway and the pH sensor. Coupling is especially interesting in H_v1 since all these processes are contained in the same structural domain. My thesis is divided into four chapters. In chapter 1, I introduced the H_v1 protein, including a history of its discovery and recent advances in the field, its physiological importance, and a summary of its structure and biophysical properties (chapter 1). The next chapter contains the first half of my thesis, which consisted in the study of the coupling between the voltage sensing and permeation pathway opening (chapter 2). Then, I focused on the second half of my work involving the coupling between the voltage and pH sensors (chapter 3). Finally, I discussed the general conclusions obtained from all the results of this thesis (chapter 4). I decided to separate the thesis in four independent chapters to give you the possibility to read them separately. Therefore, each chapter can be understood without having to read the entire thesis. Despite this, the thesis is not a compendium of isolated chapters, since the initial introduction (chapter 1) and the general discussion and conclusions (chapter 4) unify them. However, they can also be read independently. I thought this would be useful for the reader who is only interested in a section of the thesis.

Finally, I have to mention that chapter 2 produced a published paper attached at the end of the thesis. Chapter 3 produced a manuscript that will be submitted soon after the public presentation of this thesis. Additionally, at the end of the thesis, I attached a book chapter with the detailed methodology of oocytes extraction and treatment.

CHAPTER 1

VOLTAGE-GATED PROTON (H_V1) CHANNEL HAS UNIQUE BIOPHYSICAL PROPERTIES

1.1 Historical background

The history of discoveries in science is always an exciting part of the scientific work, and this is not the exception for the case of voltage-gated proton channel (H_v1). Although the existence of voltage-gated proton currents was initially proposed to explain the initiation of the bioluminescence emission in dinoflagellates (Fogel and Hastings, 1972), their first measurement was made ten years later (Thomas and Meech, 1982). In this beautiful work, the authors inserted four electrodes in snail neurons to measure the membrane potential and the intracellular pH, to inject current to voltage-clamp the membrane, and to inject HCl to control the intracellular pH (Thomas and Meech, 1982). Following this work, currents were measured in axolotl immature oocyte of the urodele amphibian *Ambystoma* (Barish and Baud, 1984) and molluscan neurons (Mahaut-Smith, 1989b). These voltage-dependent currents were characterized in these systems and showed similar properties: they were highly selective to protons, blocked by zinc and other divalent cations, and affected by both internal and external pH (Barish and Baud, 1984; Byerly et al., 1984; Mahaut-Smith, 1989a). Interestingly, during this decade, it was proposed that human neutrophils NADPH oxidase (NOX) activity was associated with a proton channel, which currently is one of the best characterized physiological roles of H_v1 (Henderson et al., 1987). In 1991 the first reported voltage-gated proton currents in rat alveolar epithelial cells appeared (DeCoursey, 1991), demonstrating that these currents were also present in mammals. Currents had the same characteristics described previously, although a notable difference was their much slower kinetics of activation and

deactivation compared with previous recordings in invertebrates. DeCoursey (1991) proposed for the first time that the presence of an unknown channel produced the voltage-gated proton currents. After this publication, there were a series of reports of proton currents in different cells, including macrophages, neutrophils, eosinophils, lymphocytes, and skeletal muscle (Bernheim et al., 1993; Cherny et al., 2003; DeCoursey and Cherny, 1993, 1994; Demaurex et al., 1993a; Demaurex et al., 1993b; Gordienko et al., 1996; Kapus et al., 1993; Klee et al., 1999; Krause et al., 1993; Schilling et al., 2002; Schrenzel et al., 1996). During the next years, an exciting discussion involving voltage-gated proton currents began. It was known that NOX, a membrane protein able to produce superoxide radicals, required of a mechanism able to dissipate the pH gradient produced by the enzyme and accumulation of intracellular protons after NADPH oxidation. Several groups proposed that the most effective mechanism to dissipate a proton gradient to the cell quickly would be a proton channel (Cherny et al., 2001; DeCoursey et al., 2000; Henderson et al., 1987, 1988; Morgan et al., 2005). However, the molecular identity of this channel was unknown. There were two proposals for this channel. In the first one, it was postulated that one of the subunits of NOX, $gp91^{phox}$, was the proton channel (Henderson, 2001; Henderson and Meech, 2002; Maturana et al., 2001; Murillo and Henderson, 2005). The second proposal involved a new protein that had this function and accompanied NOX while it produced superoxide (DeCoursey et al., 2001a; DeCoursey et al., 2001b; DeCoursey et al., 2000; DeCoursey et al., 2003). This controversy finally came to an end when the *HVCN1* gene coding for the H_v1-forming channel protein was discovered simultaneously by two groups in human, mouse, and *Ciona intestinalis* (Ramsey et al., 2006; Sasaki et al., 2006). This critical discovery allowed demonstrating that this new protein was responsible for producing the voltage-gated proton currents, and the channel that accompanied NOX activity (Okochi et al., 2009; Ramsey et al.,

2009). Additionally, this made it possible to study the physiological role of the channel by deleting it in model organisms and the channel structure to understand the molecular mechanisms of H_v1 functioning.

1.2 Physiology

The best described physiological function of H_v1 is to maintain the superoxide production by NOX in immune cells (Capasso, 2014; DeCoursey, 2013; Fernandez et al., 2016). NOX reduces molecular oxygen to produce superoxide radicals. Its activity requires the oxidation of NADPH coenzyme, which produces two intracellular protons (**Figure 1.1**). Additionally, the enzyme is electrogenic, so its activity depolarizes the membrane (Henderson et al., 1987, 1988). Both, acidification of the cytosol and depolarization of the membrane, inhibit the NOX activity (DeCoursey et al., 2003; Morgan et al., 2005) and increase the open probability of H_v1 (Cherny et al., 1995). Therefore, H_v1 is required for the sustained activity of NOX (Okochi et al., 2009; Ramsey et al., 2009) (**Figure 1.1**). This dependence is reinforced by an “enhanced activity” of H_v1 when activators of NOX, such as 12-myristate 13-acetate (PMA), are applied. This increase in activity is mainly caused by phosphorylation of a threonine residue (T29) in the N-terminal domain of the human H_v1 (hH_v1) by protein kinase C (PKC) (Morgan et al., 2007; Musset et al., 2010). NOX is a crucial enzyme in the elimination of pathogens. Therefore, it is not surprising that H_v1 is highly expressed in NOX expressing cells of the innate immune system including macrophages, neutrophils, and eosinophils (DeCoursey and Cherny, 1993; Gordienko et al., 1996; Kapus et al., 1993; Schrenzel et al., 1996). Additionally, H_v1 knockout mice presented immune disorders (Levine et al., 2015; Okochi et al., 2009; Ramsey et al., 2009; Sasaki et al., 2013; Zhu et al., 2013).

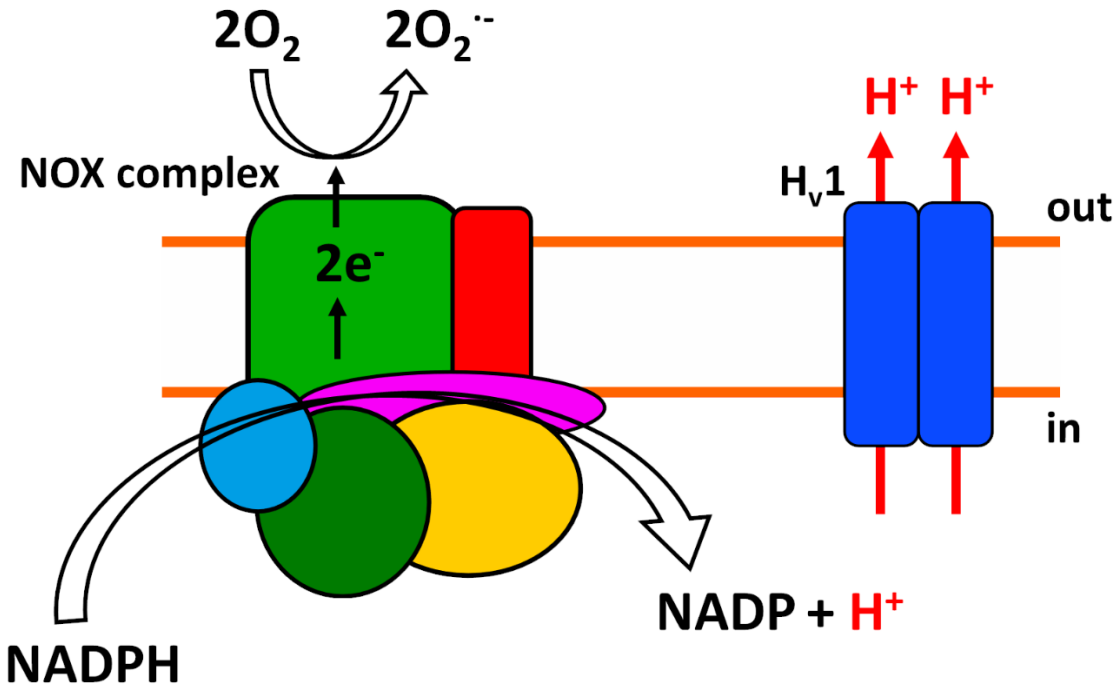

Figure 1.1. NADPH oxidase requires H_v1 to sustain its function. Schematic cartoon showing the NADPH oxidase (NOX) complex enzymatic reaction (left). In this case, NOX2 is represented, which is composed of six subunits. Cytosolic NADPH is oxidized to reduce extracellular molecular oxygen (O_2) to superoxide ($O_2^{\cdot-}$). This reaction increases the concentration of intracellular protons (red), which acidifies the cytosol and depolarizes the membrane. Then, H_v1 is activated, dissipating the proton gradient.

Although the function of H_v1 in most cells of the innate immune system involved the presence of NOX, this is not the case with basophils. These non-expressing NOX cells contain H_v1, which is activated by PKC when basophils are stimulated to release histamine (Musset et al., 2008). Dendritic cells, the antigen-presenting cells of the immune system, also expressed H_v1 and NOX, but the physiological role of the channel in these cells is still unknown (Rybicka et al., 2012; Szteyn et al., 2012). Cells of the adaptive immune system also expressed H_v1. Both B and T lymphocytes expressed H_v1 and NOX (Capasso, 2014), but proton currents in B lymphocytes are higher than in T lymphocytes. Interestingly, the activation of NOX with PMA increased H_v1 currents in T lymphocytes but decreased them in B lymphocytes (Schilling et al., 2002). In B

lymphocytes, H_v1 activity is important for efficient B cell antigen receptor activation (Capasso et al., 2010), but the role of H_v1 in T lymphocytes is still unknown. Although most of the description of the physiological role of H_v1 has been done in the immune system, several other tissues also expressed the channel.

H_v1 is expressed in the brain, specifically in microglia (Klee et al., 1999; Tian et al., 2016; Wu et al., 2012; Yu et al., 2018). Microglia are the brain resident immune cells, so it is not unexpected to find H_v1 associated with NOX in these cells. Although the physiological importance of this system is still not well understood, it has been demonstrated that the inhibition or absence of H_v1 during ischemic stroke reduces damage to neurons in the brain due to the reduction of the production of reactive oxygen species by NOX (Tian et al., 2016; Wu et al., 2012). In the lungs, H_v1 is expressed in alveolar epithelial cells, where the first measurements of voltage-gated proton channels in mammals were done (DeCoursey, 1991). H_v1 is involved in pH regulation and acid secretion to the airway surface liquid in the apical membrane of the cells, although other proteins contribute to this last process (Cho et al., 2009; Fischer et al., 2002; Iovannisci et al., 2010; Murphy et al., 2005). It has been proposed that alkalinization of the extracellular space would be the activator of H_v1 in these cells (Fischer, 2012). Another physiological role of H_v1 involves reproduction. Sperm and oocytes express the channel, but the role in oocytes is still not well understood (Smith et al., 2019). In human spermatozoa, on the other hand, it has been demonstrated that H_v1 is activated to increase the intracellular pH as an early step of capacitation (Lishko et al., 2010). The pancreas is another organ that expressed H_v1, which is located in the insulin-secreting β-cells (Zhao et al., 2015). The absence of H_v1 decreases insulin secretion and causes diet-induced obesity, hyperglycemia, and glucose intolerance in knockout mice (Pang et al., 2020a; Pang et al., 2020b), which makes the channel a possible therapeutic target for these types of metabolic diseases.

Finally, H_v1 is important in cancer. A variety of leukemia cell lines overexpress H_v1 or enhance the channel currents (Asuaje et al., 2017; Hondares et al., 2014). Additionally, it is overexpressed in glioma cell lines, breast cancer, and colorectal cancer (Morgan et al., 2015; Wang et al., 2011; Wang et al., 2013a). Inhibition of the channel pharmacologically or by decreasing its expression has been correlated with a reduction in cell proliferation, cancer metastasis and tumor growth along with an increase in cell death by apoptosis (Asuaje et al., 2017; Morgan et al., 2015; Wang et al., 2011; Wang et al., 2012; Wang et al., 2013a; Wang et al., 2013b). Therefore, H_v1 has been proposed as a promising pharmacological target to treat cancer (Fernandez et al., 2016). However, a better understanding of the molecular mechanisms of H_v1 functioning is needed to take full advantage of its future therapeutic applications.

1.3 Structure

In 2006, two groups simultaneously reported the discovery of the gene in *Ciona intestinalis*, mouse, and human (Ramsey et al., 2006; Sasaki et al., 2006). The gene was discovered by sequence alignment with the voltage-sensing phosphatase (VSP). This transmembrane protein contains a voltage sensor domain that regulates the intracellular phosphatase activity of the protein (Murata et al., 2005). H_v1 contains a voltage sensor domain (VSD) of four transmembrane segments (S1 to S4) like VSP and other voltage-gated ion channels (**Fig. 1.2a**). Although they share some structural characteristics, the identity of the VSDs of H_v1 and VSP is low, with a 23% between *Ciona intestinalis* H_v1 (CiH_v1) and VSP, and a 20% between hH_v1 and *Shaker* potassium channel. The most striking feature of H_v1 structure was the absence of a pore domain (S5 and S6) present in other voltage-gated ion channels (Catterall, 1995), which is the reason why it was also called voltage-sensor domain-only protein (VSOP). In the S4 transmembrane segment, H_v1 has three conserved arginines (R205, 208, and 211 in hH_v1; R255, 258, and 261 in

CiH_v1) followed by an asparagine (**Figure 1.2a**). These positively charged residues are responsible for the voltage sensitivity of the channel (Gonzalez et al., 2013). Another conserved residue in H_v1 VSD is an aspartate in S1 (D112 in hH_v1 and D160 in CiH_v1). This aspartate residue is known as the selectivity filter of H_v1 because when it is mutated, the channel loses its selectivity for protons (Berger and Isacoff, 2011; Musset et al., 2011). Additionally, H_v1 has an intracellular N-terminal domain that is heterogeneous in length and sequence between species. The function of this domain in the protein and its physiological role is still poorly understood. However, it is known that in hH_v1, the threonine 29 is a phosphorylation site for PKC related with the activation of the channel by activators of NOX (Musset et al., 2010). Additionally, a short hH_v1 isoform with a deletion of the first 20 amino acids has a higher response to NOX activators and lesser interaction with B-cell receptors than the wild-type channel (Hondares et al., 2014). Another modification of the N-terminal domain includes a post-transcriptional cleavage of the first 68 amino acids, resulting in a channel with altered pH dependence (Berger et al., 2017). Finally, the C-terminal domain of H_v1 forms a coiled-coil structure (Fujiwara et al., 2012; Li et al., 2010), which is important for the association between subunits to form the native dimeric channel (Lee et al., 2008) (**Figure 1.2b**).

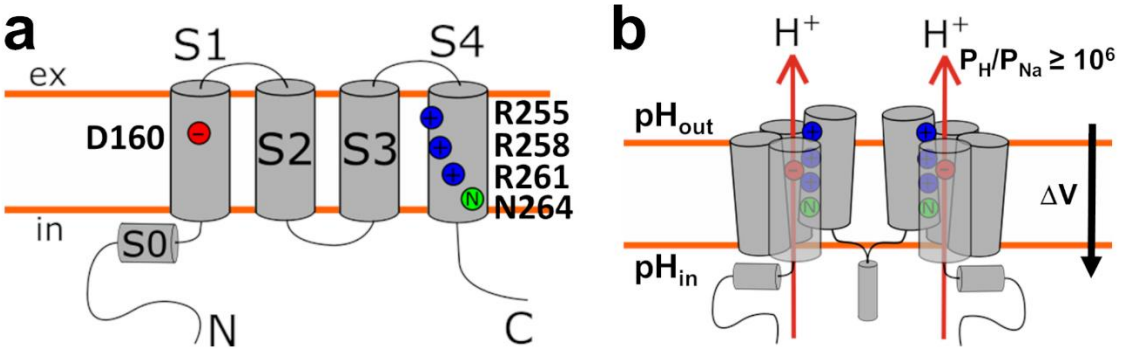

Figure 1.2. General structure and properties of H_v1. (A) Schematic cartoon showing the general structure of H_v1. Amino acid numbers correspond to *Ciona intestinalis* H_v1, showing the selectivity filter D160 is S1, the three gating charges (R255, R258, and R261) and the asparagine 264 in S4. (B) Schematic cartoon showing the

native H_v1, which is a dimer formed by a coiled-coil structure in the C-terminal domain. Protons permeate by each subunit showing a high selectivity over protons (permeability for protons over sodium, P_H/P_{Na} greater than 10^6). The channel is activated by depolarization (ΔV) and changes in the intracellular and extracellular pH (pH_{in} and pH_{out}, respectively).

The unique structure of the H_v1 channel has associated its biophysical properties (**Fig. 1.2b**). The opening of the dimeric channel is cooperative, so both VSDs have to be activated to open each subunit's permeation pathways (Gonzalez et al., 2010; Tombola et al., 2010). The channel has a very small unitary conductance, so the analysis of single-channel currents has been unsuccessful (Cherny et al., 2003). Additionally, H_v1 is highly selective to protons with a $P_{H+}/P_{Na+} \geq 10^6$ (Cherny et al., 1995). The permeation pathway and molecular mechanism of permeation are unknown, although there is one conducting pathway in each subunit of the channel. Monomeric channels with deletions in the N- and C-terminal domain still maintains its permeation properties (Koch et al., 2008). Finally, the H_v1 opening is voltage- and pH-dependent (Cherny et al., 1995). Although the voltage sensitivity is similar to other VSDs, involving an outward movement of the S4 along with the three arginine residues (Gonzalez et al., 2013; Qiu et al., 2013), the molecular mechanisms of pH sensitivity is still not well understood (DeCoursey, 2018). As it will be exposed in the next chapters, despite the relative simplicity of the H_v1 structure, the channel gating is unexpectedly complex.

1.4 References

Asuaje, A., Smaldini, P., Martin, P., Enrique, N., Orlowski, A., Aiello, E.A., Gonzalez Leon, C., Docena, G., and Milesi, V. 2017. The inhibition of voltage-gated H(+) channel (HVCN1) induces acidification of leukemic Jurkat T cells promoting cell death by apoptosis, *Pflugers Arch* 469, 251-261.

Barish, M.E., and Baud, C. 1984. A voltage-gated hydrogen ion current in the oocyte membrane of the axolotl, Ambystoma, *J Physiol* 352, 243-263.

Berger, T.K., Fussholler, D.M., Goodwin, N., Bonigk, W., Muller, A., Dokani Khesroshahi, N., Brenker, C., Wachten, D., Krause, E., Kaupp, U.B., and Strunker, T. 2017.

Post-translational cleavage of Hv1 in human sperm tunes pH- and voltage-dependent gating, *J Physiol* 595, 1533-1546.

Berger, T.K., and Isacoff, E.Y. 2011. The pore of the voltage-gated proton channel, *Neuron* 72, 991-1000.

Bernheim, L., Krause, R.M., Baroffio, A., Hamann, M., Kaelin, A., and Bader, C.R. 1993. A voltage-dependent proton current in cultured human skeletal muscle myotubes, *J Physiol* 470, 313-333.

Byerly, L., Meech, R., and Moody, W., Jr. 1984. Rapidly activating hydrogen ion currents in perfused neurones of the snail, Lymnaea stagnalis, *J Physiol* 351, 199-216.

Capasso, M. 2014. Regulation of immune responses by proton channels, *Immunology* 143, 131-137.

Capasso, M., Bhamrah, M.K., Henley, T., Boyd, R.S., Langlais, C., Cain, K., Dinsdale, D., Pulford, K., Khan, M., Musset, B., Cherny, V.V., Morgan, D., Gascoyne, R.D., Vigorito, E., DeCoursey, T.E., MacLennan, I.C., and Dyer, M.J. 2010. HVCN1 modulates BCR signal strength via regulation of BCR-dependent generation of reactive oxygen species, *Nat Immunol* 11, 265-272.

Catterall, W.A. 1995. Structure and function of voltage-gated ion channels, *Annu Rev Biochem* 64, 493-531.

Cherny, V.V., Henderson, L.M., Xu, W., Thomas, L.L., and DeCoursey, T.E. 2001. Activation of NADPH oxidase-related proton and electron currents in human eosinophils by arachidonic acid, *J Physiol* 535, 783-794.

Cherny, V.V., Markin, V.S., and DeCoursey, T.E. 1995. The voltage-activated hydrogen ion conductance in rat alveolar epithelial cells is determined by the pH gradient, *J Gen Physiol* 105, 861-896.

Cherny, V.V., Murphy, R., Sokolov, V., Levis, R.A., and DeCoursey, T.E. 2003. Properties of single voltage-gated proton channels in human eosinophils estimated by noise analysis and by direct measurement, *J Gen Physiol* 121, 615-628.

Cho, D.Y., Hajighasemi, M., Hwang, P.H., Illek, B., and Fischer, H. 2009. Proton secretion in freshly excised sinonasal mucosa from asthma and sinusitis patients, *Am J Rhinol Allergy* 23, e10-13.

DeCoursey, T.E. 1991. Hydrogen ion currents in rat alveolar epithelial cells, *Biophys J* 60, 1243-1253.

DeCoursey, T.E. 2013. Voltage-gated proton channels: molecular biology, physiology, and pathophysiology of the H(V) family, *Physiol Rev* 93, 599-652.

DeCoursey, T.E. 2018. Voltage and pH sensing by the voltage-gated proton channel, HV1, *J R Soc Interface* 15.

DeCoursey, T.E., and Cherny, V.V. 1993. Potential, pH, and arachidonate gate hydrogen ion currents in human neutrophils, *Biophys J* 65, 1590-1598.

DeCoursey, T.E., and Cherny, V.V. 1994. Voltage-activated hydrogen ion currents, *J Membr Biol* 141, 203-223.

DeCoursey, T.E., Cherny, V.V., DeCoursey, A.G., Xu, W., and Thomas, L.L. 2001a. Interactions between NADPH oxidase-related proton and electron currents in human eosinophils, *J Physiol* 535, 767-781.

DeCoursey, T.E., Cherny, V.V., Morgan, D., Katz, B.Z., and Dinauer, M.C. 2001b. The gp91phox component of NADPH oxidase is not the voltage-gated proton channel in phagocytes, but it helps, *J Biol Chem* 276, 36063-36066.

DeCoursey, T.E., Cherny, V.V., Zhou, W., and Thomas, L.L. 2000. Simultaneous activation of NADPH oxidase-related proton and electron currents in human

neutrophils, *Proceedings of the National Academy of Sciences of the United States of America* 97, 6885-6889.

DeCoursey, T.E., Morgan, D., and Cherny, V.V. 2003. The voltage dependence of NADPH oxidase reveals why phagocytes need proton channels, *Nature* 422, 531-534.

Demaurex, N., Grinstein, S., Jaconi, M., Schlegel, W., Lew, D.P., and Krause, K.H. 1993a. Proton currents in human granulocytes: regulation by membrane potential and intracellular pH, *J Physiol* 466, 329-344.

Demaurex, N., Schrenzel, J., Jaconi, M.E., Lew, D.P., and Krause, K.H. 1993b. Proton channels, plasma membrane potential, and respiratory burst in human neutrophils, *Eur J Haematol* 51, 309-312.

Fernandez, A., Pupo, A., Mena-Ulecia, K., and Gonzalez, C. 2016. Pharmacological Modulation of Proton Channel Hv1 in Cancer Therapy: Future Perspectives, *Mol Pharmacol* 90, 385-402.

Fischer, H. 2012. Function of Proton Channels in Lung Epithelia, *Wiley Interdiscip Rev Membr Transp Signal* 1, 247-258.

Fischer, H., Widdicombe, J.H., and Illek, B. 2002. Acid secretion and proton conductance in human airway epithelium, *Am J Physiol Cell Physiol* 282, C736-743.

Fogel, M., and Hastings, J.W. 1972. Bioluminescence: mechanism and mode of control of scintillon activity, *Proceedings of the National Academy of Sciences of the United States of America* 69, 690-693.

Fujiwara, Y., Kurokawa, T., Takeshita, K., Kobayashi, M., Okochi, Y., Nakagawa, A., and Okamura, Y. 2012. The cytoplasmic coiled-coil mediates cooperative gating temperature sensitivity in the voltage-gated H(+) channel Hv1, *Nat Commun* 3, 816.

Gonzalez, C., Koch, H.P., Drum, B.M., and Larsson, H.P. 2010. Strong cooperativity between subunits in voltage-gated proton channels, *Nat Struct Mol Biol* 17, 51-56.

Gonzalez, C., Rebolledo, S., Perez, M.E., and Larsson, H.P. 2013. Molecular mechanism of voltage sensing in voltage-gated proton channels, *J Gen Physiol* 141, 275-285.

Gordienko, D.V., Tare, M., Parveen, S., Fenech, C.J., Robinson, C., and Bolton, T.B. 1996. Voltage-activated proton current in eosinophils from human blood, *J Physiol* 496 (Pt 2), 299-316.

Henderson, L.M. 2001. NADPH oxidase subunit gp91phox: a proton pathway, *Protoplasma* 217, 37-42.

Henderson, L.M., Chappell, J.B., and Jones, O.T. 1987. The superoxide-generating NADPH oxidase of human neutrophils is electrogenic and associated with an H+ channel, *Biochem J* 246, 325-329.

Henderson, L.M., Chappell, J.B., and Jones, O.T. 1988. Internal pH changes associated with the activity of NADPH oxidase of human neutrophils. Further evidence for the presence of an H+ conducting channel, *Biochem J* 251, 563-567.

Henderson, L.M., and Meech, R.W. 2002. Proton conduction through gp91phox, *J Gen Physiol* 120, 759-765.

Hondares, E., Brown, M.A., Musset, B., Morgan, D., Cherny, V.V., Taubert, C., Bhamrah, M.K., Coe, D., Marelli-Berg, F., Gribben, J.G., Dyer, M.J., DeCoursey, T.E., and Capasso, M. 2014. Enhanced activation of an amino-terminally truncated isoform of the voltage-gated proton channel HVCN1 enriched in malignant B cells, *Proceedings of the National Academy of Sciences of the United States of America* 111, 18078-18083.

Iovannisci, D., Illek, B., and Fischer, H. 2010. Function of the HVCN1 proton channel in airway epithelia and a naturally occurring mutation, M91T, *J Gen Physiol* 136, 35-46.

Kapus, A., Romanek, R., Qu, A.Y., Rotstein, O.D., and Grinstein, S. 1993. A pH-sensitive and voltage-dependent proton conductance in the plasma membrane of macrophages, *J Gen Physiol* 102, 729-760.

Klee, R., Heinemann, U., and Eder, C. 1999. Voltage-gated proton currents in microglia of distinct morphology and functional state, *Neuroscience* 91, 1415-1424.

Koch, H.P., Kurokawa, T., Okochi, Y., Sasaki, M., Okamura, Y., and Larsson, H.P. 2008. Multimeric nature of voltage-gated proton channels, *Proceedings of the National Academy of Sciences* 105, 9111-9116.

Krause, R.M., Bernheim, L., and Bader, C.R. 1993. Human skeletal muscle has a voltage-gated proton current, *Neuromuscul Disord* 3, 407-411.

Lee, S.Y., Letts, J.A., and Mackinnon, R. 2008. Dimeric subunit stoichiometry of the human voltage-dependent proton channel Hv1, *Proceedings of the National Academy of Sciences of the United States of America* 105, 7692-7695.

Levine, A.P., Duchen, M.R., de Villiers, S., Rich, P.R., and Segal, A.W. 2015. Alkalinity of neutrophil phagocytic vacuoles is modulated by HVCN1 and has consequences for myeloperoxidase activity, *PLoS One* 10, e0125906.

Li, S.J., Zhao, Q., Zhou, Q., Unno, H., Zhai, Y., and Sun, F. 2010. The role and structure of the carboxyl-terminal domain of the human voltage-gated proton channel Hv1, *J Biol Chem* 285, 12047-12054.

Lishko, P.V., Botchkina, I.L., Fedorenko, A., and Kirichok, Y. 2010. Acid extrusion from human spermatozoa is mediated by flagellar voltage-gated proton channel, *Cell* 140, 327-337.

Mahaut-Smith, M.P. 1989a. The effect of zinc on calcium and hydrogen ion currents in intact snail neurones, *J Exp Biol* 145, 455-464.

Mahaut-Smith, M.P. 1989b. Separation of hydrogen ion currents in intact molluscan neurones, *J Exp Biol* 145, 439-454.

Maturana, A., Arnaudeau, S., Ryser, S., Banfi, B., Hossle, J.P., Schlegel, W., Krause, K.H., and Demaurex, N. 2001. Heme histidine ligands within gp91(phox) modulate proton conduction by the phagocyte NADPH oxidase, *J Biol Chem* 276, 30277-30284.

Morgan, D., Cherny, V.V., Finnegan, A., Bollinger, J., Gelb, M.H., and DeCoursey, T.E. 2007. Sustained activation of proton channels and NADPH oxidase in human eosinophils and murine granulocytes requires PKC but not cPLA2 alpha activity, *J Physiol* 579, 327-344.

Morgan, D., Cherny, V.V., Murphy, R., Katz, B.Z., and DeCoursey, T.E. 2005. The pH dependence of NADPH oxidase in human eosinophils, *J Physiol* 569, 419-431.

Morgan, D., McIntire, P., Cherny, V., Smith, S., Musset, B., and DeCoursey, T. 2015. Proton Channels are Present in Cell Membranes of the Breast Cancer Cell Line MDA MB 231 and Affect Recovery from an Acid Load, *Biophysical Journal* 108, 587a-587a.

Murata, Y., Iwasaki, H., Sasaki, M., Inaba, K., and Okamura, Y. 2005. Phosphoinositide phosphatase activity coupled to an intrinsic voltage sensor, *Nature* 435, 1239-1243.

Murillo, I., and Henderson, L.M. 2005. Expression of gp91phox/Nox2 in COS-7 cells: cellular localization of the protein and the detection of outward proton currents, *Biochem J* 385, 649-657.

Murphy, R., Cherny, V.V., Morgan, D., and DeCoursey, T.E. 2005. Voltage-gated proton channels help regulate pHi in rat alveolar epithelium, *Am J Physiol Lung Cell Mol Physiol* 288, L398-408.

Musset, B., Capasso, M., Cherny, V.V., Morgan, D., Bhamrah, M., Dyer, M.J., and DeCoursey, T.E. 2010. Identification of Thr29 as a critical phosphorylation site that activates the human proton channel Hvcn1 in leukocytes, *J Biol Chem* 285, 5117-5121.

Musset, B., Morgan, D., Cherny, V.V., MacGlashan, D.W., Jr., Thomas, L.L., Rios, E., and DeCoursey, T.E. 2008. A pH-stabilizing role of voltage-gated proton channels in IgE-mediated activation of human basophils, *Proceedings of the National Academy of Sciences of the United States of America* 105, 11020-11025.

Musset, B., Smith, S.M., Rajan, S., Morgan, D., Cherny, V.V., and Decoursey, T.E. 2011. Aspartate 112 is the selectivity filter of the human voltage-gated proton channel, *Nature* 480, 273-277.

Okochi, Y., Sasaki, M., Iwasaki, H., and Okamura, Y. 2009. Voltage-gated proton channel is expressed on phagosomes, *Biochem Biophys Res Commun* 382, 274-279.

Pang, H., Li, J., Du, H., Gao, Y., Lv, J., Liu, Y., and Li, S.J. 2020a. Loss of voltage-gated proton channel Hv1 leads to diet-induced obesity in mice, *BMJ Open Diabetes Res Care* 8.

Pang, H., Wang, X., Zhao, S., Xi, W., Lv, J., Qin, J., Zhao, Q., Che, Y., Chen, L., and Li, S.J. 2020b. Loss of voltage-gated proton channel Hv1 decreases insulin secretion and leads to hyperglycemia and glucose intolerance in mice, *J Biol Chem*.

Qiu, F., Rebolledo, S., Gonzalez, C., and Larsson, H.P. 2013. Subunit interactions during cooperative opening of voltage-gated proton channels, *Neuron* 77, 288-298.

Ramsey, I.S., Moran, M.M., Chong, J.A., and Clapham, D.E. 2006. A voltage-gated proton-selective channel lacking the pore domain, *Nature* 440, 1213-1216.

Ramsey, I.S., Ruchti, E., Kaczmarek, J.S., and Clapham, D.E. 2009. Hv1 proton channels are required for high-level NADPH oxidase-dependent superoxide production during the phagocyte respiratory burst, *Proceedings of the National Academy of Sciences of the United States of America* 106, 7642-7647.

Rybicka, J.M., Balce, D.R., Chaudhuri, S., Allan, E.R.O., and Yates, R.M. 2012. Phagosomal proteolysis in dendritic cells is modulated by NADPH oxidase in a pH-independent manner, *Embo J* 31, 932-944.

Sasaki, M., Takagi, M., and Okamura, Y. 2006. A voltage sensor-domain protein is a voltage-gated proton channel, *Science* 312, 589-592.

Sasaki, M., Tojo, A., Okochi, Y., Miyawaki, N., Kamimura, D., Yamaguchi, A., Murakami, M., and Okamura, Y. 2013. Autoimmune disorder phenotypes in Hvcn1-deficient mice, *Biochem J* 450, 295-301.

Schilling, T., Gratopp, A., DeCoursey, T.E., and Eder, C. 2002. Voltage-activated proton currents in human lymphocytes, *J Physiol* 545, 93-105.

Schrenzel, J., Lew, D.P., and Krause, K.H. 1996. Proton currents in human eosinophils, *Am J Physiol* 271, C1861-1871.

Smith, R.Y., Morgan, D., Sharma, L., Cherny, V.V., Tidswell, N., Molo, M.W., and DeCoursey, T.E. 2019. Voltage-gated proton channels exist in the plasma membrane of human oocytes, *Hum Reprod* 34, 1974-1983.

Szteyn, K., Yang, W., Schmid, E., Lang, F., and Shumilina, E. 2012. Lipopolysaccharide-sensitive H+ current in dendritic cells, *Am J Physiol Cell Physiol* 303, C204-212.

Thomas, R.C., and Meech, R.W. 1982. Hydrogen ion currents and intracellular pH in depolarized voltage-clamped snail neurones, *Nature* 299, 826-828.

Tian, D.S., Li, C.Y., Qin, C., Murugan, M., Wu, L.J., and Liu, J.L. 2016. Deficiency in the voltage-gated proton channel Hv1 increases M2 polarization of microglia and attenuates brain damage from photothrombotic ischemic stroke, *J Neurochem* 139, 96-105.

Tombola, F., Ulbrich, M.H., Kohout, S.C., and Isacoff, E.Y. 2010. The opening of the two pores of the Hv1 voltage-gated proton channel is tuned by cooperativity, *Nat Struct Mol Biol* 17, 44-50.

Wang, Y., Li, S.J., Pan, J., Che, Y., Yin, J., and Zhao, Q. 2011. Specific expression of the human voltage-gated proton channel Hv1 in highly metastatic breast cancer cells, promotes tumor progression and metastasis, *Biochem Biophys Res Commun* 412, 353-359.

Wang, Y., Li, S.J., Wu, X., Che, Y., and Li, Q. 2012. Clinicopathological and biological significance of human voltage-gated proton channel Hv1 protein overexpression in breast cancer, *J Biol Chem* 287, 13877-13888.

Wang, Y., Wu, X., Li, Q., Zhang, S., and Li, S.J. 2013a. Human voltage-gated proton channel hv1: a new potential biomarker for diagnosis and prognosis of colorectal cancer, *PLoS One* 8, e70550.

Wang, Y., Zhang, S., and Li, S.J. 2013b. Zn(2+) induces apoptosis in human highly metastatic SHG-44 glioma cells, through inhibiting activity of the voltage-gated proton channel Hv1, *Biochem Biophys Res Commun* 438, 312-317.

Wu, L.J., Wu, G., Akhavan Sharif, M.R., Baker, A., Jia, Y., Fahey, F.H., Luo, H.R., Feener, E.P., and Clapham, D.E. 2012. The voltage-gated proton channel Hv1 enhances brain damage from ischemic stroke, *Nat Neurosci* 15, 565-573.

Yu, Y., Yu, Z., Xie, M., Wang, W., and Luo, X. 2018. Hv1 proton channel facilitates production of ROS and pro-inflammatory cytokines in microglia and enhances oligodendrocyte progenitor cells damage from oxygen-glucose deprivation in vitro, *Biochem Biophys Res Commun* 498, 1-8.

Zhao, Q., Che, Y., Li, Q., Zhang, S., Gao, Y.T., Wang, Y., Wang, X., Xi, W., Zuo, W., and Li, S.J. 2015. The voltage-gated proton channel Hv1 is expressed in pancreatic islet beta-cells and regulates insulin secretion, *Biochem Biophys Res Commun* 468, 746-751.

Zhu, X., Mose, E., and Zimmermann, N. 2013. Proton channel HVCN1 is required for effector functions of mouse eosinophils, *BMC Immunol* 14, 24.

CHAPTER 2

GATING CHARGE TRAPPING IN VOLTAGE-GATED PROTON (H_V1) CHANNELS

2.1 Abstract

The voltage-gated proton (H_v1) channel contains a voltage sensor and a conductive pore in one structural module. Voltage sensor movements can be directly detected by measuring gating currents, and detailed characterization of H_v1 charge displacements during channel activation can help to understand the function of this channel. I succeeded in detecting gating currents in the monomeric form of the *Ciona*-H_v1 channel. To decrease proton currents and better separate gating currents from ion currents, I used the low-conducting H_v1 mutant N264R. Isolated ON-gating currents decayed at increasing rates with membrane depolarization, and the amount of gating charges displaced saturates at high voltages, two hallmarks of currents arising from the movement of charged elements within the boundaries of the cell membrane. The kinetic analysis of gating currents revealed a complex time course of the ON-gating current characterized by two peaks and a marked Cole-Moore effect. Both features indicate that the voltage sensor undergoes several voltage-dependent conformational changes during activation. However, most of the charge is displaced in a single central transition. Upon voltage sensor activation, the charge is trapped and only a fast component that carries a small percentage of the total charge is observed after repolarization. I hypothesize that trapping is due to the presence of the arginine side chain in position 264, which acts as a blocking ion. I conclude that the movement of the voltage sensor must proceed through at least five states to account for our experimental data satisfactorily.

2.2 Introduction

Voltage-gated proton channels (H_v1) are transmembrane proteins that regulate cellular pH producing outward proton currents in response to depolarization. Since the discovery of the *Ciona intestinalis*, mouse, and human H_v1 genes in 2006 (Ramsey et al., 2006; Sasaki et al., 2006), the relevance of this channel in physiological and pathophysiological processes has increased continuously (DeCoursey, 2018). H_v1 is a voltage-gated ion channel with a unique structure and properties. It is a homodimer (Koch et al., 2008b; Lee et al., 2008; Tombola et al., 2008) containing four transmembrane alpha helixes in each subunit (S1 to S4). Both the voltage sensor and the permeation pathway of this channel originate from these four transmembrane segments. The fourth transmembrane helix (S4) contains three conserved arginine residues responsible for the channel voltage sensitivity (Gonzalez et al., 2010; Gonzalez et al., 2013). The intracellular N-terminal domain is variable in both length and sequence among different species. The intracellular C-terminal domain forms a coiled-coil structure necessary for dimer formation (Koch et al., 2008b). H_v1 is voltage- (Gonzalez et al., 2013) and pH-dependent (Cherny et al., 1995), it is highly selective to protons (Musset et al., 2011), has a small unitary conductance (Cherny et al., 2003) and display a cooperative gating between subunits (Fujiwara et al., 2012; Gonzalez et al., 2010). However, there are still many open questions regarding the mechanisms of H_v1 activation. In particular, the details regarding how the gating charges are displaced during activation and how these movements are related to channel opening are known. In this thesis, I contributed to answering these questions.

H_v1 voltage sensor movement has been studied principally by two methods: accessibility assays and fluorescence. In the first case, membrane-impermeable thiol-reactive methanethiosulfonate (MTS) probes were used to test the state-dependent accessibility

of a cysteine residue introduced into a specific region of the voltage sensor (Larsson et al., 1996). In the case of H_v1, accessibility experiments indicate that both S1 (Mony et al., 2015) and S4 (Gonzalez et al., 2013) undergo conformational changes during activation and that there is cooperativity between the subunits of the channel (Gonzalez et al., 2010). The second approach involves the use of voltage-clamp fluorometry (VCF) (Gandhi and Olcese, 2009). In VCF, the conformational changes of the channel are monitored by a fluorescent probe bound to a cysteine introduced into a specific site using mutagenesis (Cha and Bezanilla, 1997; Mannuzzu et al., 1996). VCF experiments revealed two conformational changes during activation (Qiu et al., 2013), following the S4 movement there is a displacement of S1 associated with the opening of the channel (Mony et al., 2015). The caveat of these methodologies is that they are indirect approaches to study the dynamics of the H_v1 voltage sensor. In contrast, gating currents directly report the movement of the voltage-sensing charges across the membrane electric field, making it possible to study the kinetics of this process in detail. Here I present a detailed study of gating currents from fast activating monomeric H_v1 channels carrying a mutation that impairs proton conductance (N264R) (Qiu et al., 2013).

In *Shaker* voltage-gated potassium channel, gating currents are produced by the movement of arginine residues in the S4 transmembrane segment within the voltage sensor domain (Aggarwal and MacKinnon, 1996; Seoh et al., 1996). Three of these arginine residues are conserved in S4 of H_v1 and were shown to be responsible for the voltage-dependent gating of the channel (Gonzalez et al., 2013). Since the *Ciona*-H_v1 channels express well in oocytes, it should be possible to record gating currents induced by the activation of this channel. Indeed, preliminary studies on H_v1 gating current have been reported (Baez-Nieto et al., 2014; Carmona et al., 2018; De La Rosa and Ramsey,

2018a). I used a monomeric form of the H_v1 carrying a deletion of the N- Δ(1-128) and C-terminal Δ(269-342) domains that are necessary for channel dimerization (Koch et al., 2008a). The mutant channel maintains the hallmark biophysical properties of H_v1, including the voltage dependency, proton selectivity, and pH sensitivity. However, it exhibits much faster kinetics of activation than the dimeric H_v1 (Koch et al., 2008a). I demonstrate that the initial current transients evoked by depolarizing steps in *Xenopus* oocyte expressing N264R H_v1 monomers fulfill the requirements to be recognized as gating currents (Chandler et al., 1976). The gating charge-voltage curves saturate at high voltages, the kinetics of current decay is voltage-dependent, and the charge displaced during the ON returns slowly during repolarization. The data is consistent with a gating kinetics model in which the displacement of the voltage sensor must proceed at least five states before channel opening. Finally, the finding that the ON charge is not recovered in the OFF suggests that a large fraction of the gating charge is trapped in the last transitions.

2.3 Materials and Methods

2.3.1 Mutagenesis, transcription, and sequencing. The single N264R mutation was introduced with QuickChange kit (Promega Corp.) in pSP64T-contained *Ciona intestinalis* H_v1 sequence kindly provided by Dr. Okamura. The $\Delta N\Delta C$ H_v1 was constructed with a stop codon at Val270 and initiator methionine replacing Glu129 (Koch et al., 2008b). Primers were designed using the web service QuickChange Primer Design. Mutant DNA was amplified by PCR, checked by sequencing, and then linearized with NotI restriction enzyme. *In vitro* transcription was performed with mMESSAGE mMACHINE kit (Ambion) using RNA polymerase SP6. RNA was quantified by absorbance at 260 nm, and its

integrity was checked by electrophoresis in 1% agarose gel with ethidium bromide at 0.6 µg/µL.

2.3.2 Oocytes extraction and RNA injection. *Xenopus laevis* oocytes were obtained and injected with 50 nL of RNA at a concentration of 1 µg/µL according to previously described methodologies (Alvarez et al., 2019).

2.3.3 Electrophysiology. Voltage clamp recordings were performed in inside-out giant patches of oocytes membranes (Hilgemann, 1995). The internal and external solutions contained 100 mM HEPES, 2 mM $MgCl_2$, 1 mM EGTA, and 50 mM N-methyl-D-glucamine (NMDG)-methanesulfonate. pH was adjusted with NMDG or methanesulphonate to 7.0. Measurements were performed at room temperature (22 °C). Pipettes of borosilicate capillary glass (1B150F-4, World Precision Instruments) were pulled on a horizontal pipette puller (Sutter Instruments) and fire-polished until obtaining a diameter between 15 to 24 µm (resistances of 0.8-1.2 MΩ in the bath solution). Data were acquired with an Axopatch 200B amplifier (Axon Instruments). Both the voltage command and current output were filtered at 20 kHz with 8-pole Bessel low-pass filters (Frequency Devices). Analog signals were sampled with a 16-bit A/D converter (Digidata 1440A, Axon Instruments) at 250 kHz. Experiments were performed using Clampex 8 acquisition software (Axon Instruments). Capacitive currents were compensated by analog circuitry, and linear capacitive currents were subtracted using a P/-8 protocol with a sub-sweep holding potential of -90 mV (Armstrong and Bezanilla, 1973). Data analysis was performed with Python programming language scripts (Python Software Foundation, https://www.python.org/).

2.3.4 Gating current simulations. A five-state linear kinetic model was simulated by solving the equation $d\boldsymbol{P}(t)/dt = \boldsymbol{P}(t)\mathbf{Q}$, where $\boldsymbol{P}(t)$ is the probability vector of the states and

Q is the transition rate matrix. I solved the time dependency of ***P***(*t*) using the spectral expansion (Colquhoun and Hawkes, 1995). Forward and reverse kinetic constants, $\alpha(V)$ and $\beta(V)$ respectively, were modeled as $\alpha(V)= \alpha_0 \exp(xz\delta e_0 V/kT)$ and $\beta(V)= \beta_0 \exp((x-1)z\delta e_0 V/kT)$, where α_0 and β_0 are the kinetic constants at V=0 mV, $z\delta e_0$ is the charge moved in the transition, x is the fraction of the charge moved from a well to the barrier peak in each forward transition, and k, and T has its usual meaning. Gating currents $I_g(t)$ were obtained with the equation $I_g(t)=N\boldsymbol{F}(t)\boldsymbol{Z}$, where N is the number of channels, $\boldsymbol{F}(t)$ is the net flux of each transition (Vandenberg and Bezanilla, 1991), and ***Z*** is a vector containing the charge associated to each transition. Parameters were obtained comparing the experimental data qualitatively with the simulation results. Simulations and model parameter searches were performed with Python programming language scripts (Python Software Foundation, https://www.python.org/). Scripts are available in the digital format of this thesis or can be solicited to the author.

2.4 Results

2.4.1 H_v1 gating currents are revealed in monomeric channels and better resolved in conductance impaired N264R mutant

To detect H_v1 gating currents, I expressed wild-type *Ciona intestinalis* H_v1 channels in *Xenopus laevis* oocytes and recorded membrane currents in giant patches (inside-out configuration and symmetrical pH = 7.0). In dimeric H_v1, I was unable to resolve any non-linear capacitive currents. At short times after the onset of the depolarizing pulse, we observed a monotonic development of current free of any transient component (**Fig. 2.1a**). In contrast, upon depolarization, oocytes membrane patches expressing fast activating monomeric channels display an initial current step that preceded the

development of ion currents (**Fig. 2.1b**). As expected for gating currents, these initial step currents were absent during hyperpolarizing pulses (**Fig. 2.1c**). I conclude that my failure to detect gating currents in the dimeric H_v1 channels is their slow kinetics and small amplitude.

Since ion currents heavily contaminate the putative gating currents from monomeric H_v1, I resorted to the N264R mutant of monomeric H_v1 that greatly decreases proton currents while retaining voltage sensor movement as assayed by indirect methods (Qiu et al., 2013; Sakata et al., 2010). At depolarizing voltages, currents recorded from this mutant channel showed an early transient current followed by increasing outward currents (**Fig. 2.1d**). During repolarization, I can distinguish a rapid transient current followed by a nearly constant component. Most likely, the transient component is gating charge movement, but the slow component may be a mix of ion and gating current (**Fig. 2.1d**). To corroborate that the ON-transient is due to non-linear charge movement, I also show that hyperpolarization evoked currents lack this component (**Fig. 2.1e**). The following analysis will demonstrate that the early currents in **Fig. 2.1d** are indeed gating currents.

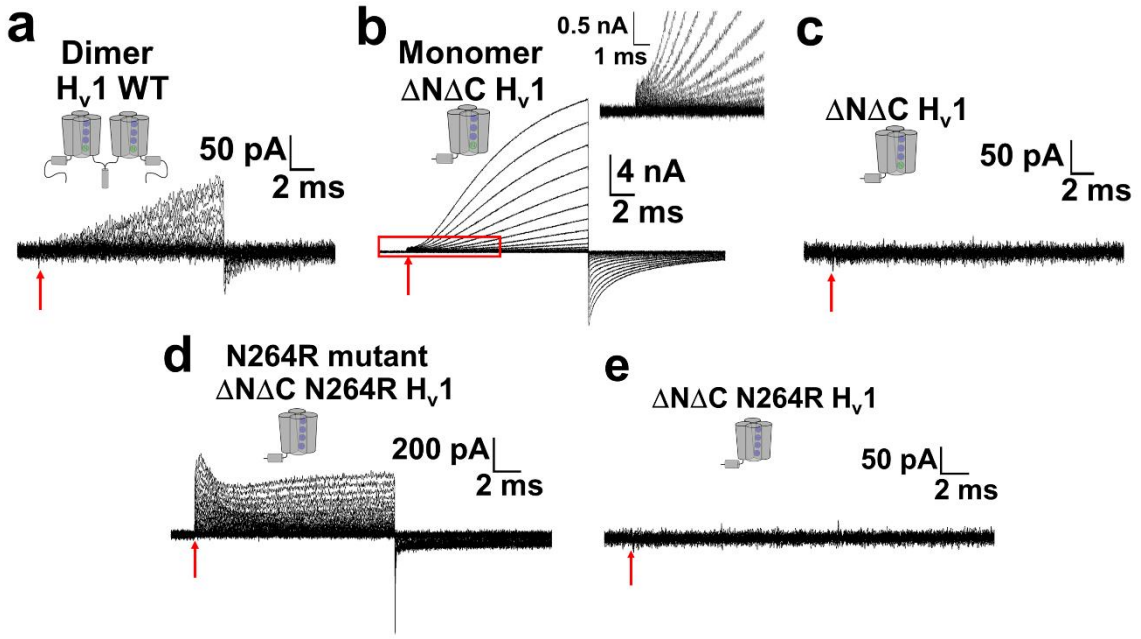

Figure 2.1. An early non-linear capacitive current was detected in the monomeric H_v1. (a) Currents produced by the dimeric H_v1 did not show an initial non-linear capacitive component. (b) Currents produced by the monomeric form of the channel presented an initial step (see inset) preceding the development of fast proton currents. (c) A hyperpolarizing protocol applied to patches expressing the monomeric H_v1 did not produce similar currents. (d) Currents produced by the conductance impaired monomeric H_v1 mutant N264R presented an initial non-linear transient current followed by the development of proton currents. (e) A hyperpolarizing protocol applied to patches expressing the monomeric H_v1 mutant N264R did not produce currents. Superimposed current traces were recorded for membrane voltage steps from -90 to +200 mV in 10 mV increments in (a) and (b), from -90 to +260 mV in 10 mV increments in (d), and from to -330 to -50 mV in 10 mV increments in (c) and (e). Red arrows indicate the time at which the voltages pulses were applied. Holding potential was -70 mV. The linear capacitive current was subtracted online using a P/-8 pulse protocol.

2.4.2 H_v1 gating currents can be isolated from ion currents

Isolation of the ON-gating currents was performed numerically assuming that the currents recorded from monomeric H_v1 mutant (I_{exp}) were the sum of gating (I_g) and ion currents (I_i) (Baez-Nieto et al., 2014).

$$I_{exp}(t) = I_g(t) + I_i(t) \tag{2.1}$$

Gating currents were modeled as a product of an increasing and a decreasing exponential function, corresponding to the rising and decaying phase of the gating currents, respectively.

$$I_g(t) = A\left(1 - e^{-t/\tau_1}\right)e^{-t/\tau_2} \tag{2.2}$$

where *A* is the amplitude and τ_1 and τ_2 are the time constants of the increasing and the decreasing exponential functions, respectively. Ion currents were modeled as an exponential function raised to the power of two with a time constant τ_3, which accounts for the sigmoidal shape of macroscopic current time course from mutant monomeric H_v1 (**Fig. 2.1b**).

$$I_i(t) = B\left(1 - e^{-t/\tau_3}\right)^2 \tag{2.3}$$

where *B* is the amplitude of the ion current component. **Fig. 2.2a** shows examples of the fitting procedure of the current records at six different voltages. Plots of the isolated gating currents $I_g(t)$ show that both the amplitude and the rate of decay increase with voltage as expected from *bona fide* gating currents (**Fig. 2.2b**). The time course of the charge displaced, obtained by integrating $I_g(t)$, is shown in **Fig. 2.2c**. The time constant of the gating current decay (τ_2; equation 2.2) vs voltage data were fitted assuming that the conformational change of the voltage sensor is well described by a first-order process: resting-active (**A**-**B**) (**Fig. 2.2d**, open circles). In the **A**-**B** two-state model, voltage-dependent time constants and rates are given by the equations:

$$\tau_2(V) = \frac{1}{\alpha(V)+\beta(V)}, \quad \alpha(V) = \alpha_0 e^{\frac{z\delta_\alpha e_0 V}{kT}}, \quad \beta(V) = \beta_0 e^{\frac{-z\delta_\beta e_0 V}{kT}} \tag{2.4}$$

where $\alpha(V)$ and $\beta(V)$ are the forward and backward rate constants, respectively and α_0 and β_0 are the rate constants for $V = 0$; $z\delta_\alpha$ and $z\delta_\beta$ describe the voltage dependence of the rates, e_0 is the elementary charge, and k and T have their usual meanings. The parameters that best described the data shown were α_0 = 0.027 ± 0.002 ms^{-1}, β_0 = 0.15 ± 0.01 ms^{-1}, $z\delta_\alpha$ = 0.34 ± 0.02 and $z\delta_\beta$ = 1.44 ± 0.12 (**Fig. 2.2d**; solid line). $\beta(V)$ is more voltage-dependent than $\alpha(V)$ and as a result, the bell-shaped time constant vs voltage plot is asymmetric (**Fig. 2.2d**).

Charge displaced at each voltage was obtained from the area under the corresponding isolated gating current, i.e. A times τ_2, (equation 2.2; **Fig. 2.2d**, solid circles). This $Q(V)$ curve showed a voltage-dependent saturation and was well fitted using a Boltzmann function:

$$Q(V) = \frac{Q_{max}}{1 + e^{\frac{-z\delta e_0 (V - V_{0.5})}{kT}}} \tag{2.5}$$

with half-activation voltage ($V_{0.5}$) of 52.8 ± 1.1 mV and effective valence ($z\delta$) of 1.23 ± 0.06 (**Fig. 2.2d**; solid line). For a set of 10 independent experiments, the average values of the parameters were: $z\delta$ = 1.05 ± 0.09 and $V_{0.5}$ = 54.8 ± 7.9 mV (mean ± S.E.M).

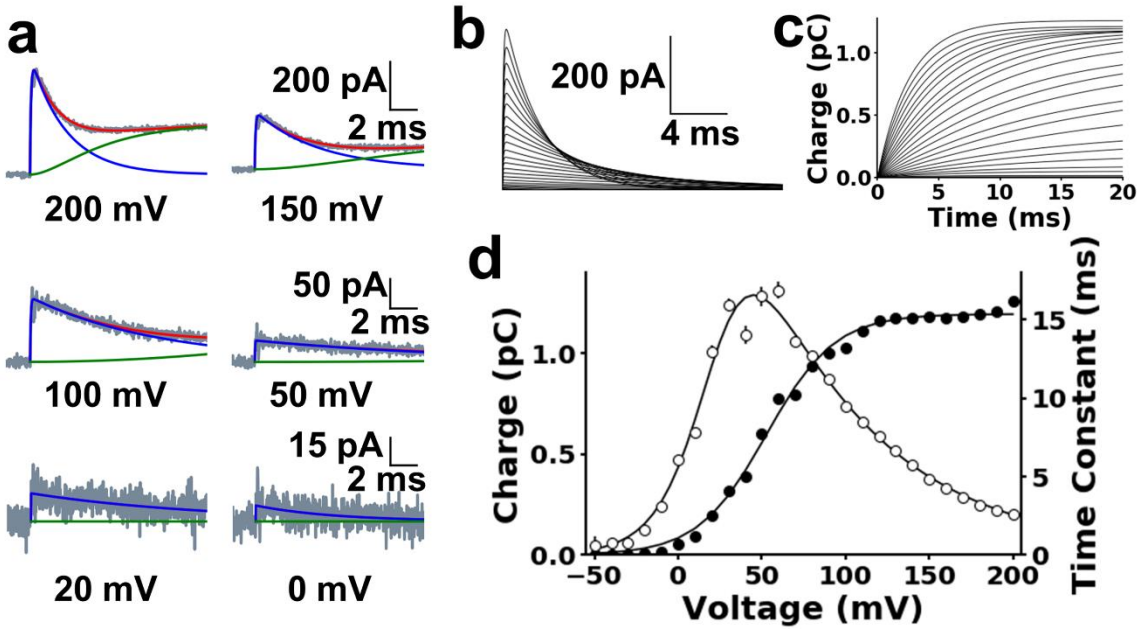

Figure 2.2. Isolated ON-gating currents were voltage-dependent. (a) Representative experimental currents recorded for the monomeric H_v1 mutant N264R during depolarizations at the indicated voltages (I_{exp}, black traces). They were fitted with equation (2.1) to isolate the ON-gating current (I_g, blue traces) from the ion current (I_i, green traces). Holding potential was -70 mV. (b) Superimposed plots of the isolated ON-gating currents for membrane voltage steps from -90 to +200 mV in 10 mV increments. (c) Time course of the gating charge displaced obtained integrating the gating currents shown in (b). (d) Time constants of the I_g decay (τ_2, open circles) and charge displaced as a function of voltage ($Q(V)$ curve, black circles). Time constant data were fitted using a two-state model (solid line), where α_0 = 0.027 ± 0.002 ms^{-1}, β_0 = 0.15 ± 0.01 ms^{-1}, $z\delta_\alpha$ = 0.34 ± 0.02 and $z\delta_\beta$ = 1.44 ± 0.12. $Q(V)$ curve was fitted by a Boltzmann function (solid line, equation 2.5), where Q_{max} = 1.19 ± 0.01 pC, $V_{0.5}$ = 53 ± 1 mV and $z\delta$ = 1.25 ± 0.06. Error bars are the standard deviation of the parameters obtained in the fitting procedure. The average values of the $Q(V)$ parameters (N = 10) were: $z\delta$ = 1.05 ± 0.09 and $V_{0.5}$ = 54.8 ± 7.9 mV.

2.4.3 H_v1 gating currents kinetics revealed that a large fraction of the charge is trapped

Fig. 2.2a shows that gating currents precede the development of ionic currents, giving a time window to characterize them in more detail. Accordingly, to minimize the activation of ion currents, I measured the OFF-gating currents after very short depolarizations.

Furthermore, after the pulse to 150 mV, the membrane potential was returned to the reversal potential of the proton currents (0 mV). Upon returning to 0 mV, I observed a rapid transient with a 0.03 ms time constant (**Fig. 2.3a and 2.3b inset**). However, the OFF-gating charges displaced during these brief transients are only a minute fraction of that displaced during the ON. This discrepancy indicates that while dwelling at 150 mV, a large fraction of the charges become trapped in a deep well. The amplitude of the OFF-gating currents increased with the duration of the depolarizing pulse and reached a plateau following an exponential function with a time constant of 1.31 ± 0.04 ms. (**Fig. 2.3b**). I computed the charge of OFF transient by multiplying the amplitude of the transient by the decay time constant of the spike (τ = 0.03 ms). The time course of the ON-gating current cannot be calculated directly from the current records due to the ion current contamination. To have a rough estimation of the ON-gating charge, I integrated the current numerically from the beginning of the depolarizing pulse up to 1 ms. From 1 ms on, I integrate the rest of the charge by multiplying the amplitude of the current at 1 ms by the 4 ms time constant of the gating current decay at 150 mV (**Fig 2.2d**). With these ON and OFF charges, we built the graph showed in **Fig. 2.3c**. For long depolarizing pulses, the OFF/ON charge ratio is 7/500 (or 1.4% of the ON). Therefore, the gating charge displaced during the ON is not recovered during the OFF.

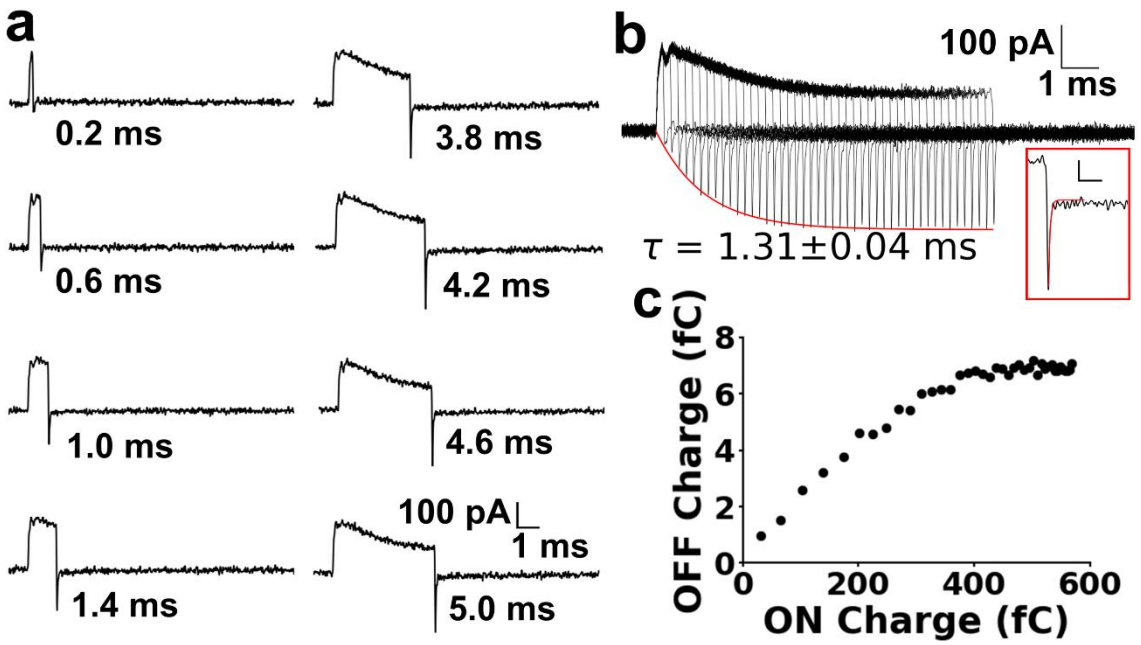

Figure 2.3. The gating charge is trapped during voltage sensor activation. (a) Currents recorded for a series of depolarizations with different durations. The protocol consisted of a prepulse voltage of -70 mV, followed by a test pulse to +150 mV and repolarization to 0 mV (reversal potential). Depolarization was imposed during the time indicated for each trace. (b) Superimposed series of current records produced by short depolarizations from a prepulse voltage of -70 mV, depolarization to +150 mV, and repolarization to 0 mV. Each trace is separated from the following by a 0.2 ms time increment. The time course of the fast component is described by the red line. Inset. OFF-gating current is well described by a single exponential of 0.03 ms (red trace). Scale bar: 50 pA and 0.4 ms. (c) OFF-gating charge as a function of the ON-gating charge for pulses of different durations. OFF charge was calculated multiplying the amplitude of the current by the time constant of decay (0.03 ms), while ON charge was integrated numerically and using the time constant at 150 mV (see text).

2.4.4 Trapped H_V1 gating charge is recovered during repolarization

I next designed a protocol to recover the ON-gating charges consisting of two 20 ms depolarization pulses to 150 mV from a holding potential of -70 mV separated by a repolarization of increasing duration at -70 mV (**Fig. 2.4a and b**). If the trapped gating charge returns slowly at -70 mV, the recovered charge can be measured during the second depolarizing pulse. At the onset of the second depolarization, a brief spike was recorded followed by a pedestal of ion current. The spike appeared after a brief

repolarization period, e.g. 2 ms. This ON spike is the mirror image of the OFF spike seen at the onset of the preceding repolarization. With a longer repolarization at -70 mV (50 ms), the ON spike disappears, and the gating current reaches an amplitude comparable with that of the first 20 ms pulse (**Fig. 2.4a and b**). The origin of the OFF and ON spikes will be explained with a five-state kinetic model (see below). The amount of charge recovered during the second pulse increases following an exponential time course with a time constant of 87.6 ± 7.4 ms (**Fig. 2.4b and c**). The charge extrapolated at very long times, Q_{∞}, is 1566 ± 80 fC (**Fig. 2.4c**), which compares well with the charge displaced during the ON (1500 fC). Note that the fast transient current during the ON-gating currents is only present when the repolarization period is short and disappears at long repolarizations (**Fig. 2.4a and b**). Moreover, I had consistently observed two peaks and a rising phase in the ON-gating current at 150 mV when the holding voltages were sufficiently negative (negative voltages in **Fig. 2.3a and 2.4d**). However, when I increase the holding voltages, only a single peak is detected (positive voltages in **Fig. 2.4d**). The rate of decay of the gating currents is also affected by the initial conditions, being faster with prepulse voltages above 0 mV (**Fig. 2.5a and b**). This protocol is equivalent to the well-known Cole-Moore effect (Cole and Moore, 1960; Gonzalez et al., 2000) and can reveal that the voltage sensor undergoes multiple voltage-dependent transition states (see Discussion) preceding the voltage sensor activation and channel opening (**Fig. 2.5c and d**). A Cole-Moore shift in dimeric native H_v1 channels was reported previously (DeCoursey and Cherny, 1994). However, my results show that this effect is also present in the monomeric form of the channel, indicating that the monomer also transits through several closed states before channel opening.

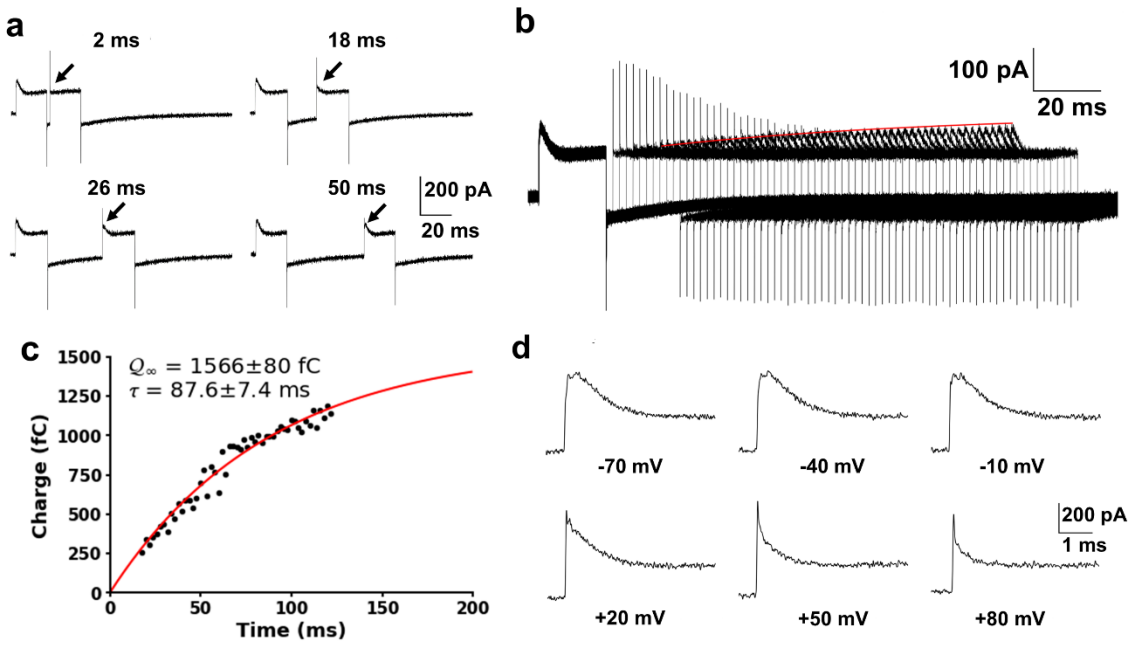

Figure 2.4. The OFF-gating charge is recovered slowly. (a) ON-gating current recovery protocol for four different times. Two depolarizing pulses from a holding potential of -70 mV to 150 mV were separated by the time indicated. A fast outward gating current appeared at short intervals, and it decreased at longer intervals, while a second slower component appeared at longer intervals (arrows). (b) Superimposed currents produced by the ON recovery protocol from a holding potential of -70 mV and depolarization to 150 mV. The interval of time between the depolarizing pulses increased 2 ms between traces. The red line describes the time course of the ON-gating charge recovery. (c) The charge displaced during the slow component of the second depolarization as a function of the time interval between the depolarizations. The data were fitted using a single increasing exponential function $Q_\infty[1-\exp(-t/\tau)]$ where Q_∞ is the exponential amplitude and τ is the time constant. Note that the asymptote of the curve is 1566 ± 80 fC, meaning that the charge is recovered completely. (d) Cole-Moore effect of the ON-gating current when a depolarizing pulse of 200 mV is preceded by the prepulse voltage indicated. Note how the two peaks of current are converted into a single peak of current and the kinetics of decay gets faster as the prepulse voltage becomes more positive.

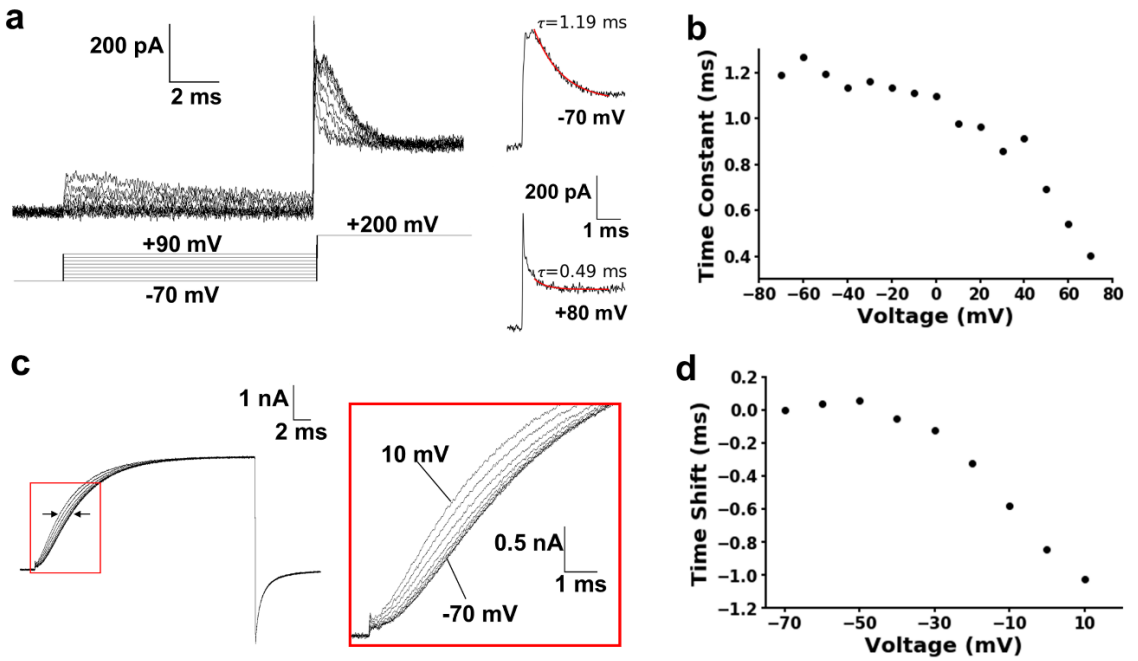

Figure 2.5. Cole-Moore effect of gating and proton currents in monomeric H_v1 channels. (a) Cole-Moore's shift of gating currents. Superimposed gating current traces of the monomeric H_v1 mutant N264R for a 200 mV pulse preceded by a prepulse from -70 to 90 mV in increments of 20 mV. The time constant for each trace was calculated fitting a single decreasing exponential function to the slowest component (red line, right). (b) Time constants were calculated as shown in (a) for different prepulse voltages. The kinetics become faster as the voltage of the prepulse increases. (c) Superimposed current traces of the monomeric H_v1 channels showing a Cole-Moore shift in the proton current as of the prepulse voltage increases. Note in the inset the presence of gating current at the beginning of the recording. A depolarization at 150 mV was preceded by a prepulse from -70 to +10 mV in 10 mV increments. Linear capacitive currents were subtracted by a P/-8 protocol. (d) Time-shift of the monomeric H_v1 channel proton current as a function of the prepulse voltage.

2.5 Discussion

2.5.1 Gating current measurements

The two main difficulties for measuring gating currents in the wild-type dimeric H_v1 are the slow kinetics of activation (**Fig. 2.6a** and **2.7**), which possibly is correlated with a slow movement of the voltage sensor, and the inability to eliminate or reduce significantly

proton currents through the channels. Here, I used an experimental strategy that enabled me to detect and characterize the H_v1 charge displacement. Since the kinetics of proton currents in the monomeric form of the channel develop much faster than those in the dimer (**Fig. 2.6** and **2.7**) implying a faster increase in the H_v1 voltage-dependent open probability, I expected to find gating currents faster and with larger amplitudes. Also, to minimize the proton currents, I used the monomeric low-conducting mutant N264R (**Fig. 2.6c** and **2.7**). To compare the channel opening voltage dependence, I measured the conductance-voltage (G-V) curves in dimeric and monomeric channels (**Fig. 2.7** and **2.8**). Note that the G-V curves in the wild-type channels needed a different voltage pulse protocol because proton depletion can occur in this case (**Fig. 2.7**). This phenomenon, evidenced by a decrease in the proton currents (**Fig. 2.6b**), is produced due to changes in the local concentration of protons (De-la-Rosa et al., 2016). These results showed that both the dimeric and monomeric N264R mutant proton currents have almost the same voltage dependence as the wild-type forms of H_v1 (**Fig. 2.7** and **2.8**). Therefore, the mutation N264R in H_v1 does not alter the steady-state properties of the channel activation.

Gating currents must obey certain rules demanded by the confined space in which they move. First, the charge versus voltage (Q-V) curve should saturate at high voltages at which all voltage sensors are activated. Second, gating currents should become larger and faster as the voltage is increased; i.e., the gating currents kinetics is voltage-dependent (Chandler et al., 1976). Third, all the charge displaced during the ON must be recovered during the OFF. In the N264R mutant, I isolated the gating currents analytically, and the resulting non-linear currents displayed kinetics and voltage dependence that satisfied the first two criteria. However, the OFF represented only 1.4 % of the ON-gating charges. This phenomenon reminded me of charge-immobilization first reported for

sodium channels (Armstrong and Bezanilla, 1977). Here I prefer to use the concept of trapping since modeling of the gating kinetics data suggests that upon activation charge needs to surmount a large barrier to return to its initial configuration (see below). Therefore, these results show that the monomeric N264R H_v1 mutant is a suitable model for studying the channel gating currents.

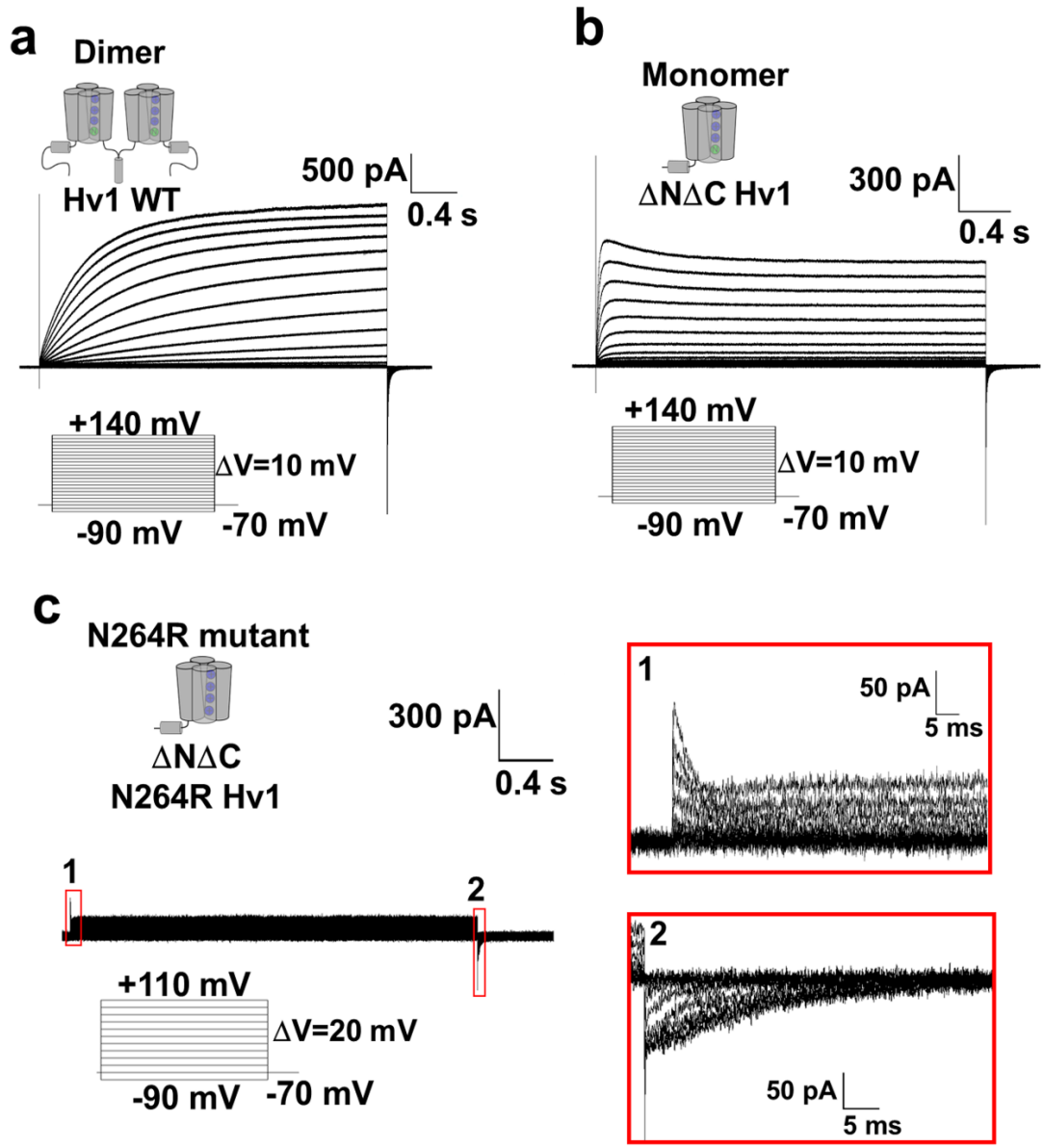

Figure 2.6. Monomeric H_v1 mutant N264R has a fast gating and an impaired conductance. (a) Superimposed current traces produced by the dimeric H_v1 channel under voltage clamp. Note the slow gating of the channel and the proton depletion at the

end of the pulses. (b) Superimposed current traces produced by the monomeric H_v1. Note how the currents reach a maximum at short times, and then decreased to reach a steady-state as a consequence of proton depletion. (c) Superimposed current traces of the monomeric H_v1 mutant N264R show a small ion current. Insets show the ON-gating current (1) and the tail current (2). Linear capacitive currents were subtracted using a P/-8 protocol on figure (c).

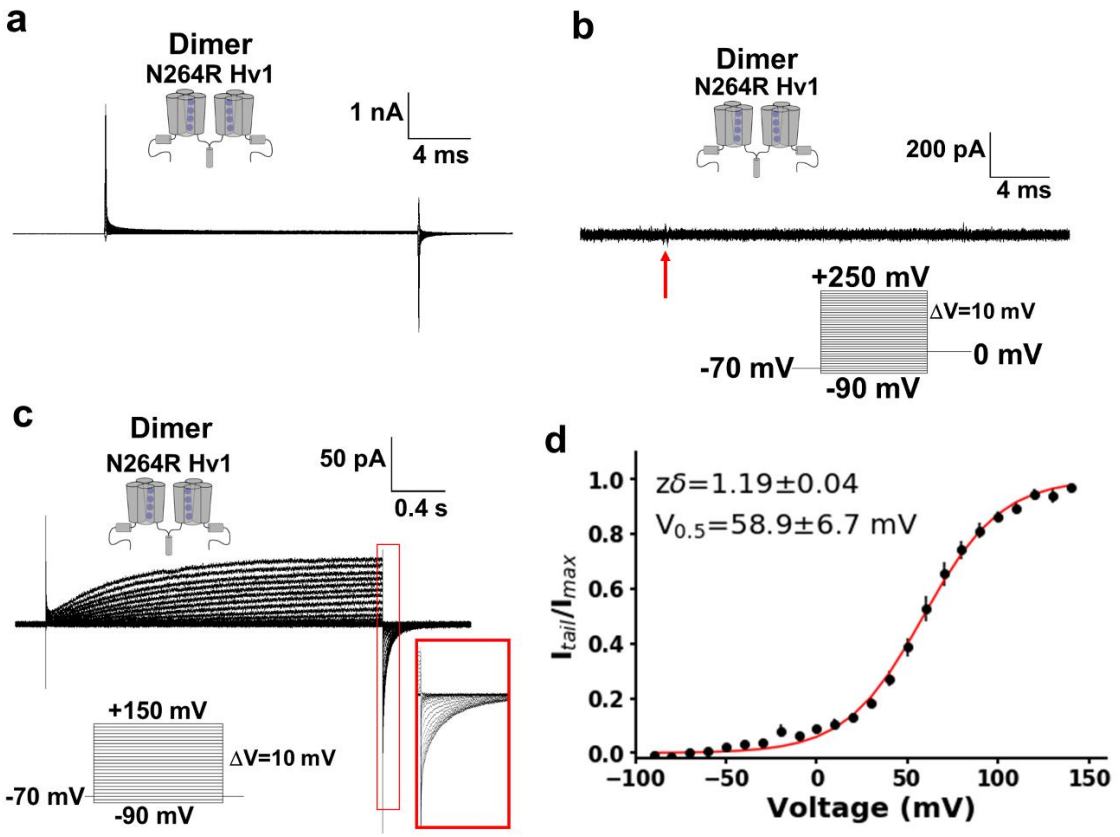

Figure 2.7. Absence of gating currents in the dimeric H_v1 N264R mutant channel. (a) Superimposed current traces of the dimeric N264R channel. (b) Superimposed current traces showed in (a) after subtraction of the linear capacitive currents using a P/-8 protocol. (c) Superimposed current traces of the dimeric N264R mutant channel. Increasing the voltage pulse duration reveals ion currents with a slow time course with time constants similar to those found for the dimeric wild-type H_v1 channel. (d) Normalized tail currents of dimeric H_v1 mutant N264R (black dots). Data were fitted using a Boltzmann function (red line). The apparent number of gating charges ($z\delta$) and the half voltage ($V_{0.5}$) obtained from the fit are shown in the figure (N=5).

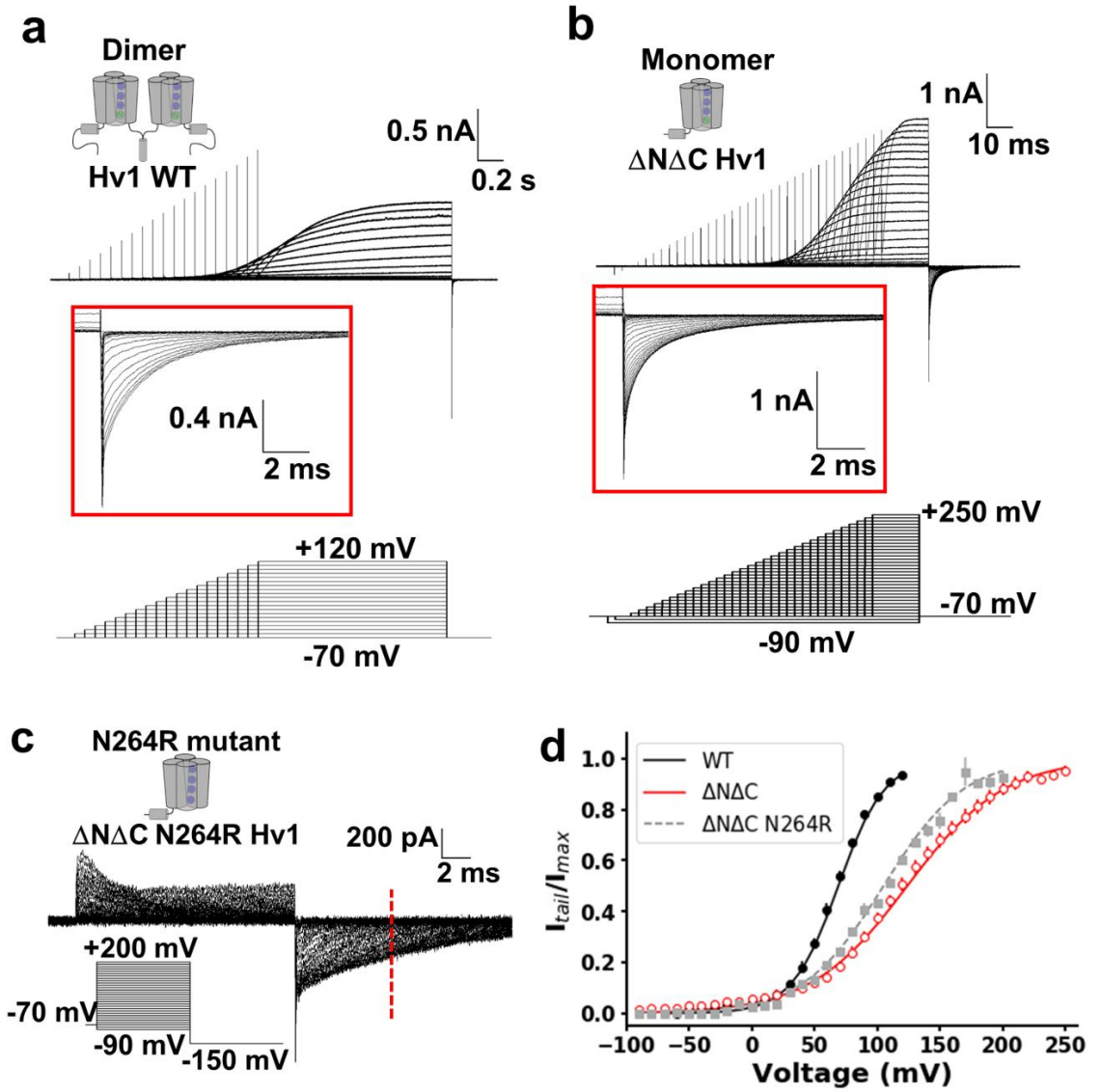

Figure 2.8. Voltage activation in monomeric H_v1 mutant N264R is similar to the wild-type monomer. (a) Superimposed current traces of the H_v1 channel (dimer) showing a representative protocol of depolarizing steps of decreasing duration to avoid proton depletion. The inset shows the tail currents. (b) Superimposed current traces of the monomeric H_v1 channels showing a representative protocol of depolarizing steps of decreasing duration. This protocol was used to avoid changes in the local proton concentration during activation (proton depletion). The inset shows the tail currents. (c) Superimposed current traces of the monomeric H_v1 mutant N264R showing a representative protocol to obtain the tail currents of the channel. To increase the magnitude of the currents and avoid contamination with OFF-gating currents, the tail currents were measured at -150 mV and 6 ms after the depolarizing pulse was turned off (broken red line). Linear capacitive currents were subtracted by a P/-8 protocol. (d) Normalized tail currents of dimeric H_v1 (WT, black circles), monomeric H_v1 (ΔNΔC, red open circles), and monomeric H_v1 mutant N264R (ΔNΔC N264R, grey squares). The data

were fitted with a Boltzmann function obtaining the parameters $V_{0.5}$ = 67.0 ± 3.9 mV and $z\delta$ = 1.37 ± 0.03 for the dimeric H_v1 (*N*=5), $V_{0.5}$ = 121.0 ± 7.9 mV and $z\delta$ = 0.66 ± 0.01 for the monomeric H_v1 (*N*=4), $V_{0.5}$ = 106.6 ± 5.6 mV and $z\delta$ = 0.80 ± 0.02 for the monomeric H_v1 mutant N264R (N=5).

2.5.2 A two-state model is not enough to recapitulate gating charge displacement in H_v1 channels

To analyze isolated gating currents, I assumed a two-state model resting (A) - active (B). However, a closer inspection of the data suggests that the movement of the voltage sensor in monomeric H_v1 is more complex than a two-state process. The first observation that calls the attention is the fact that only a very small fraction of the ON-gating charge is recovered in the OFF (**Fig. 2.3c**), suggesting that the return of the charge to the resting state is very slow indeed. Actually, the double pulse experiments in **Fig. 2.4** suggest that to return to the resting state, the voltage sensor needs to undergo at least two transitions, $A \leftrightarrow B_1 \leftrightarrow B_2$, where A is the resting state, and that a large energy barrier separates states A from B_1. The fast transition seen in the OFF is determined by the B_2 to B_1 transition and the slow charge return, defined by the 88 ms time constant (**Fig 2.4c**), represents the transition from B_1 to A. However, the presence of two peaks in the ON-gating current and the pronounced Cole-Moore effect also suggest that to reach state B_1, the voltage sensor undergoes first a fast transition defining the first peak A_1-A_2 and a slower transition A_2-A_3 before reaching the B_1 state. Therefore, charge trapping is a consequence of the large energy barrier separating states A_3 from B_1 (see below). Against a two-state model is also the fact that the Boltzmann describing the Q-V curve yield a $z\delta$ close to 1 (**Fig. 2.2**), in contrast to the limiting slope experiments that sets a lower limit to near 3 gating charges per monomeric H_v1 channel (Gonzalez et al., 2010). This discrepancy suggests that there is more than one step involved in voltage sensor activation (Bezanilla and Villalba-Galea,

2013). Despite this, the proposed model seems to conflict with another H_v1 gating current measurement (De La Rosa and Ramsey, 2018b).

While these thesis results were being analyzed, detection of gating currents in the dimeric human proton channel mutant W207A-N214R (W257A-N264R in *Ciona*-H_v1) was reported (De La Rosa and Ramsey, 2018b). The method used by the authors to measure gating currents was stepping to a depolarizing voltage from different holding potentials, which is essentially a “Cole-Moore” protocol. Surprisingly, the gating current data does not show a Cole-Moore effect like the one reported here. This is an unexpected result considering that the data also indicate that the gating currents kinetics is defined by multiple states (De La Rosa and Ramsey, 2018b). However, the lack of a well-defined Cole-Moore effect is probably caused by the W207A mutation fast activation kinetics (Cherny et al., 2015). In this respect, my approach to measuring H_v1 gating currents seems to maintain better wild-type channel characteristics.

2.5.3 A five-state model reproduced H_v1 gating currents features

I propose a sequential model for the movement of the monomeric H_v1 voltage sensor consisting of five states (A_1, A_2, A_3, B_1, and B_2) separated by four transitions (**Fig. 2.9, 2.10, and Table 2.1**). States A_1 to A_3 are revealed during H_v1 channel activation (**Fig. 2.4d and 2.5**) and B_1 and B_2 during channel deactivation (**Fig. 2.4a and b**). Gating currents simulated from our five-state model presented two peaks of currents in the ON and only a fast component in the OFF (**Fig 2.9b**), reproducing the experimental currents. Additionally, it can reproduce the gating currents observed during activation and deactivation and the Cole-Moore effect at different prepulse voltages (**Fig. 2.9c-e**). Our model showed that the kinetics of the ON-gating current is dominated by the highest energy barrier placed between A_3 and B_1 (32 kJ/mol). Application of a 150 mV pulse

decreases this energy to 17 kJ/mol, but upon returning to -70 mV, the charge needs to surmount a 27 kJ/mol barrier hight to return from B_1 to the A_3 state (**Fig. 2.9f**). This activation energy difference predicts an A_3 to B_1 charge movement at 150 mV to be 27 times faster than the B_1 to A_3 movement at -70 mV. Our results indicate that the difference between the slow kinetic component of the ON (4 ms) is 22 times faster than the slow OFF component (88 ms; cf., **Fig 2.2d** with **Fig. 2.4c**), which is in reasonable agreement with the calculation using the five-state model. However, it is important to note that this model was obtained by a qualitative reproduction of the main characteristics of the measured gating currents, and then its quantitative interpretation is limited.

Table 2.1. Parameters of the H_v1 gating model. Parameters used in the simulations of the five-state H_v1 gating model. The model and the meaning of the parameters are defined in Section 2.3.4. of Materials and Methods.

Transition	α_0 (ms^{-1})	β_0 (ms^{-1})	$z\delta$	x
$A_1 \rightleftharpoons A_2$	0.5	12	0.2	0.5
$A_2 \rightleftharpoons A_3$	2.4	1	0.1	0.5
$A_3 \rightleftharpoons B_1$	0.002	0.01	1.2	0.85
$B_1 \rightleftharpoons B_2$	3	5	0.18	0.5

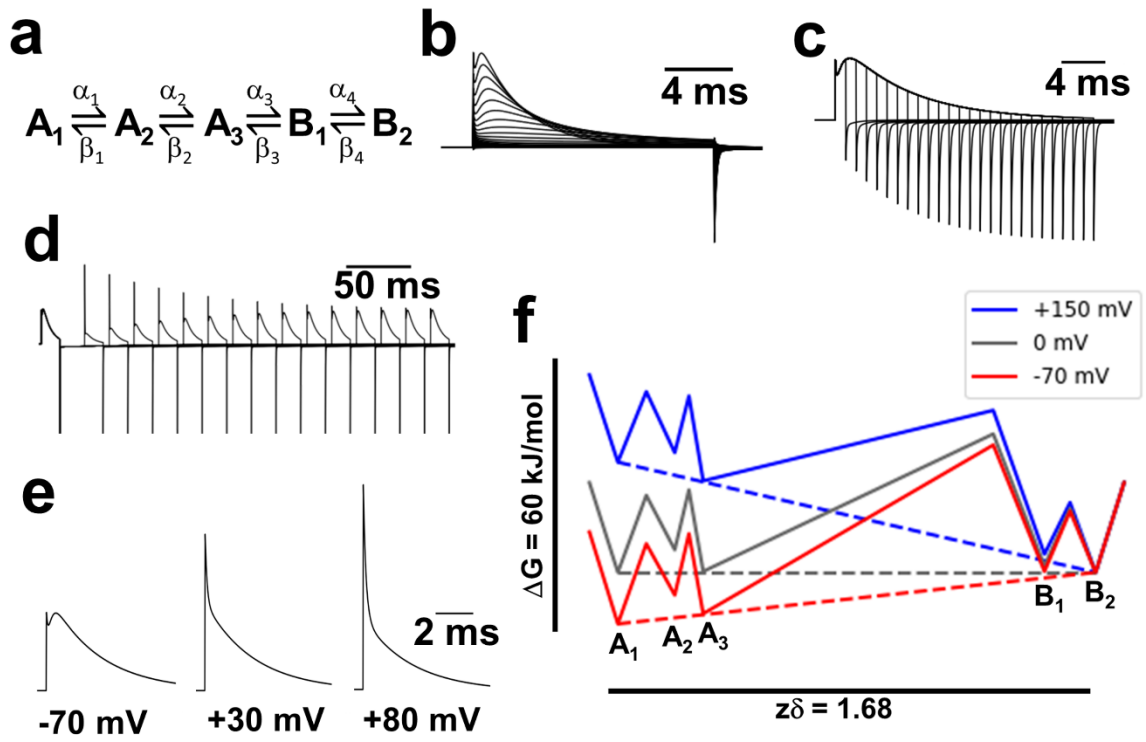

Figure 2.9. A five-state model can reproduce the features of the H_v1 gating currents. (a) The five-state sequential model used to simulate H_v1 gating currents. Rates and voltage dependence of each transition are given the Table 2.1 by the equations defined in Section 2.3.4. of Materials and Methods. (b) Superimposed simulated traces of gating currents produced by the model. A prepulse at -70 mV was followed by a series of voltage steps from -90 to 200 mV in 10 mV increments and repolarization to 0 mV. Note the presence of two peaks during the ON-gating current, and the large difference between the gating charge displaced during the ON and OFF components. (c) Superimposed simulated traces of depolarizations at 150 mV of increasing duration produced a fast OFF component that increases at short depolarizations to reach a plateau during repolarization at 0 mV, similar to Fig. 2.3b. Holding potential is -70 mV and the time interval of depolarization increased 1 ms between current traces. (d) Superimposed simulated traces of the ON recovery protocol similar to the protocol of Fig. 2.4b. Holding potential is -70 mV, and depolarizations were produced at 150 mV. The time interval between depolarizations increases 20 ms between traces. (e) Simulated traces of thee ON-gating current produced with a depolarization at 200 mV from a prepulse at the indicated voltage. Note that, similar to the result showed in Fig 2.4d, the two peaks of current in the ON change to one and the kinetics of decay get faster as the prepulse voltage increases. (f) Energy barriers produced by the five-state model at three different voltages. The reaction coordinate (horizontal axis) is the gating charge displaced during the process and the voltage differences were applied relative to the final state B_2.

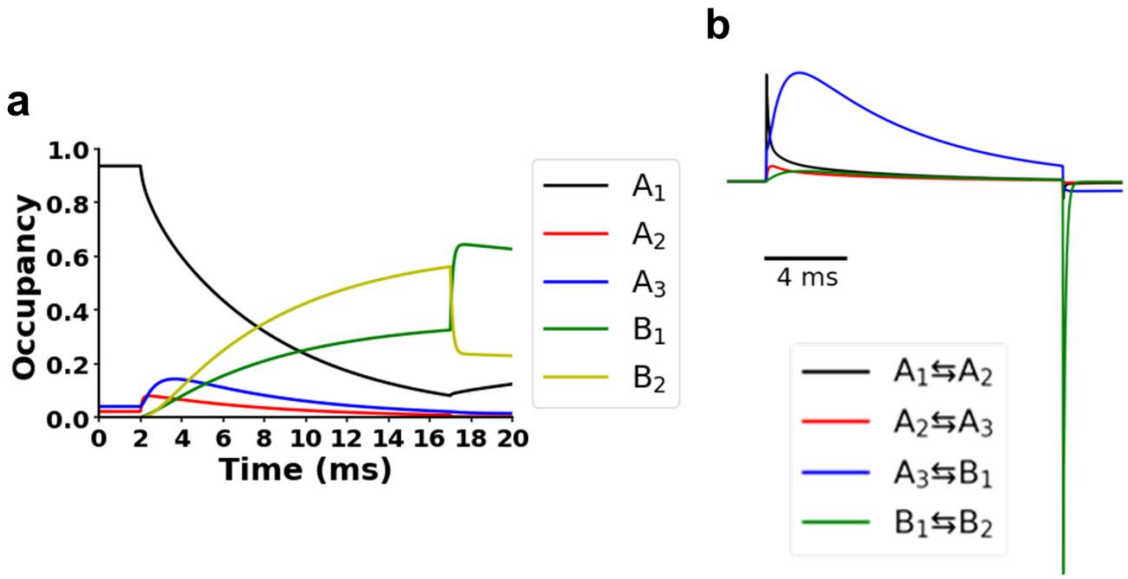

Figure 2.10. Predicted occupancy and time course of the charge displace between the different transitions of the five-state model. (a) Occupancy of the different states during a depolarizing pulse of 150 mV (t = 2 to 17 ms) a holding potential of -70 mV. Note that at the holding potential, the channels are principally in the A_1 state, but a small percentage of channels are also occupying the A_2 and A_3 states. States B_1 and B_2 are not occupied at this voltage. The small energy barriers between these three states and the high energetic barrier separating them from the states B_1 and B_2 can account for this initial occupancy distribution (Fig. 2.9d). When the voltage changes to 150 mV (2 ms), the occupancy of A_1 decreases to populate the other four states. The state A_2 is populated quickly, to reach a low maximum occupancy and started to decrease slowly. Something similar happens with the A_3 state, but the occupancy increases at a slower pace and reaches a greater maximum occupancy than the preceding state. Meanwhile, both states B_1 and B_2 begins to populate slowly. At the end of the depolarizing pulse, B_2 state has the greatest occupancy followed by B_1 state. The net result of depolarization then is a change of occupancy mainly from A_1 to B_1 and B_2. When the voltage imposed returns to the holding value, there is a rapid change of occupancy from B_2 to B_1 due to the small energy barrier between these states. However, channels become trapped between these states due to the high energy barrier separating B_1 from A_3 (Fig. 2.9d). (b) The contribution of each transition to the final gating current shows that during the depolarization at 150 mV from a holding potential of -70 mV most of the current is produced by the slower transition from A_3 to B_1 (blue trace), with all the other states contributing with very small percentages to the final gating current. Note that the fast gating current during the depolarization is due to the transition from A_1 to A_2 (black trace), which at this voltage originates the first peak of current, while the second one is due to the delayed current produced by the slower transition. During repolarization, the fast change of occupancy from B_2 to B_1 causes the fast transient inward gating current (green trace), while a second slower and smaller component is developed by the return from B_1 to A_3 (blue trace).

2.5.4 A new H_v1 channel kinetic model is needed

A previous report showed that a fluorophore attached to the S4 voltage sensor in dimeric H_v1 channels revealed two S4 charge movements (Qiu et al., 2013). The first movement precedes channel opening with S4 charge movements in both subunits independently, and the second one correlates with channel opening, defined as the fluorescence hook (Qiu et al., 2013). To make it compatible with my proposed model, only B_2 in the present model would be correlated with an open channel. Then, the hook would be the transition from B_2 to B_1, which is fast and closes the channel, while transition B_1 to A_3 would be the main S4 transition, which is slow. In the kinetic model of dimeric H_v1 (Qiu et al., 2013), voltage sensor movement involved three closed and one open state, where the movement of both voltage sensors within the dimer is necessary before the opening of the permeation pathway of each subunit (Qiu et al., 2013). Here I found that each independent H_v1 voltage sensor transits through different states, suggesting that the movement of charge is more complex than previously thought. The most significative fact is that more than 50% of gating charge displacement, on the monomeric H_v1 channel, occurs before opening (in 5 ms at 150 mV, when the open probability of the monomeric H_v1 channel is only 0.2, 65% of the gating charge has been displaced). However, in view that dimer formation confers a cooperative gating to H_v1, it could be possible that dimeric move different than monomeric voltage sensors (Gonzalez et al., 2010).

2.5.5 Molecular mechanism for trapping

I envision that the rate-limiting step that keeps the charges from returning to its resting configuration involves a blocked-like phenomenon mediated by the arginine side chain, much like the documented blockade of H_v1 channels by guanidinium reagents (Hong et

al., 2014; Hong et al., 2013; Hong et al., 2015). Moreover, as reported before using the dimeric human H_v1 mutant N214R (Ramsey et al., 2010; Ramsey et al., 2006) and mouse mutant N210R (Sakata et al., 2010), I found that the N264R mutant open channel behaves as an inward rectifier (**Fig. 2.11**). Blockade by the positively charged arginine located in the internal vestibule of the channel should be relieved by hyperpolarizing voltages, and the mutant channel should behave as an inward rectifier as found experimentally (**Fig. 2.11**). I should also consider that the mutation introduced at position 264 can decrease proton currents by changing the electrostatic potential in the neighborhood of the H_v1 channel internal entrance. Although my data indicate that the N264 mutant does not modify the channel voltage dependence (**Fig. 2.7** and **2.8**), measurements of this position accessibility to thiol-modifying agents showed to be state-dependent. However, structural models suggest that this position is outside the electric field (Gonzalez et al., 2013; Takeshita et al., 2014), but more experiments are needed to confirm this claim. Finally, the inspection of the proton current recording of the monomeric *Ciona*-N264R mutant suggests that the positively charged guanidinium stabilizes the closed state of the channel, making the channel deactivation slower for the dimeric and monomeric *Ciona*-H_v1 (**Fig. 2.7 and 2.11**), and on the dimeric mouse and human H_v1 containing the equivalent N210R (Sakata et al., 2010) and N214R (Ramsey et al., 2010) mutation, respectively. A possible explanation to these findings is that the gating charge is trapped when the channel is activated upon depolarization, and it recovered slowly during the repolarization process, as I showed in this study.

I conclude that trapping is a consequence of the presence of the charged arginine chain in position 264. Given the fast deactivation rate shown by the wild-type monomeric H_v1 channel, the presence of a neutral asparagine in that position may have the effect of

collapsing the barrier that separates states A_3 from B_1. Further experiments are needed to test this hypothesis and to check the generality of the gating kinetics model I proposed here.

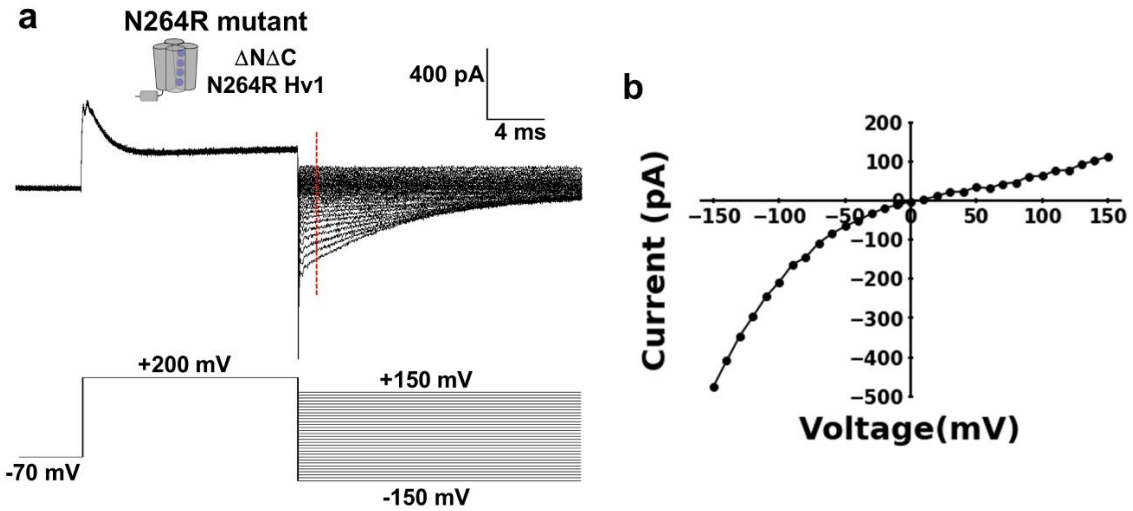

Figure 2.11. Monomeric H_v1 mutant N264R is an inward rectifier. (a) Superimposed current traces of the monomeric H_v1 mutant N264R produced by the protocol showed on the lower part of the figure. Values of the tail currents in (b) were obtained at the time defined by the isochrone indicated by the broken red line. (b) The current-voltage curve obtained as described in (a) shows a clear inward rectification.

2.6 References

Aggarwal, S.K., and MacKinnon, R. 1996. Contribution of the S4 segment to gating charge in the Shaker K+ channel, *Neuron* 16, 1169-1177.

Alvarez, O., Castillo, K., Carmona, E., Gonzalez, C., and Latorre, R. 2019. Methods for Investigating TRP Channel Gating, *Methods Mol Biol* 1987, 167-185.

Armstrong, C.M., and Bezanilla, F. 1973. Currents related to movement of the gating particles of the sodium channels, *Nature* 242, 459-461.

Armstrong, C.M., and Bezanilla, F. 1977. Inactivation of the sodium channel. II. Gating current experiments, *J Gen Physiol* 70, 567-590.

Baez-Nieto, D., Otarola, E., Contreras, G., Larsson, P., Latorre, R., and Gonzalez, C. 2014. Gating Currents of Monomeric Hv Channel Reveals a Permeation Pathway Coupled to the Voltage Activation, *Biophysical Journal* 106, 233a-233a.

Bezanilla, F., and Villalba-Galea, C.A. 2013. The gating charge should not be estimated by fitting a two-state model to a Q-V curve, *J Gen Physiol* 142, 575-578.

Carmona, E.M., Baez-Nieto, D., Pupo, A., Castillo, K., Alvarez, O., Neely, A., Latorre, R., and Gonzalez, C. 2018. Properties of the Voltage-Gated Proton Channel Gating Currents, *Biophysical Journal* 114, 546a.

Cha, A., and Bezanilla, F. 1997. Characterizing voltage-dependent conformational changes in the Shaker K+ channel with fluorescence, *Neuron* 19, 1127-1140.

Chandler, W.K., Rakowski, R.F., and Schneider, M.F. 1976. A non-linear voltage dependent charge movement in frog skeletal muscle, *J Physiol* 254, 245-283.

Cherny, V.V., Markin, V.S., and DeCoursey, T.E. 1995. The voltage-activated hydrogen ion conductance in rat alveolar epithelial cells is determined by the pH gradient, *J Gen Physiol* 105, 861-896.

Cherny, V.V., Morgan, D., Musset, B., Chaves, G., Smith, S.M., and DeCoursey, T.E. 2015. Tryptophan 207 is crucial to the unique properties of the human voltage-gated proton channel, hHV1, *J Gen Physiol* 146, 343-356.

Cherny, V.V., Murphy, R., Sokolov, V., Levis, R.A., and DeCoursey, T.E. 2003. Properties of single voltage-gated proton channels in human eosinophils estimated by noise analysis and by direct measurement, *J Gen Physiol* 121, 615-628.

Cole, K.S., and Moore, J.W. 1960. Potassium ion current in the squid giant axon: dynamic characteristic, *Biophys J* 1, 1-14.

Colquhoun, D., and Hawkes, A.G.: A Q-Matrix Cookbook, In Sakmann B., and Neher E., editors: *Single-Channel Recording*, Boston, MA, 1995, Springer US, pp. 589-633.

De-la-Rosa, V., Suarez-Delgado, E., Rangel-Yescas, G.E., and Islas, L.D. 2016. Currents through Hv1 channels deplete protons in their vicinity, *J Gen Physiol* 147, 127-136.

De La Rosa, V., and Ramsey, I.S. 2018a. Gating Currents in Hv1 Proton Channels, *Biophysical Journal* 114, 124a.

De La Rosa, V., and Ramsey, I.S. 2018b. Gating Currents in the Hv1 Proton Channel, *Biophys J* 114, 2844-2854.

DeCoursey, T.E. 2018. Voltage and pH sensing by the voltage-gated proton channel, HV1, *J R Soc Interface* 15.

DeCoursey, T.E., and Cherny, V.V. 1994. Voltage-activated hydrogen ion currents, *J Membr Biol* 141, 203-223.

Fujiwara, Y., Kurokawa, T., Takeshita, K., Kobayashi, M., Okochi, Y., Nakagawa, A., and Okamura, Y. 2012. The cytoplasmic coiled-coil mediates cooperative gating temperature sensitivity in the voltage-gated H(+) channel Hv1, *Nat Commun* 3, 816.

Gandhi, C.S., and Olcese, R.: The Voltage-Clamp Fluorometry Technique, In Lippiat J.D., editor. *Potassium Channels: Methods and Protocols*, Totowa, NJ, 2009, Humana Press, pp. 213-231.

Gonzalez, C., Koch, H.P., Drum, B.M., and Larsson, H.P. 2010. Strong cooperativity between subunits in voltage-gated proton channels, *Nat Struct Mol Biol* 17, 51-56.

Gonzalez, C., Rebolledo, S., Perez, M.E., and Larsson, H.P. 2013. Molecular mechanism of voltage sensing in voltage-gated proton channels, *J Gen Physiol* 141, 275-285.

Gonzalez, C., Rosenman, E., Bezanilla, F., Alvarez, O., and Latorre, R. 2000. Modulation of the Shaker K(+) channel gating kinetics by the S3-S4 linker, *J Gen Physiol* 115, 193-208.

Hilgemann, D.W.: The Giant Membrane Patch, In Sakmann B., and Neher E., editors: *Single-Channel Recording*, Boston, MA, 1995, Springer US, pp. 307-327.

Hong, L., Kim, I.H., and Tombola, F. 2014. Molecular determinants of Hv1 proton channel inhibition by guanidine derivatives, *Proceedings of the National Academy of Sciences of the United States of America* 111, 9971-9976.

Hong, L., Pathak, M.M., Kim, I.H., Ta, D., and Tombola, F. 2013. Voltage-sensing domain of voltage-gated proton channel Hv1 shares mechanism of block with pore domains, *Neuron* 77, 274-287.

Hong, L., Singh, V., Wulff, H., and Tombola, F. 2015. Interrogation of the intersubunit interface of the open Hv1 proton channel with a probe of allosteric coupling, *Scientific reports* 5, 14077.

Koch, H.P., Kurokawa, T., Okochi, Y., Sasaki, M., Okamura, Y., and Larsson, H.P. 2008a. Multimeric nature of voltage-gated proton channels, *Proc Natl Acad Sci U S A* 105, 9111-9116.

Koch, H.P., Kurokawa, T., Okochi, Y., Sasaki, M., Okamura, Y., and Larsson, H.P. 2008b. Multimeric nature of voltage-gated proton channels, *Proceedings of the National Academy of Sciences* 105, 9111-9116.

Larsson, H.P., Baker, O.S., Dhillon, D.S., and Isacoff, E.Y. 1996. Transmembrane movement of the shaker K+ channel S4, *Neuron* 16, 387-397.

Lee, S.Y., Letts, J.A., and Mackinnon, R. 2008. Dimeric subunit stoichiometry of the human voltage-dependent proton channel Hv1, *Proceedings of the National Academy of Sciences of the United States of America* 105, 7692-7695.

Mannuzzu, L.M., Moronne, M.M., and Isacoff, E.Y. 1996. Direct physical measure of conformational rearrangement underlying potassium channel gating, *Science* 271, 213-216.

Mony, L., Berger, T.K., and Isacoff, E.Y. 2015. A specialized molecular motion opens the Hv1 voltage-gated proton channel, *Nat Struct Mol Biol* 22, 283-290.

Musset, B., Smith, S.M., Rajan, S., Morgan, D., Cherny, V.V., and Decoursey, T.E. 2011. Aspartate 112 is the selectivity filter of the human voltage-gated proton channel, *Nature* 480, 273-277.

Qiu, F., Rebolledo, S., Gonzalez, C., and Larsson, H.P. 2013. Subunit interactions during cooperative opening of voltage-gated proton channels, *Neuron* 77, 288-298.

Ramsey, I.S., Mokrab, Y., Carvacho, I., Sands, Z.A., Sansom, M.S.P., and Clapham, D.E. 2010. An aqueous H+ permeation pathway in the voltage-gated proton channel Hv1, *Nat Struct Mol Biol* 17, 869-875.

Ramsey, I.S., Moran, M.M., Chong, J.A., and Clapham, D.E. 2006. A voltage-gated proton-selective channel lacking the pore domain, *Nature* 440, 1213-1216.

Sakata, S., Kurokawa, T., Norholm, M.H., Takagi, M., Okochi, Y., von Heijne, G., and Okamura, Y. 2010. Functionality of the voltage-gated proton channel truncated in S4, *Proceedings of the National Academy of Sciences of the United States of America* 107, 2313-2318.

Sasaki, M., Takagi, M., and Okamura, Y. 2006. A voltage sensor-domain protein is a voltage-gated proton channel, *Science* 312, 589-592.

Seoh, S.A., Sigg, D., Papazian, D.M., and Bezanilla, F. 1996. Voltage-sensing residues in the S2 and S4 segments of the Shaker K+ channel, *Neuron* 16, 1159-1167.

Takeshita, K., Sakata, S., Yamashita, E., Fujiwara, Y., Kawanabe, A., Kurokawa, T., Okochi, Y., Matsuda, M., Narita, H., Okamura, Y., and Nakagawa, A. 2014. X-ray crystal structure of voltage-gated proton channel, *Nat Struct Mol Biol* 21, 352-357.

Tombola, F., Ulbrich, M.H., and Isacoff, E.Y. 2008. The voltage-gated proton channel Hv1 has two pores, each controlled by one voltage sensor, *Neuron* 58, 546-556.

Vandenberg, C.A., and Bezanilla, F. 1991. A sodium channel gating model based on single channel, macroscopic ionic, and gating currents in the squid giant axon, *Biophys J* 60, 1511-1533.

CHAPTER 3

THE pH MODULATION OF THE VOLTAGE SENSOR IN THE VOLTAGE-GATED PROTON CHANNEL (H_V1)

3.1 Abstract

The voltage-gated proton channel (H_v1) is a dimeric membrane protein that dissipates acute acid loads in cells. This function relies on regulating the channel open probability by both the voltage and the pH difference ($\Delta pH = pH_{out} – pH_{in}$) established across the membrane. The H_v1 dependence on ΔpH instead of internal or external pH has been challenging to explain. To study this property, I measured the pH dependence of gating currents in the monomeric D160N H_v1 mutant, which is a non-conducting channel. The gating charge-voltage curves were shifted according to the ΔpH value, suggesting that the ΔpH determines the initial and final states of the voltage sensor domain (VSD) during activation. Although a positive ΔpH value increased the VSD activation rate, gating currents kinetics depended on the internal and external pH. Moreover, gating currents deactivation kinetics evidenced a voltage-independent transition modulated by the internal and external pH. Therefore, the H_v1 VSD has an intrinsic state-dependent pH modulation that favors its activation and channel opening.

3.2 Introduction

The primary physiological function of the voltage-gated proton channel (H_v1) is proton extrusion of acute acid loads. This role is evident during the respiratory burst in macrophages, where H_v1 dissipates the proton gradient established by the NADPH oxidase to produce superoxide radicals (DeCoursey et al., 2000; Okochi et al., 2009; Ramsey et al., 2009). This function is a consequence of the unique structure and biophysical properties of the channel. Other voltage-gated ion channels have a voltage

sensor domain (made up of transmembrane segments S1 to S4) coupled to a pore domain (S5 to S6) (Hille, 2001). However, H_v1 contains only a voltage sensor domain (VSD) flanked by intracellular N- and C-terminal domains (Ramsey et al., 2006; Sasaki et al., 2006). The C-terminal domain forms a coiled-coil structure between two H_v1 subunits to form a dimer (Koch et al., 2008; Lee et al., 2008). H_v1 lacks the pore domain present in other voltage-gated ion channels, so the permeation pathway is contained in its VSD. Accordingly, the monomeric H_v1, which has the N- and C-terminal domains deleted, is also a voltage-gated proton channel (Koch et al., 2008). H_v1 is highly selective to protons (Musset et al., 2011) and has a small unitary conductance (Cherny et al., 2003; DeCoursey and Cherny, 1994). Channel opening is cooperative (Gonzalez et al., 2010; Tombola et al., 2008) and voltage-dependent (Gonzalez et al., 2013; Tombola et al., 2010). However, the most remarkable property of the channel is its pH-dependence (DeCoursey, 2018).

Since the first measurements of voltage-gated proton currents from different preparations, it has been evident that H_v1 channels are modulated by pH (Barish and Baud, 1984; Bernheim et al., 1993; Byerly et al., 1984; DeCoursey, 1991; Kapus et al., 1993). However, the technical difficulties of controlling the pH during proton current measurements were only overcome in a study using alveolar epithelial cells, in which pH values were confirmed by comparing the reversal potential with the equilibrium potential for protons (Cherny et al., 1995). This detailed study unveiled the properties of the pH dependence of H_v1 gating. First, the conductance versus voltage (G-V) curves shifted according to the ΔpH ($pH_{out} - pH_{in}$) established across the membrane regardless of the internal or external pH value. However, a saturation of the shift was observed at pH values greater than 8. Second, the kinetics of activation also shifted according to the ΔpH,

similarly to what happened with the G-V curves. The discovery of the H_v1 gene (Ramsey et al., 2006; Sasaki et al., 2006) makes it possible to study these properties in heterologous systems A series of acidic and basic channel residues were replaced by alanine, but none of these mutations abolished the pH dependence completely (Ramsey et al., 2010). Despite this, recent studies have found mutations that modified this channel property. The change of a conserved tryptophan in S4 (W207 in human H_v1) results in an altered pH_{out} dependency without modifying the effect of pH_{in} (Cherny et al., 2015). A second mutation involves the replacement of the histidine 168 in human H_v1 (hH_v1), which decreases the G-V curve shifts by ΔpH only when pH_{in} is changed (Cherny et al., 2018). Another reported alteration of the hH_v1 pH dependence occurs when the first 68 amino acids of the channel N-terminal domain are deleted. In this shorter channel, the G-V curve shifts decrease when pH_{in} is changed, and different locations in the voltage axis of the curves are observed at ΔpH=0 (Berger et al., 2017). All these results suggest that H_v1 has independent internal and external pH sensors. It has been proposed that these pH sensors are a series of protonatable negatively charged residues in S1, S2, and S3 (DeCoursey, 2018). The complexity of the problem increased with the cooperative gating of the dimer (Gonzalez et al., 2010; Tombola et al., 2010) and the multiple states involving the VSD movement (Carmona et al., 2018).

The pH dependence of H_v1 has been difficult to understand because its study has involved proton currents of the dimeric channel. The dimeric channel currents make it very difficult to separate the effects of pH on the cooperativity of gating, the VSD movement, and the channel opening. There is evidence indicating that pH affects both the VSD movement (De La Rosa and Ramsey, 2018) and the unitary conductance (Cherny et al., 2003) of the channel. However, a detailed study of the former at different

pH and ΔpH values is missing. The monomer of the *Ciona intestinalis* H_v1 (CiH_v1) channel is an excellent candidate to overcome the difficulties imposed using dimeric channels. It allows studying the VSD movements directly through gating current measurements in the absence of cooperativity (Carmona et al., 2018; Koch et al., 2008).

3.3 Materials and Methods

3.3.1 Mutagenesis, transcription, and sequencing. *Ciona intestinalis* H_v1 contained in pSP64T vector was kindly provided by Dr. Okamura. The vector was modified with a stop codon at Val270 and an initiator methionine replacing Glu129 to produce the monomeric H_v1 (Koch et al., 2008). D160 single mutations were introduced using QuickChange kit (Promega Corp.). The resulting DNA was amplified, checked by sequencing, and then linearized with PvuII restriction enzyme. Linearized DNA was used to synthesize RNA with mMESSAGE mMACHINE SP6 transcription kit (Ambion). RNA was quantified by absorbance at 260 nm, and its integrity was checked by electrophoresis in an agarose gel.

3.3.2 Oocytes extraction and RNA injection. *Xenopus laevis* oocytes were obtained and manipulated according to previously described methodologies (Alvarez et al., 2019). They were injected with 50 nL of RNA at a concentration of 1 μg/μL and were incubated at 18 °C for 2 to 3 until they were used for the recordings.

3.3.3 Electrophysiology. Currents were measured in patches of oocyte membranes in the inside-out modality by voltage clamp. Only one experiment was performed in each patch, as I consistently observed a change in the current kinetics and sometimes even shifts of the G-V or Q-V curves when patches were repeatedly depolarized. This phenomenon has been reported by others (Byerly et al., 1984; Cherny et al., 1995). The internal and external solutions contained 100 mM buffer (MES for pH 6.0, HEPES for pH

7.0, and HEPBS or HEPES for pH 8.0), 2 mM $MgCl_2$, 1 mM EGTA, and 50 mM N-methyl-D-glucamine (NMDG)-methanesulfonate. pH was adjusted with NMDG or methanesulphonate. Measurements were performed at room temperature (22 °C). Pipettes of borosilicate capillary glass (1B150F-4, World Precision Instruments) were pulled on a horizontal pipette puller (Sutter Instruments) and fire-polished until a diameter between 15 to 24 µm (resistances of 0.8-1.2 MΩ in the bath solution). Data were acquired with an Axopatch 200B amplifier (Axon Instruments). The voltage command and the current output were filtered at 20 kHz with 8-pole Bessel low-pass filters (Frequency Devices). Analog signals were sampled with a 16-bit A/D converter (Digidata 1440A, Axon Instruments) at 250 kHz. Experiments were performed using Clampex 8 acquisition software (Axon Instruments). Capacitive currents were compensated by analog circuitry, and a -P/8 subtraction protocol was used (Armstrong and Bezanilla, 1973). Data analysis was performed using Python programming language scripts (Python Software Foundation, https://www.python.org/).

3.4 Results

3.4.1 Monomeric H_v1 is a simple model to study the channel pH-dependency

As monomeric H_v1 is still a functional proton channel (Gonzalez et al., 2010; Koch et al., 2008), I thought this could be a simple model for investigating the H_v1 pH dependence. The monomeric channel is pH-dependent (Koch et al., 2008), but there are no detailed studies of this property. I was interested to know if the G-V curves shifted according to the ∆pH as occurs in the dimer. I expressed the monomeric *Ciona intestinalis* H_v1 (CiH_v1) in *Xenopus laevis* oocytes to measure the G-V curves at different pHs and ∆pHs from tail

currents (**Fig. 3.1a-c**). I fitted the tail currents, $I_{tail}(V)$, to a two-state Boltzmann distribution model

$$I_{tail}(V) = \frac{I_{tail,max}}{1+e^{\frac{-z\delta F(V-V_{0.5})}{RT}}} \quad (3.1)$$

where $I_{tail,max}$ is the maximal tail current, $z\delta$ is the voltage-dependence, $V_{0.5}$ is the voltage at which half of the channels are open, and F, R, and T have their usual meanings.

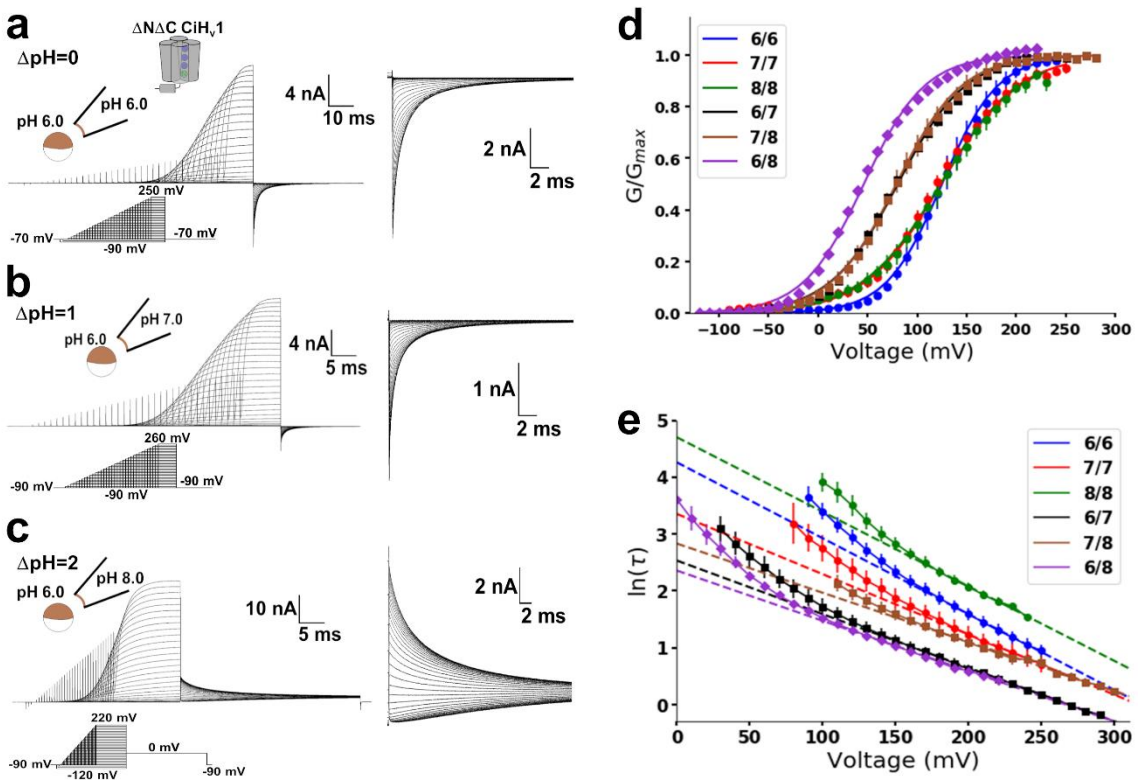

Figure 3.1. Monomeric Hv1 currents are ΔpH-dependent. Representative current recordings of monomeric H_v1 at (a) ΔpH=0, (b) ΔpH=1, and (c) ΔpH=2. The insets show the tail currents in an expanded time and current scale. Note the superposition of tail currents at high voltages suggesting that the open probability reached its maximum value. (d) Mean G-V curves at the indicated pH_{in}/pH_{out} obtained from the tail currents. Curves were fitted using a two-state Boltzmann distribution model (lines; equation 3.1 in text, and Table 3.1). (e) The mean logarithm of the activation time constant as a function of voltage at the indicated pH_{in}/pH_{out}. Dotted lines correspond to a fit of the data at high voltages using equation $ln[\tau(V)/ms] = -(z\delta_{\alpha}e_0/kT)V - ln(\alpha_0\ ms)$ (equation 3.3 in text and Table 3.2). Data are shown as mean ± S.E.M.

To minimize local changes in pH caused by proton fluxes, I used a high concentration of buffer in all solutions to increase the proton transfer rate. Additionally, as the depolarizing voltage increased and higher currents passed through channels, the voltage pulse duration was shortened to avoid depletion or accumulation of protons. I also measured the experimental reversal potential before and after the G-V curve measurement to determine the ΔpH (**Fig. 3.2**).

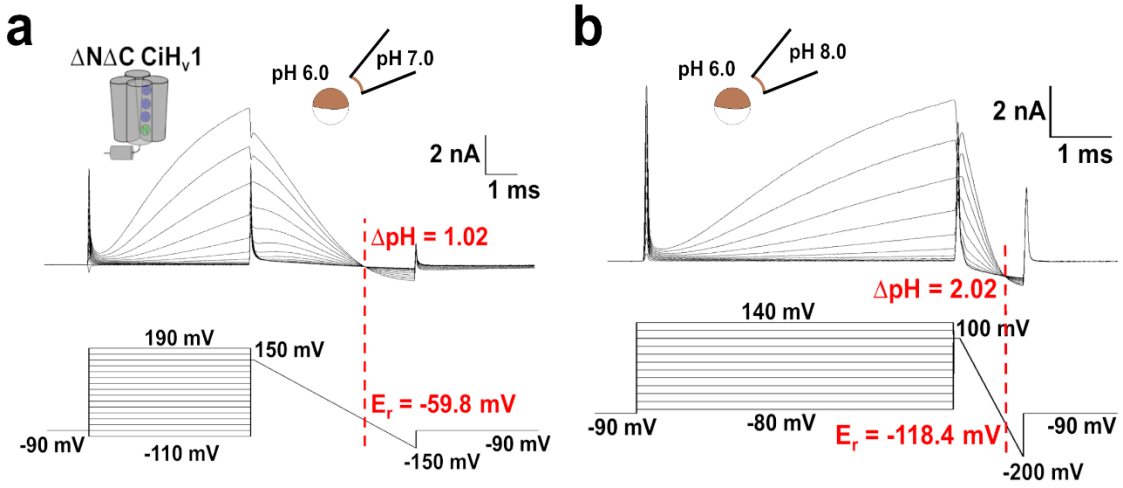

Figure 3.2. Reversal potential measurements were done before and after G-V curves determination. Currents produced by the monomeric H_v1 at (a) ΔpH 1 and (b) ΔpH 2. Representative voltage protocol and determination of the current reversal potential to obtain the experimental ΔpH established across the membrane. It consisted of a series of depolarizations followed by a ramp. The current as a function of time during the ramp is $I(t) = C(dV/dt) + G_{leak}(V-E_{r,leak}) + G(V-E_r)$, where C is the capacitance, V is voltage, G_{leak} is the leak conductance, $E_{r,leak}$ is the reversal potential of the leak conductance, G is the channel voltage-dependent conductance, and E_r is the reversal potential of this channel. The two first terms on the right of the equation for $I(t)$ are the same for all the ramps as dV/dt is constant, and G_{leak} does not depend on voltage. As each depolarization preceding the ramp finished with a different channel open probability of channels, G is different for each ramp. The voltage at which $I(t)$ is equal for all ramps is when $V=E_r$, the reversal potential of the voltage-dependent conductance.

With these precautions, G-V curves shifted to the left as the ΔpH (pH_{out}(high) – pH_{in}(low)) increased regardless of the internal or external pH value (**Fig. 3.1d**). This result was similar to what has been reported for the dimeric H_v1 (Cherny et al., 1995; Cherny et al.,

2015). An increase of two ΔpH units promoted a shift of the $V_{0.5}$ of -79 ± 7 mV (**Table 3.1**). Activation currents (I) were fitted to a single exponential function

$$I(t) = I_{max}\left(1 - e^{-t/\tau}\right) \tag{3.2}$$

where I_{max} is the current at infinite time and τ is the activation time constant. Interestingly, the $\tau(V)$ curves follow a different behavior than the G-V curves (**Fig. 3.1e**). The largest discrepancy occurred at ΔpH=1: Activation time constants at pH_{in}/pH_{out} 7/8 were similar to 7/7 (ΔpH=0), but at 6/7, they almost superimposed with the values obtained at 6/8 (ΔpH=2). Thus, the rate of channel opening is influenced by the internal and external pH instead of the ΔpH. Monomeric H_v1 has more than one closed state (Carmona et al., 2018), so $\tau(V)$ is an unknown function involving parameters of every activation transition. However, at high voltages, $\tau(V)$ is determined mainly by the slowest forward rate, $\alpha(V)$, and therefore

$$\tau(V) \approx \frac{1}{\alpha(V)} = \frac{1}{\alpha_0 e^{\frac{z\delta_\alpha e_0 V}{kT}}} \tag{3.3}$$

where α_0 is the value of the rate constant at 0 mV, $z\delta_\alpha e_0$ is the charge associated with the forward transition, V is the voltage, and k, e_0, and T have their usual meanings. The $\tau(V)$ data at high positive voltages were fitted using equation 3.3 to obtain the parameters α_0 and $z\delta_\alpha$ at different pHs (**Fig. 3.1e and Table 3.2**). The resultant α_0 values did not show a simple relation with ΔpH, but they were about ten-times smaller in symmetrical pH 6 and 8 than the values obtained at ΔpH=2 (pH_{in}/pH_{out}=6/8). On the other hand, the values of $z\delta_\alpha$ at these symmetrical pHs were approximately 55% larger than at ΔpH=2. At ΔpH=1, $z\delta_\alpha$ values were similar to those at ΔpH=2, but the values of α_0 were smaller following the order 6/8 > 6/7 > 7/8 (pH_{in}/pH_{out}). Then, I can separate the kinetic data into

two groups: symmetrical pH 6 and 8 (small values of α_0 and high values of $z\delta_\alpha$) and asymmetrical pHs (high values of α_0 and small values of $z\delta_\alpha$). The values of the kinetic parameters at symmetrical pH 7 were between these two groups. These results showed that a positive pH gradient favors the opening of the H_v1 monomer by increasing the open probability and the slowest forward rate of activation. However, this last change is not a simple function of the ΔpH value but rather a function of the internal and external pH (**Fig. 3.1e**).

Table 3.1. Parameters from the G-V curves fitted to a two-state Boltzmann distribution model at different pHs. G-V curves of the monomeric H_v1 were fitted to $I_{tail}(V) = I_{tail,max}/(1 + exp(-z\delta F(V - V_{0.5})/RT))$. N is the number of replicates of each condition. The function was defined in the text (equation 3.1). Values correspond to mean ± S.E.M.

pH_{in}/pH_{out}	$V_{0.5}$ (mV)	$z\delta$	N
6/6	126 ± 3	0.91 ± 0.02	7
7/7	120 ± 4	0.72 ± 0.05	4
8/8	125 ± 3	0.64 ± 0.03	5
7/8	80 ± 2	0.78 ± 0.03	7
6/7	80 ± 2	0.75 ± 0.01	5
6/8	46 ± 1	0.83 ± 0.02	3

Table 3.2. Parameters obtained by fitting the proton currents activation time constant as a function of voltage at different pHs. Activation time constants of proton currents at high voltages from the monomeric H_v1 were fitted to $ln[\tau(V)/ms] = -(z\delta_\alpha e_0/kT)V - ln(\alpha_0\ ms)$. N is the number of replicates of each condition. The function was defined in the text (equation 3.3). Values correspond to mean ± S.E.M.

pH_{in}/pH_{out}	α_0 (s^{-1})	$z\delta_\alpha$	N
6/6	14.1 ± 0.7	0.34 ± 0.01	7
7/7	35 ± 2	0.27 ± 0.01	4
8/8	9.1 ± 0.7	0.33 ± 0.01	5
7/8	59 ± 3	0.22 ± 0.01	7
6/7	80 ± 1	0.24 ± 0.01	5
6/8	95 ± 3	0.22 ± 0.01	3

3.4.2 H_v1 gating currents in a non-conducting mutant channel

The G-V curve shifts induced by a proton gradient indicate that pH affects the H_v1 closed-open equilibrium. However, the VSD activation and the channel opening are kinetically distinguishable processes in the monomer (Carmona et al., 2018), so the G-V curve shifts could be produced by affecting either of them. To study the pH dependence exclusively on the VSD activation, I have to measure gating currents produced during the VSD movements (Armstrong and Bezanilla, 1973; Bezanilla, 2018; Keynes and Rojas, 1973). Previously, I used the low-conducting mutant N264R to measure gating currents in the monomeric H_v1 channel (Carmona et al., 2018). Although ΔpH modulated gating currents of the N264R mutant, it was not possible to analyze these changes due to the presence of large proton currents at low internal pH (**Fig. 3.3**).

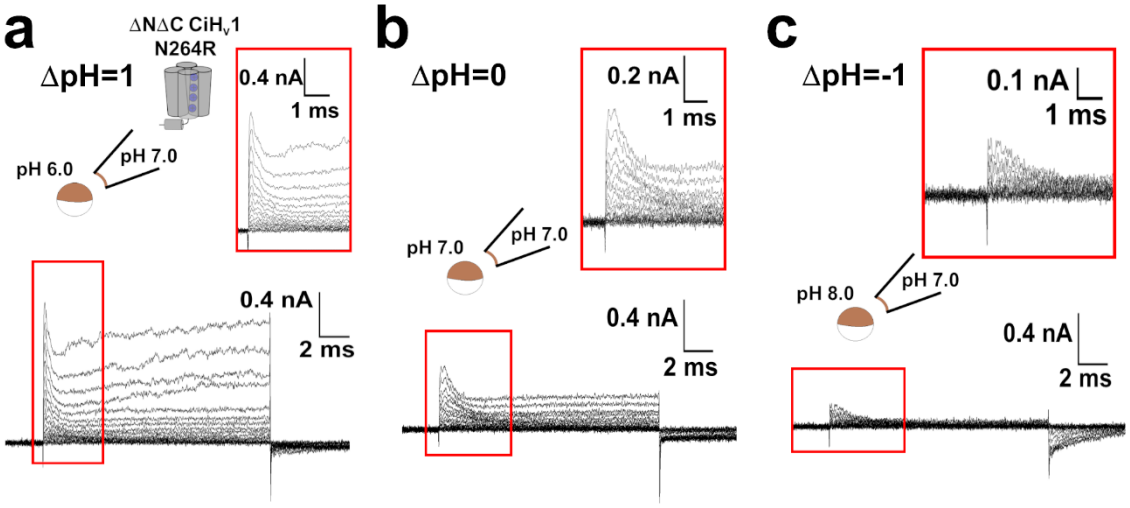

Figure 3.3. ΔpH modulated currents of the monomeric N264R H_v1 mutant. Currents produced by the monomeric N264R H_v1 mutant at (a) ΔpH=1 (pH_{in}/pH_{out}=6/7), (b) ΔpH=0 (pH_{in}/pH_{out}=7/7), and (c) ΔpH=-1 (pH_{in}/pH_{out}=8/7). Recordings are from the same patch of membrane. In (a) and (b), the protocol consisted of depolarizations from -90 to 250 mV from a holding potential of -70 mV. In (c), depolarizations from the holding potential were from -90 to 170 mV. A -P/8 subtraction protocol from a sub-holding potential of -90 mV was applied.

To eliminate proton currents, I searched for non-conducting H_v1 mutants. Previous reports show that mutations in one amino acid contained in the selectivity filter of the channel, D112 in hH_v1 and D160 in CiH_v1, resulted in non-conducting channels (Chamberlin et al., 2015; Mony et al., 2015; Musset et al., 2011). In particular, the absence of proton currents in the D160 mutants is not due to a defective VSD, as fluorescent-labeled mutant channels showed voltage-dependent fluorescence changes (Chamberlin et al., 2015; Mony et al., 2015). Fortunately, I found that the mutation D160N produced robust gating currents with almost a complete absence of ion currents in the monomeric H_v1 (**Fig. 3.4a**). However, a small current remains at the end of the depolarizing pulses during the ON-gating current, especially at high voltages (**Fig. 3.4a**, inset). I always observed this residual ion current in patches expressing the D160N channel, suggesting that this mutant still conserves a small conductance. However, its magnitude makes it difficult to determine the ion current origin and characteristics.

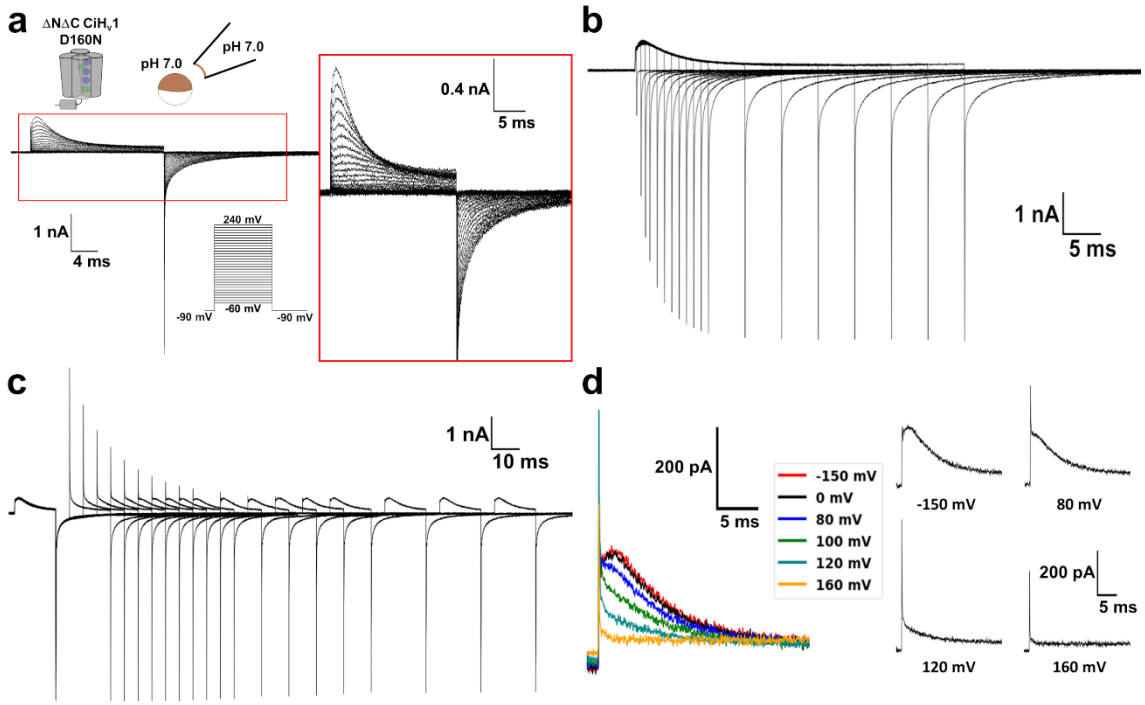

Figure 3.4. Gating currents of the monomeric D160N H_v1 mutant channel. Currents produced in patches of membranes expressing the monomeric D160N H_v1 mutant at symmetrical pH 7 are shown. A -P/8 subtraction protocol from a sub-holding potential of -90 mV was applied. (a) Superimposed traces of gating currents produced by depolarizations from a holding potential of -90 mV. Gating currents were elicited by voltages from -60 to 240 mV in 10 mV steps. (b) Superimposed traces of currents produced by a 200 mV depolarization pulse of increasing duration. Holding potential was -90 mV. (c) Superimposed traces of currents produced by an ON-recovery protocol consisting of two 200 mV depolarization pulses separated by returning to -90 mV at increasing duration. Holding potential was -90 mV. (d) Cole-Moore shift effect of gating currents produced by a 200 mV depolarization preceded by a prepulse at the indicated voltage.

As the mutation D160N significantly affects the channel opening, I wondered whether its VSD movements were similar to those studied previously in the low-conducting mutant N264R (Carmona et al., 2018). Similar to the N264R mutant gating currents, the D160N mutant showed a saturation of the OFF-gating current (**Fig. 3.4b**), a fast and a slow component during an ON-gating current recovery (**Fig. 3.4c**), and a Cole-Moore shift effect (**Fig. 3.4d**). However, I found that the presence of the residual ion current resulted in a higher gating charge displaced during the ON than during the OFF for large

depolarizing voltages when quantified by numerical integration. As this residual current is small, I fitted the ON-gating current decay, $I_g(t)$, to a single exponential

$$I_g(t) = I_0 e^{-t/\tau} \quad (3.4)$$

where I_0 is the current at time t=0 located after the ON-gating current rising phase and τ is the time constant. Due to the high voltage dependence of the decay kinetics, the interval of time I used for the fit was short for high voltages and increases as the applied voltage decreases (**Fig. 3.5a**). Residuals were used as the criterion to determine the interval of time needed for the fittings (**Fig. 3.5 and 3.6**). When the ON gating charge was calculated from the exponential fit and numerical integration of the rising phase, the charge displaced during the ON was equal to the OFF charge calculated by numerical integration of the OFF-gating current (**Fig. 3.6d**). More importantly, I could obtain the ON-gating current's kinetic information despite the presence of the ion residual current.

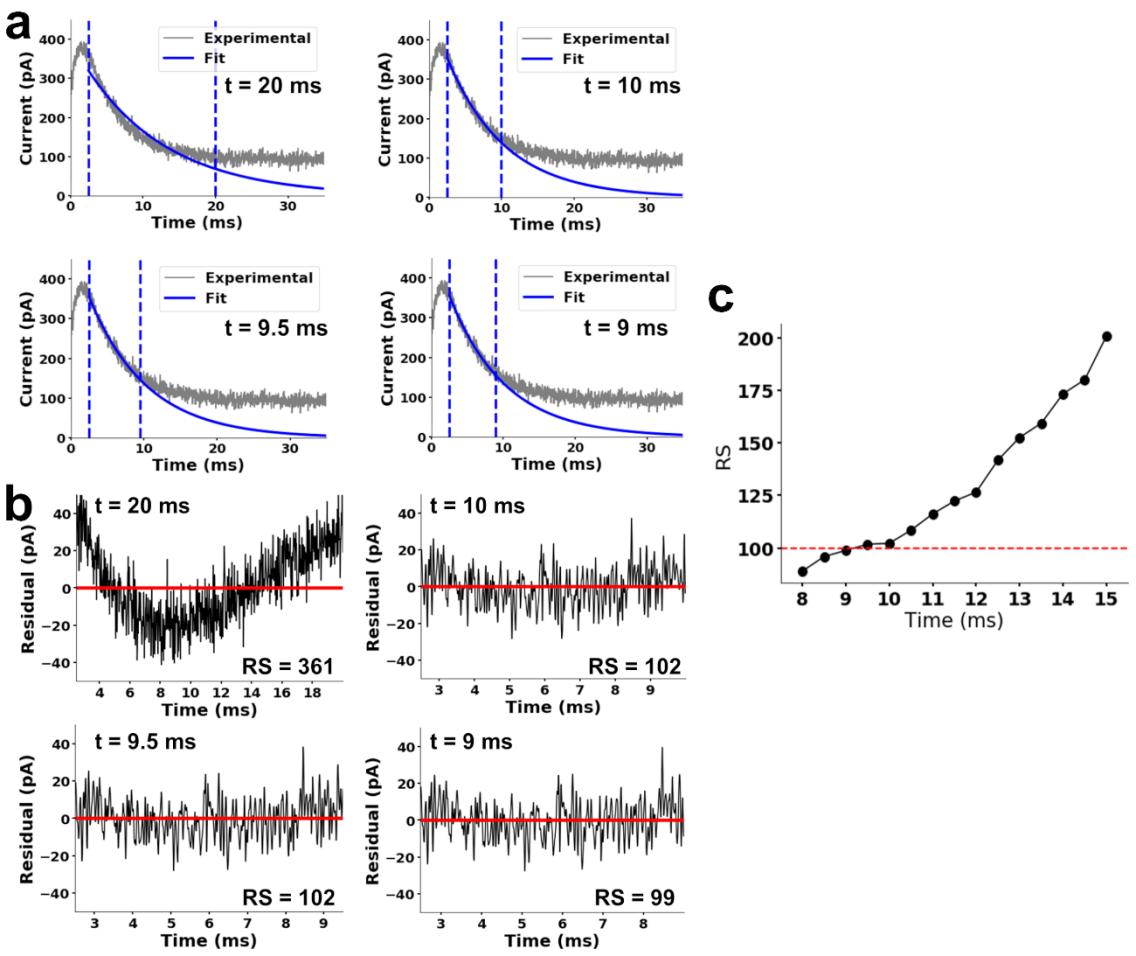

Figure 3.5. Residuals were used as the criterion to fit the decay of the ON-gating currents. Trace of ON-gating current of the monomeric D160N mutant H_v1 at 230 mV from a holding potential of -70 mV at symmetrical pH 7. A -P/8 subtraction protocol from a sub-holding potential of -90 mV was applied. (a) A representative procedure used to fit the experimental ON-gating current decay (grey trace) to a single exponential function (equation 3.4; red trace) is shown. The interval of time used for each fit is between the red dotted lines. Very long times (*t*=20 ms) produced a visible poor fit due to the residual current. As the interval of time decreased, the goodness of the fit increased. (b) Residuals of the fits during the respective interval of time showed in (a) were calculated as $r(t) = y(t) - \hat{y}(t)$, where r is the residual, y the experimental value, and $\hat{y}$ is the value obtained from the fit. Residuals were used to determine the goodness of the fit. For *t*=20 ms, there is an asymmetry in the distribution of the residuals. Although smaller, this asymmetry is still present at *t*=10 ms and 9.5 ms, indicating that the fit was poor in this part of the curve. I quantify the normalized sum of the residuals (*RS*) for each fit as

$$RS = \frac{\sum_{i=1}^{n} (y_i - \hat{y}_i)^2 / pA^2}{n}$$

where *n* is the number of points used in the fit. (c) The experimental trace was fitted using different intervals of time, and the *RS* for each fit was calculated. I used this plot to define an *RS* threshold (RS_T = 100 in this case, red dotted line). In this manner, I used the fit's

visual goodness, the distribution of the residuals, and the RS_T to decide the interval of time used to fit each trace of current (see Fig. 3.6). For the example showed in this figure, the best interval of time was 9 ms. An RS_T value of 100 was used for all the recordings at ΔpH=0, and a value of 120 was used for ΔpH>0.

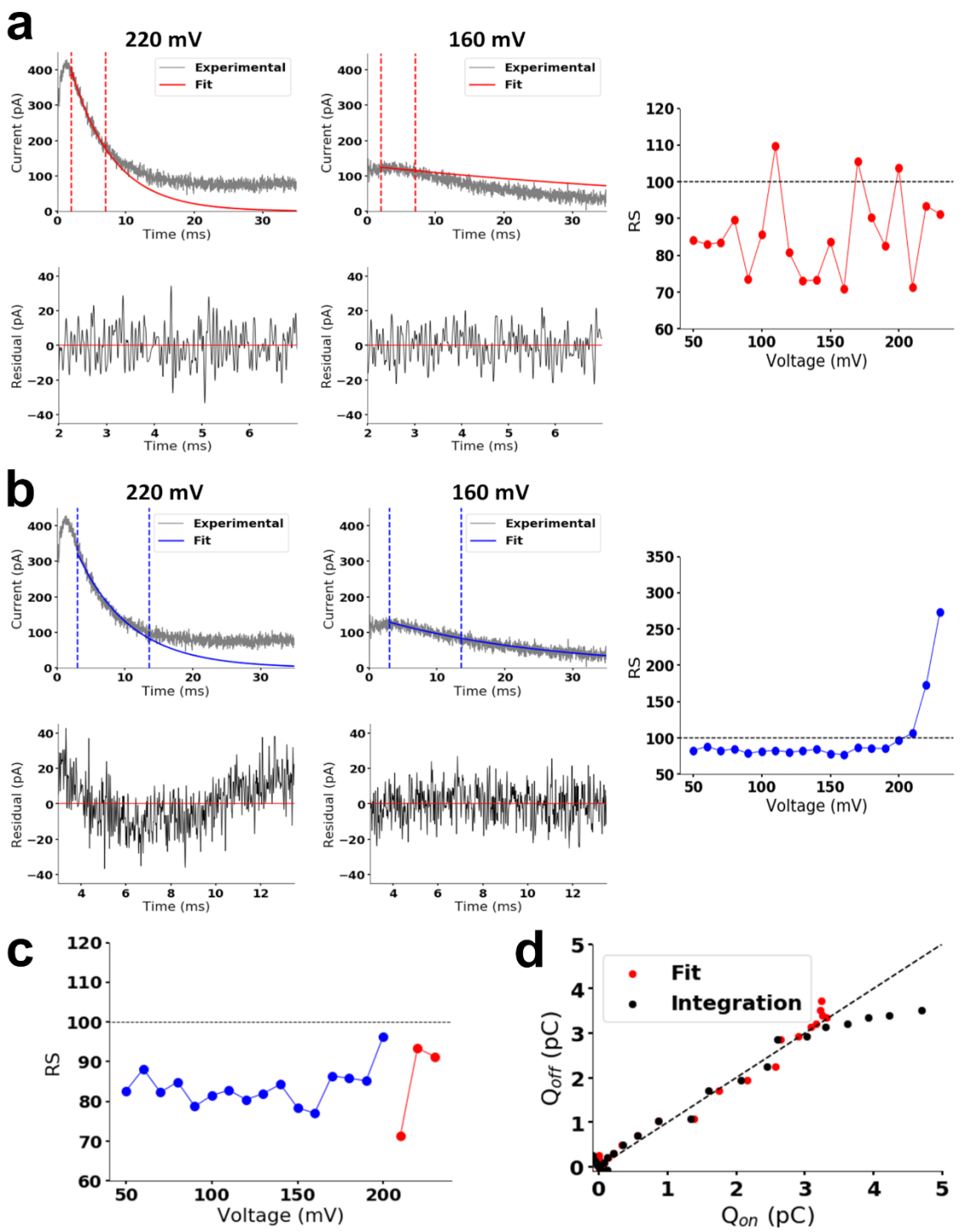

Figure 3.6. A representative fit procedure of the ON-gating currents for different voltages at ΔpH=0. Traces of ON-gating current of the monomeric D160N mutant H_v1 for different voltages at symmetrical pH 7 were fitted to obtain the kinetics of the ON-gating current decay. In this case, the analysis of a Q-V curve obtained from 50 to 230 mV is showed. Holding potential was -70 mV, and a -P/8 subtraction protocol from

a sub-holding potential of -70 mV was applied. Due to the high voltage-dependence of the kinetics of decay, the interval of time used to fit the entire Q-V changed depending on the applied voltage. (a) Short intervals of time to fit the data (red dotted lines, *t*=5 ms) produced good fits at high voltages (left), but poor fits at low voltages (center). The normalized sum of residuals (*RS*, defined in the legend of the Fig. 3.5) for each voltage is shown for this interval of time (right). The *RS* threshold (RS_T) used for the recordings at ∆pH=0 was 100 (black dotted line) and a value of 120 was used for ∆pH>0. In this case, neither the residuals distribution nor the sum of residuals indicated a poor fit at 160 mV. However, visual inspection of the fit is enough to decide this is not a suitable interval of time to fit the data for this voltage. (b) Long intervals of time (blue dotted lines, *t*=10.5 ms) produced poor fits at high voltages (left), but good fits at low voltages (center). *RS* for each voltage along with the RS_T (black dotted line) are shown for this interval of time (right). In this case, both the residuals distribution and the sum of residuals indicated a poor fit at 220 mV. (c) *RS* calculated for each voltage along with the RS_T (black dotted line). Red values were obtained using an interval of 5 ms to fit the data, while blue values were obtained using an interval of 10.5 ms to fit the data. (d) Charge displaced during the OFF-gating current (Q_{off}) was determined by numerical integration. In contrast, the charge displaced during the ON-gating current (Q_{on}) was determined by numerical integration (black circles) or by the area under the curve of the fit plus the numerical integration of the rising phase (red circles). The dotted line defines $Q_{off} = Q_{on}$. The Q_{on} was higher than the Q_{off} when the former was calculated by numerical integration (black circles). This difference is caused by the presence of the residual current at the end of the depolarizing pulses. However, Q_{on} was approximately equal to Q_{off} when the former was calculated from the exponential fits of the ON-gating currents (red circles).

3.4.3 The steady-state properties of H_v1 gating currents are ∆pH-dependent

I measured gating currents produced from the monomeric D160N H_v1 mutant at different internal and external pHs (**Fig. 3.7a-c**). Charge versus voltage (Q-V) curves were obtained from numerical integration of the OFF-gating currents for each condition (**Fig. 3.7d**) and fitted to a two-state Boltzmann distribution model

$$Q(V) = \frac{Q_{max}}{1+e^{\frac{-z\delta_Q F(V-V_{0.5})}{RT}}} \tag{3.5}$$

where Q_{max} is the maximal charge displaced, $z\delta_Q$ is the effective valence, and the rest of the parameters were defined in equation 3.1. Q-V curves obtained in symmetrical pH superimposed, but they shifted to the left as the ∆pH increased (**Fig. 3.7d**) following the pattern showed by the G-V curves (cf. **Fig. 3.1d** with **Fig. 3.7d**).

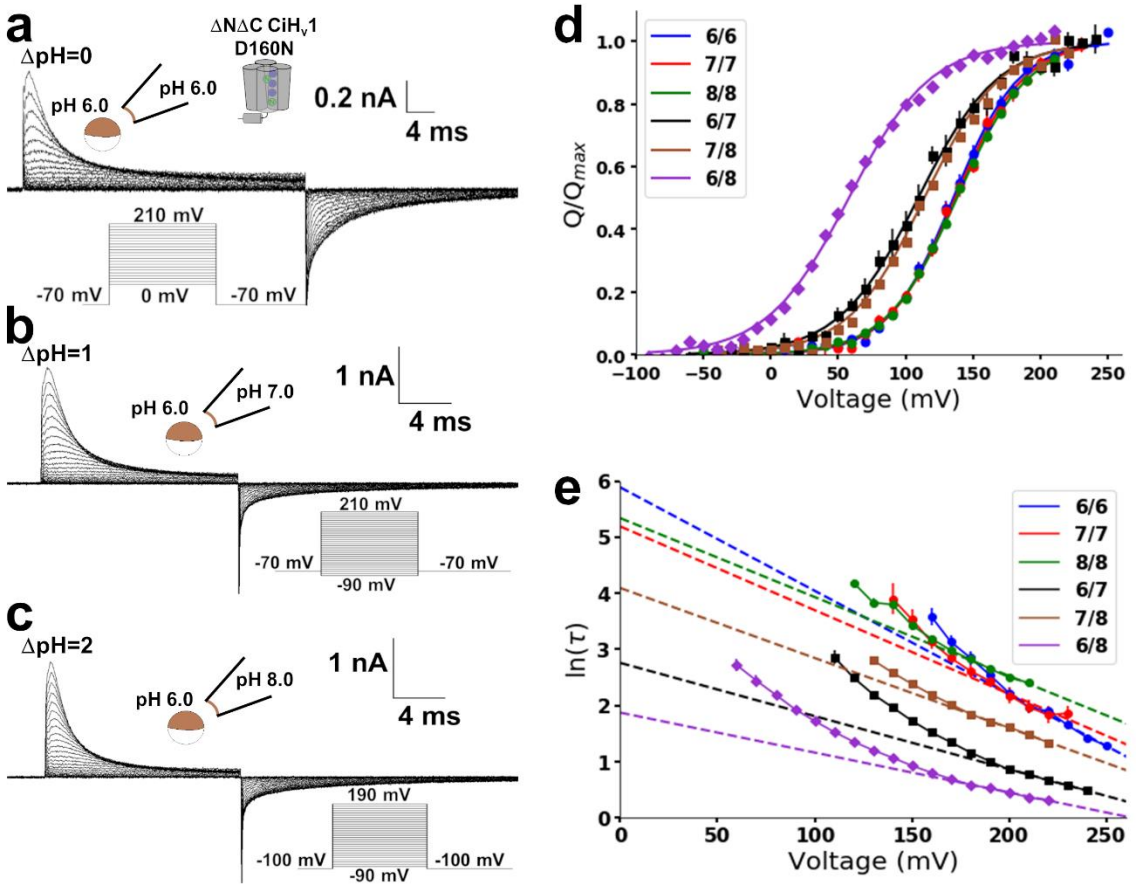

Figure 3.7. Gating currents of monomeric D160N H_v1 mutant are ΔpH-dependent. Currents produced in patches of membranes expressing the monomeric D160N H_v1 mutant at different pHs were measured. A -P/8 subtraction protocol from a sub-holding potential of -90 mV was applied. Representative recordings at (a) ΔpH=0, (b) ΔpH=1, and (c) ΔpH=2 are shown. (d) Mean Q-V curves at the indicated pH_{in}/pH_{out}. Curves were fitted using a two-state Boltzmann distribution model (lines; equation 3.5 and Table 3.3). (e) The mean logarithm of the ON-gating current decay time constant as a function of voltage at the indicated pH_{in}/pH_{out}. Dotted lines correspond to the fit of data at high voltages to the equation $ln[\tau(V)/ms] = -(z\delta_\alpha e_0/kT)V - ln(\alpha_0\ ms)$ (equation 3.3 and Table 3.4). Data are shown as mean ± S.E.M.

The Q-V shifts indicate that the ΔpH alters the resting-active (R-A) equilibrium of the VSD.

This ΔpH-dependent change can be quantified as the $V_{0.5}$ shift relative to symmetrical pH:

$$\Delta V_{0.5} = V_{0.5(\Delta pH)} - V_{0.5(\Delta pH=0)} \tag{3.6}$$

The $\Delta V_{0.5}$ obtained when the ΔpH=2 was -77 ± 7 mV (**Table 3.3**). Such a shift causes a decrease in the free energy that defines the VSD R-A equilibrium of 9.0 ± 0.8 kJ/mole. This calculation makes the simplifying assumption that a two-state R-A model describes the VSD displacement. Despite this, it is useful to illustrate the significant difference of free energy in the VSD R-A equilibrium produced by the ΔpH change. Therefore, somehow the energy stored in the ΔpH is coupled to the H_v1 VSD activation.

Table 3.3. Parameters from the Q-V curves fitted to a two-state Boltzmann distribution model at different pHs. Q-V curves of the monomeric D160N H_v1 mutant were fitted to $Q(V) = Q_{max}/(1 + exp(-z\delta_Q F(V - V_{0.5})/RT))$. N is the number of replicates of each condition. The function was defined in the text (equation 3.5). Values correspond to mean ± S.E.M.

pH_{in}/pH_{out}	$V_{0.5}$ (mV)	$z\delta_Q$	N
6/6	135 ± 2	1.05 ± 0.03	7
7/7	137 ± 3	1.01 ± 0.03	4
8/8	138 ± 1	0.98 ± 0.03	5
7/8	116 ± 1	0.90 ± 0.02	6
6/7	112 ± 3	0.87 ± 0.04	4
6/8	58 ± 2	0.85 ± 0.01	8

Next, I fitted the ON-gating current decay using the strategy discussed above for all the different pHs (**Fig. 3.5 and 3.6**). The ON-gating currents decay kinetics were similar in symmetrical pH and differed in the presence of a positive ΔpH (**Fig. 3.7e**). This result was analogous to that of the proton currents activation kinetics in the conductive channel (cf. **Fig. 3.1e** with **Fig. 3.7e**). The ON-gating current decay time constants ($\tau(V)$) for high voltages were fitted using equation 3.3 (**Table 3.4**). The parameter values can be separated into two groups corresponding to ΔpH=0 (low α_0 values and high $z\delta_\alpha$ values) and ΔpH>0 (high α_0 values and low $z\delta_\alpha$ values). However, this last group's values differed,

following the order 6/8 > 6/7 > 7/8 (pH_{in}/pH_{out}) for the values of α_0 and the inverse order for the $z\delta_\alpha$ values. Despite this, an increase of ΔpH in two units increased the value of α_0 50 times and decreased $z\delta_\alpha$ by 62%. This significant change shows that a positive ΔpH value increased the VSD activation's slowest forward rate. However, the degree of increase depends on the internal and external pH instead of ΔpH.

Table 3.4. Parameters obtained by fitting the ON-gating current decay time constant as a function of voltage at different pHs. ON-gating currents time constants of decay at high voltages from the monomeric D160N H_v1 mutant were fitted to $ln[\tau(V)/ms] = -(z\delta_\alpha e_0/kT)V - ln(\alpha_0\ ms)$. N is the number of replicates of each condition. The function was defined in the text (equation 3.3). Values correspond to mean ± S.E.M.

pH_{in}/pH_{out}	α_0 (s^{-1})	$z\delta_\alpha$	N
6/6	3 ± 1	0.47 ± 0.04	7
7/7	6 ± 4	0.38 ± 0.08	4
8/8	3.4 ± 0.5	0.40 ± 0.02	5
7/8	17 ± 1	0.32 ± 0.01	6
6/7	63 ± 5	0.24 ± 0.01	4
6/8	150 ± 10	0.18 ± 0.01	8

3.4.4 H_v1 gating currents kinetics depends on the internal and external pH values

The previous experiments suggest that a positive ΔpH value modifies the steady-state R-A occupancies of the H_v1 VSD and increases the slowest forward activation rate. However, the monomeric VSD undergoes several transitions during activation (**Fig. 3.4**). Therefore, gating currents kinetics will help to clarify the pH dependence mechanism of the VSD movements. I first used a voltage protocol consisting of 200-mV depolarizations of increasing duration from a holding potential of -90 mV (**Fig. 3.8**). In this manner, the VSD deactivates from states that are increasingly distant from the initial resting state (S_0). The OFF-gating current decay had fast and slow components in a proportion that

changed according to the depolarizing pulse duration, resulting in a slower decay at more prolonged pulses (**Fig. 3.8a-c and 3.9**). Moreover, the proportion and rate of these components changed according to the internal and external pH values, which was evident even in the OFF-gating current amplitude at ΔpH=1 (**Fig. 3.8b-c**).

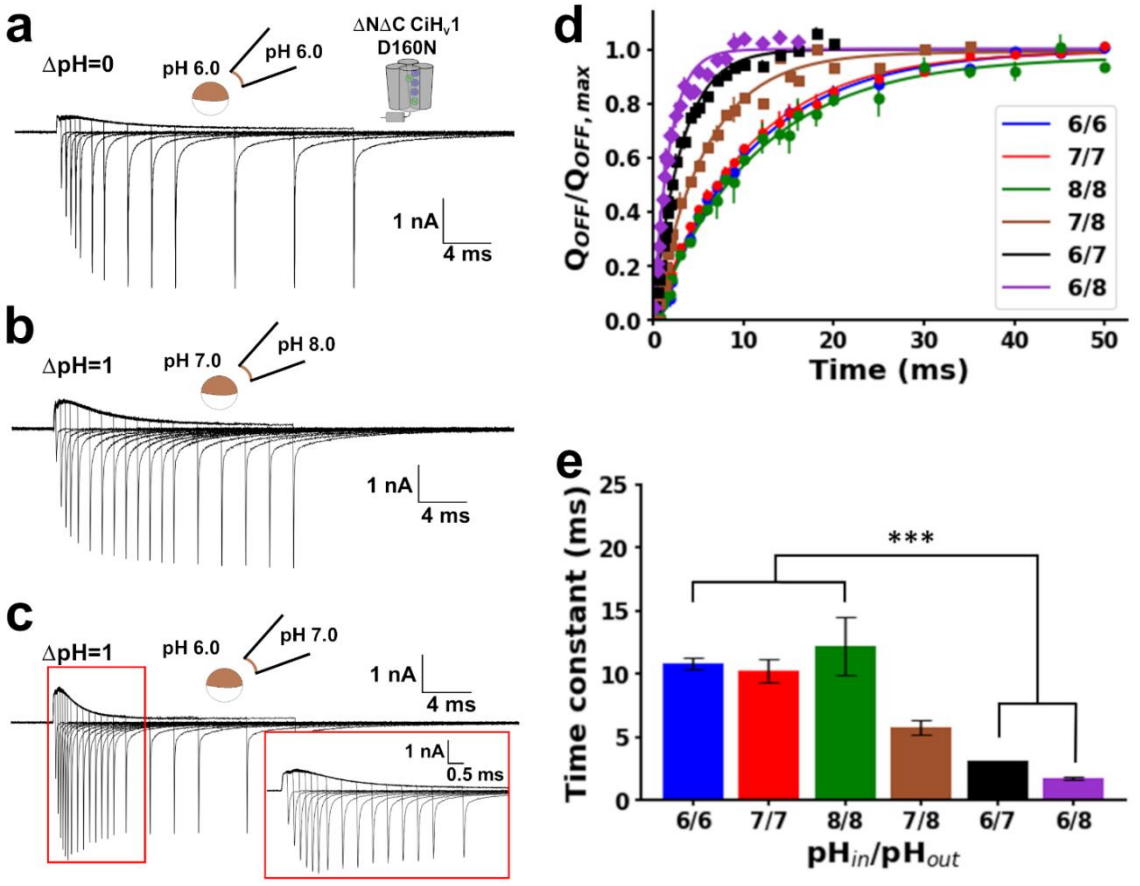

Figure 3.8. The activation kinetics of the monomeric D160N H_v1 mutant increased with ΔpH. Currents produced in patches of membranes expressing the monomeric D160N H_v1 mutant at different pHs were measured. The protocols consisted of short 200 mV depolarizations of increasing duration. Holding potential was -90 mV, and a -P/8 subtraction protocol from a sub-holding potential of -90 mV was applied. The figure shows representative recordings at (a) ΔpH=0, and two different internal and external pH values corresponding to ΔpH=1, (b) pH_{in}/pH_{out}=7/8 and (c) pH_{in}/pH_{out}=6/7. (d) Mean normalized OFF-gating charge ($Q_{OFF}/Q_{OFF,max}$) as a function of the depolarization duration at different pHs. Data were fitted to the equation $Q_{OFF}/Q_{OFF,max}(t) = 1 - exp(-t/\tau)$ (lines; equation 3.7). (e) Time constant values at the indicated pH_{in}/pH_{out} (Table 3.5). Statistical analysis was performed by a one-way ANOVA post-Tukey test (***:P≤0.001). Data are shown as mean ± S.E.M.

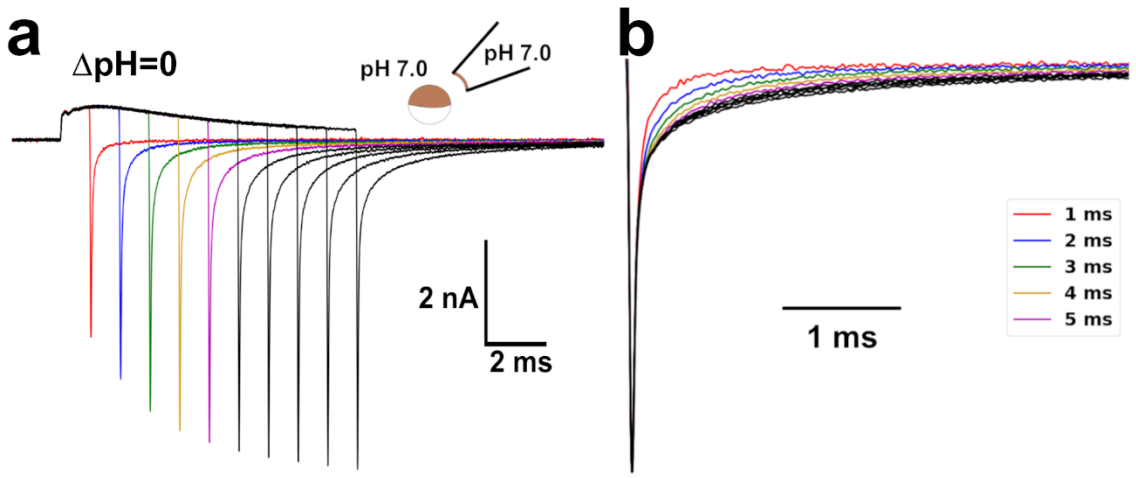

Figure 3.9. The OFF-gating currents decay of the monomeric D160N H_v1 mutant was slower at more prolonged depolarizations. Representative current traces produced by the monomeric D160N H_v1 mutant. Although the figure shows an experiment in symmetrical pH 7, the same phenomenon occurred at all the different pHs tested (see Fig. 3.8). Holding potential was -90 mV, and -P/8 subtraction protocol from a sub-holding potential of -90 mV was applied. (a) Superimposed traces of currents produced by a 200-mV depolarization pulse of increasing duration. (b) Normalized OFF-gating currents showed in (a). The colored traces correspond to the currents produced at the indicated depolarization durations in the legend.

These results indicate the existence of multiple pH-dependent transitions separating S_0 and the final state (S_n) during the VSD activation. Despite this complexity, the charge displaced during the OFF as a function of the depolarization duration, $Q_{OFF}(t)$, increased until reaching saturation (**Fig. 3.8d**). The $Q_{OFF}(t)$ data fitted well to a single exponential

$$Q_{OFF}(t) = Q_{OFF,max}(1 - e^{-t/\tau}) \quad (3.7)$$

where $Q_{OFF,max}$ is the charge displaced at infinite time and τ is the time constant (**Table 3.5**). The fitting of the $Q_{OFF}(t)$ data using equation 3.7 showed that a positive ΔpH increased the VSD activation (**Fig. 3.8e**). This time constant value was similar to that obtained when measuring the ON-gating current decay at the same voltage by equation 3.4 (**Fig. 3.7e**; both values showed in **Table 3.5**). These results showed that the VSD

activation involves several transitions, but the slowest transition displaces most of the gating charge. Furthermore, although the ΔpH-dependent shifts of the Q-V curves were independent of the internal and external pH, gating currents kinetics depended on these pH values.

Table 3.5. Activation time constants of the H_v1 voltage sensor at different pHs. Time constants (τ) were obtained from fits of the experiments shown in Fig. 3.8 to the equation $Q_{OFF}/Q_{OFF,max}(t) = 1 - exp(-t/\tau)$. N is the number of replicates of each condition. The function was defined in the text (equation 3.7). For comparison, the time constant obtained from the ON-gating current decay at 200 mV plotted in Fig. 3.7e (τ_{QV200}), along with its number of replicates (N_{QV200}), is included. Values correspond to mean ± S.E.M.

pH_{in}/pH_{out}	τ (ms)	N	τ_{QV200} (ms)	N_{QV200}
6/6	11 ± 1	4	9.5 ± 0.8	7
7/7	10 ± 2	5	9 ± 1	4
8/8	12 ± 4	3	12.1 ± 0.2	5
7/8	6 ± 1	3	5.0 ± 0.1	6
6/7	3.1 ± 0.4	12	2.4 ± 0.1	4
6/8	1.8 ± 0.4	9	1.59 ± 0.09	8

Next, I studied the VSD deactivation by an ON-recovery protocol consisting of two 200-mV depolarization pulses separated by an increasing interval of time at -90 mV (**Fig. 3.10**). The VSD is completely activated with the first depolarizing pulse, but the subsequent deactivation at -90 mV is interrupted by the second depolarization. Therefore, the second ON-gating current is produced by the VSD activation from states that are increasingly distant from S_n. Gating currents elicited by the second voltage pulse showed two components (**Fig. 3.10a-c**). A faster current component appeared when the separation between depolarizations was short. As this separation increased, the faster component decreased, and the slower component began to recover. The charge displaced during the second depolarization normalized by the first depolarization, $Q_{ON2}/Q_{ON1}(t)$, was fitted using a two-component exponential function (**Fig. 3.10d**):

$$Q_{ON2}/Q_{ON1}(t) = Q_{fast}\left(1 - e^{-t/\tau_{fast}}\right) + Q_{slow}\left(1 - e^{-t/\tau_{slow}}\right) \quad (3.8)$$

with Q_{fast} and Q_{slow} being the proportions of the fast and slow gating charge components, respectively, and τ_{fast} and τ_{slow} their respective time constants (**Table 3.6**). The fast time constant was pH-independent (around 2 ms), while the slow time constant was affected by pH (**Fig. 3.10e**). At ΔpH=0, there was a trend for the slow time constants to increase at low pH values, but these differences were not statistically significant. Moreover, the τ_{slow} value did not change appreciably between pH_{in}/pH_{out} 7/7 and 7/8, even though the ΔpH value changed. On the other hand, this time constant increased significantly when pH_{in}/pH_{out} was 6/7 and 6/8 (corresponding to a ΔpH value of 1 and 2, respectively). However, the values between these last ΔpHs were not significantly different. Thus, although the data suggest that a positive ΔpH decreases the deactivation rate when I compare the values at ΔpH=0 with pH_{in}/pH_{out} 6/7 and 6/8, this is not a general conclusion.

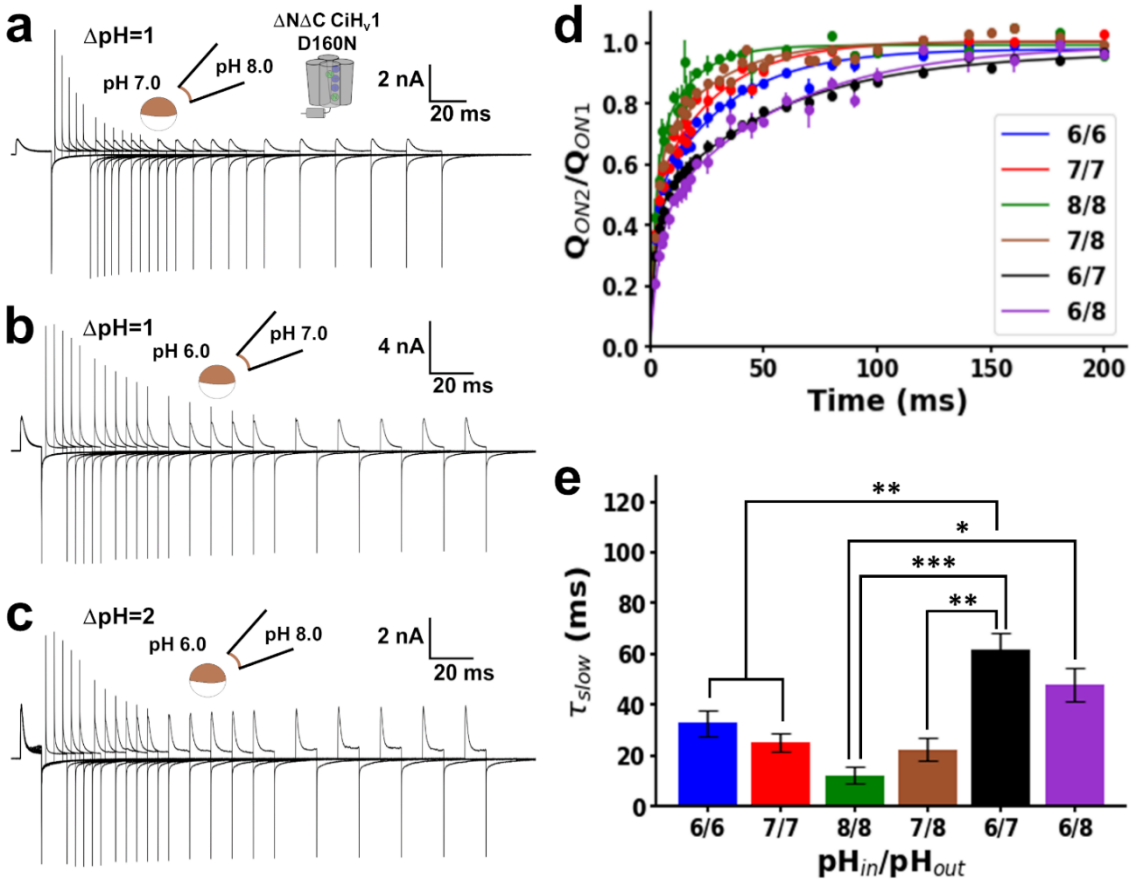

Figure 3.10. The ON-recovery kinetics of the monomeric D160N H_v1 was not ΔpH-dependent. Currents produced in patches of membranes expressing the monomeric D160N H_v1 mutant at different pHs were measured. The protocols consisted of two depolarizations at 200 mV separated by a return of increasing duration at -90 mV. Holding potential was -90 mV, and a -P/8 subtraction protocol from a sub-holding potential of -90 mV was applied. The figure shows representative recordings at different values of internal and external pH corresponding to ΔpH=1, (a) pH_{in}/pH_{out}=7/8 and (b) pH_{in}/pH_{out}=6/7, and (c) ΔpH=2. (d) Mean charge displaced during the second depolarization (Q_{ON2}) normalized by the first depolarization (Q_{ON1}) as a function of the interval between the depolarizing pulses at different pHs. Data were fitted to the equation $Q_{ON2}/Q_{ON1}(t) = Q_{fast}(1-exp(-t/\tau_{fast})) + Q_{slow}(1-exp(-t/\tau_{slow}))$ (equation 8). (e) Time constants of the slower component at the indicated pH_{in}/pH_{out} (Table S6). Statistical analysis was performed by a one-way ANOVA post-Tukey test (*:P≤0.05, **:P≤0.01, and ***:P≤0.001). Data are shown as mean ± S.E.M.

Table 3.6. Time constants obtained from the ON-gating current recovery protocol at different pHs. Time constants obtained from fits of the experiments shown in Fig. 3.10 to the equation $Q_{ON2}/Q_{ON1}(t) = Q_{fast}(1-exp(-t/\tau_{fast})) + Q_{slow}(1-exp(-t/\tau_{slow}))$. N is the number of replicates of each condition. The function was defined in the text (equation 3.8). Values correspond to mean ± S.E.M.

pH_{in}/pH_{out}	τ_{fast} (ms)	τ_{slow} (ms)	N
6/6	1.7 ± 0.2	33 ± 5	6
7/7	1.8 ± 0.1	25 ± 4	4
8/8	1.9 ± 0.6	12 ± 3	3
7/8	2.2 ± 0.3	23 ± 5	3
6/7	2.6 ± 0.2	62 ± 6	8
6/8	3.9 ± 0.4	48 ± 7	3

To clarify the effect of pH on the VSD deactivation, I also analyzed the OFF-gating current decay. Since the charge is obtained from the integral of the current over time, the slow time constants obtained from the ON-recovery and OFF-gating current decay should have similar values. However, the last recordings suggest they are different since ON-gating current recovery did not coincide visually with the OFF-gating current decay (**Fig. 3.10b-c**). To compare both kinetics, I fitted the OFF-gating current at -90 mV from 0.4 ms onwards, $I_{OFF}(t)$, to a two-component exponential function (**Fig. 3.11**)

$$I_{OFF}(t) = I_{0,fast}e^{-t/\tau_{fast}} + I_{0,slow}e^{-t/\tau_{slow}} \quad (3.9)$$

where $I_{0,fast}$ and $I_{0,slow}$ are the initial current amplitudes of the fast and slow component, respectively, and τ_{fast} and τ_{slow} are their respective time constants (**Table 3.7**). The difference of the slow deactivation kinetics calculated from the ON-recovery (equation 3.8) and the OFF decay (equation 3.9) depended on the internal and external pH (**Fig. 3.11a-b**; both values showed in **Table 3.7**). The slow OFF-gating current decay time constant was higher when pH_{in} was 6, independent of the ΔpH value (**Fig. 3.11c**). Moreover, they were consistently smaller than the ON-recovery slow time constant,

except at symmetrical pH 8 (**Table 3.7**). These results suggest that the VSD deactivation kinetics measured by these two approaches are produced by different transitions (see Discussion). Despite this, the kinetic analysis of gating currents demonstrated that H_v1 VSD activation and deactivation depend on the internal and external pH instead of the ΔpH value.

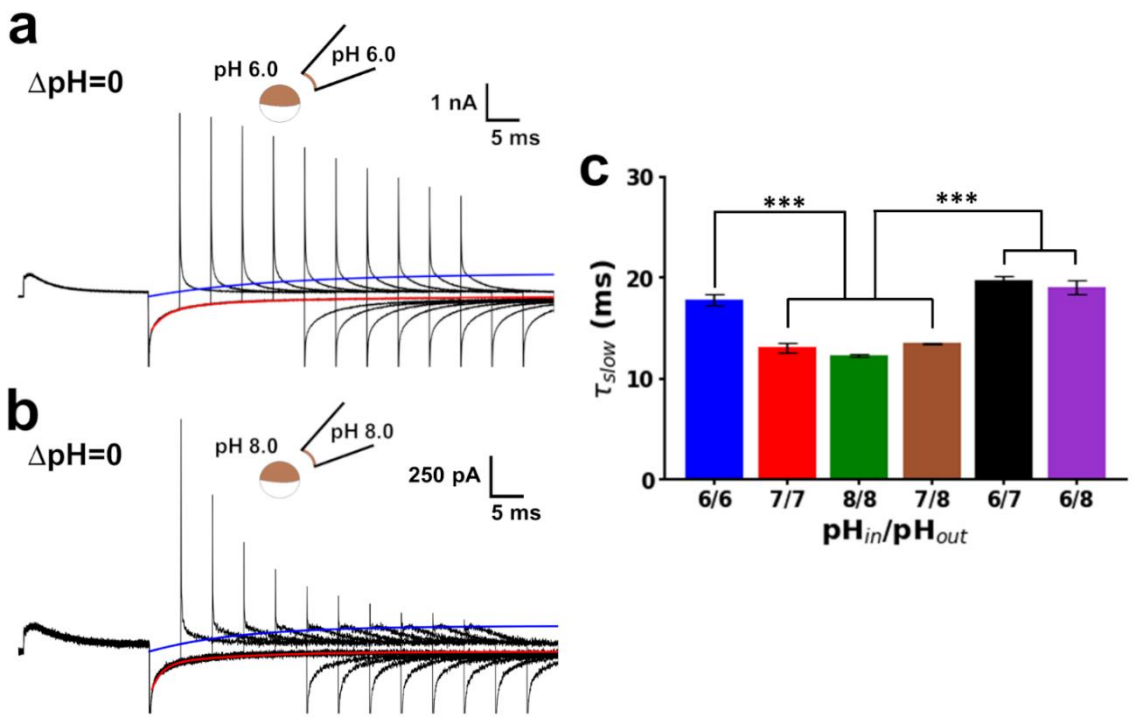

Figure 3.11. The OFF-gating current decay and the ON-gating current recovery showed different kinetics for the monomeric D160N H_v1 mutant. Representative currents produced by the monomeric D160N H_v1 mutant during the ON-recovery protocol at (a) symmetrical pH 6 and (b) symmetrical pH 8 are shown. The protocol consists of two 200 mV depolarizations separated by an increasing interval of time at -90 mV. Holding potential was -90 mV, and -P/8 subtraction protocol from a sub-holding potential of -90 mV was applied. OFF-gating current (I_{OFF}) was fitted to the equation $I_{OFF}(t) = I_{0,fast}exp(-t/\tau_{fast}) + I_{0,slow}exp(-t/\tau_{slow})$ (equation 3.9). The fits are shown as a red line. To compare it with the ON-gating recovery, the fit's slower component with a final amplitude corresponding to the first ON-gating current maximum is shown in blue. (c) Slower OFF-gating current decay time constants at -90 mV at different pHs (Table 3.7). Statistical analysis was performed by a one-way ANOVA post-Tukey test (***:P≤0.001). Data are shown as mean ± S.E.M.

Table 3.7. OFF-gating current decay time constants at -90 mV at different pHs. Time constants (τ) were obtained from fits of the OFF-gating current at -90 mV to the equation $I_{OFF}(t) = I_{0,fast}exp(-t/\tau_{fast}) + I_{0,slow}exp(-t/\tau_{slow})$. N is the number of replicates of each condition (Fig. 3.11c). The function was defined in the text (equation 3.9). For comparison, the slow time constant obtained from the ON-recovery protocol plotted in Fig. 3.10e ($\tau_{slow,ONRec}$), along with its number of replicates (N_{ONRec}), is included. Values correspond to mean ± S.E.M.

pH_{in}/pH_{out}	τ_{fast} (ms)	τ_{slow} (ms)	N	$\tau_{slow,ONRec}$ (ms)	N_{ONRec}
6/6	2.07 ± 0.07	17.9 ± 0.5	6	33 ± 5	6
7/7	1.72 ± 0.04	13.1 ± 0.5	4	25 ± 4	4
8/8	1.9 ± 0.1	12.3 ± 0.1	5	12 ± 3	3
7/8	2.3 ± 0.2	13.5 ± 0.1	4	23 ± 5	3
6/7	1.95 ± 0.06	19.8 ± 0.5	8	62 ± 6	8
6/8	2.5 ± 0.3	19.1 ± 0.7	7	48 ± 7	3

3.5 Discussion

3.5.1 The pH modifies the voltage dependence of H_v1

My results showed that the monomeric H_v1 contains the molecular determinant(s) necessary to sense the internal and external pH. In particular, the H_v1 VSD movements are changed by pH. This pH dependence has been studied previously using the dimeric W207A-N264R hH_v1 mutant (De La Rosa and Ramsey, 2018). Similar to my results, an increase of pH_{out} (higher ΔpH) produced a leftward shift of the Q-V curve and faster ON-gating currents decay (De La Rosa and Ramsey, 2018). However, this study only explored the effect of one change in pH_{out}, leaving the unknown of the ΔpH effect on H_v1 gating currents. Additionally, the mutation W207A, which is necessary to measure hH_v1 gating currents, modifies the channel's external pH dependency (Cherny et al., 2015). I solved both issues using the monomeric D160N mutant, demonstrating for the first time that the H_v1 VSD steady-state properties are ΔpH-dependent. However, VSD kinetics depend on internal and external pH values.

The Q-V curve shifts of the monomeric D160N mutant can be explained by a decrease in the energy difference between S_0 and S_n (ΔG) at higher ΔpH values. This conclusion is model-independent since it was obtained in equilibrium. However, a better understanding of the pH dependence mechanism requires knowing how pH modulates the H_v1 VSD transitions. Two different approaches showed that the slowest forward rate increased at higher ΔpH values. First, the fitting of the ON-gating currents decay $\tau(V)$ data at high voltages (**Fig. 3.7e**); and second, the $Q_{OFF}(t)$ data obtained from depolarizing pulses of increasing duration (**Fig. 3.8d**). More importantly, this last experiment indicates that most of the gating charge is displaced in a single transition. Therefore, the states of the VSD, S_i, can be assigned to two groups separated by a high energy barrier (**Fig. 3.12a**, black). Based on my previous model (Carmona et al., 2018), I can propose the number of states separated by the highest energy barrier shown in **Fig. 3.12a**, but the following reasoning is valid for a model of any number of states. The forward rate of activation at high voltages will be determined mainly by the energy difference between S_0 and the maximum of the highest energy barrier (ΔG^*) (**Fig. 3.12a**). My results indicate that a positive ΔpH decreases both ΔG and ΔG^*. The simplest way to decrease both energies is destabilizing the states preceding the highest energy barrier (**Fig. 3.12a**, red). Only a destabilization of S_0 can produce the same outcome if a new higher energy state is occupied at the resting conditions (e.g., the third energy well in **Fig. 3.12a**). In agreement with this model, molecular dynamics simulations have also proposed a destabilization of the H_v1 resting state in the presence of a positive ΔpH by disrupting intramolecular electrostatic interactions (Boonamnaj and Sompornpisut, 2019). However, this model cannot explain the differences in kinetics I found at ΔpH=1 or during deactivation. A state-dependent pH

dependency can explain this discrepancy, so each energy barrier is modulated by the internal and external pH independently.

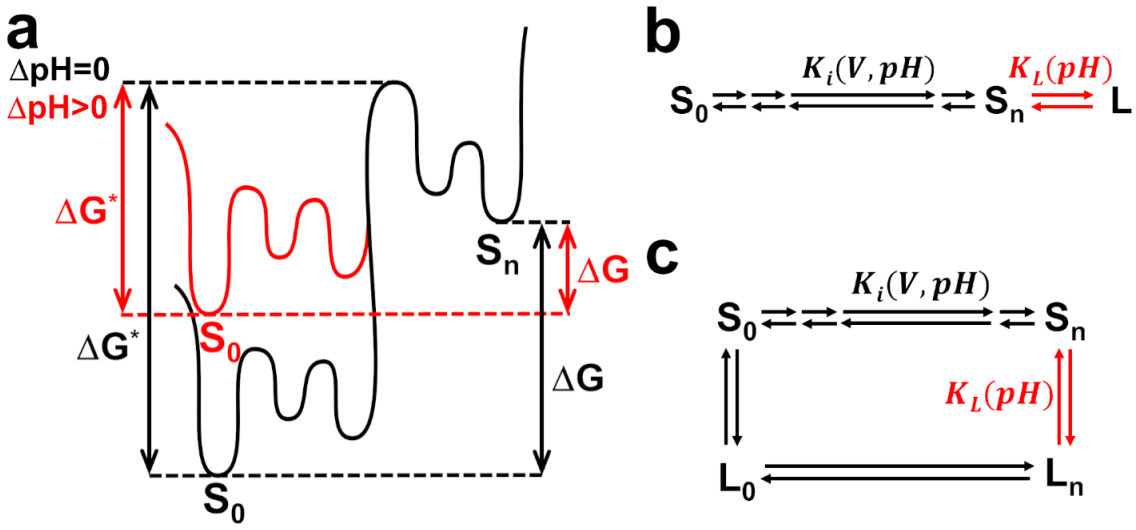

Figure 3.12. Proposed models to explain the pH dependency of the monomeric D160N H_v1 voltage sensor. (a) Simplified proposed energy profiles for the monomeric H_v1 VSD activation that explain its ΔpH dependency. In black, the profile and free energies in the absence of a ΔpH are shown. The energy difference between the VSD initial state (S_0) and final state (S_n) and between S_0 and the maximum of the highest activation energy barrier, are indicated as ΔG and ΔG*, respectively. The simplest change in the energy profile that explains the experimental results when ΔpH increases is shown in red. (b) Proposal for a sequential kinetic model that explains the H_v1 VSD deactivation. (c) Proposal for a non-sequential kinetic model that explains the H_v1 VSD deactivation. K_i represents the voltage- and pH-dependent equilibrium constants of the ith step (black). K_L is the voltage-independent equilibrium constant of the step from S_n to the relaxed state L or L_n (red).

3.5.2 H_v1 voltage sensor deactivation reveals a voltage-independent transition

Deactivation measured by the ON-recovery (**Fig. 3.10**) evidenced a slower rate at higher ΔpH, which is explained by an increase in the energy difference between S_n and the highest energy barrier (**Fig. 3.12a**). The stabilization of the S_n state would decrease this energy and ΔG. However, deactivation is not a simple function of pH or ΔpH. The pH modulation of the ON-recovery deactivation kinetics could be explained by the saturation

of the changes produced at alkaline pH (Berger et al., 2017; Cherny et al., 1995; Cherny et al., 2015), as the slow ON-recovery kinetics did not appreciably vary when pH was changed from 7 to 8. However, such saturation was not observed in the monomeric channel G-V or Q-V curve shifts. More importantly, the deactivation measured by the OFF-gating current decay (**Fig. 3.11**) showed a completely different result. The difference between the time constants of deactivation is not an artifact since it was evidenced even in the same experiment. The simplest way to explain this discrepancy is that the H_v1 VSD activation involves a sequential model with a voltage-independent step from S_n to a relaxed state (L) (**Fig. 3.12b**). Since only the voltage-dependent steps produce gating currents, the last transition is not observed in the OFF-gating current decay. However, the ON-recovery can reveal this slow voltage-independent transition.

Interestingly, a low voltage-dependent transition related to channel opening has been proposed for the H_v1 dimer (Gonzalez et al., 2010; Qiu et al., 2013; Villalba-Galea, 2014). Moreover, the D160N mutation slows down the fluorescence signal associated with the opening of dimeric channels labeled in S1 (Mony et al., 2015). My results show that a similar slow transition is also present in the monomeric D160N VSD, suggesting that L is related to the open channel conformation. As proposed previously for the dimer (Mony et al., 2015; Qiu et al., 2013), my data suggest that a voltage-independent conformational change opens the channel after VSD activation. Surprisingly, ON-recovery kinetics showed that this last step is pH-dependent (**Fig. 3.10e**), so pH modulates both the VSD activation and the permeation pathway opening independently. It is important to mention that a model involving an alternative deactivation pathway through relaxed states (L_i) can also explain my data (**Fig. 3.12c**). This last model has been proposed to occur in the VSD to explain hysteresis in voltage-gated ion channels (Bezanilla et al., 1982; Bruening-Wright and Larsson, 2007; Villalba-Galea et al., 2008), including H_v1 (Villalba-Galea,

2014). However, the simpler sequential model is preferred as it can explain my data using fewer parameters.

3.5.3 The D160 is more than a selectivity filter in H_v1

The existence of a voltage-independent transition related to channel opening in the non-conducting D160N mutant is surprising. This conserved aspartate located in S1 has been proposed to be the channel's selectivity filter (Berger and Isacoff, 2011; Musset et al., 2011) because mutations in this residue produced an impaired selectivity (Berger and Isacoff, 2011; Musset et al., 2011) or non-conducting channels (Berger and Isacoff, 2011; Chamberlin et al., 2015; Mony et al., 2015; Musset et al., 2011; Qiu et al., 2016). Despite this, these mutant channels are still functional in both their voltage (Chamberlin et al., 2015; Mony et al., 2015; Qiu et al., 2016) and pH dependence (Musset et al., 2011; Ramsey et al., 2010). Searching for a channel with these characteristics to study the pH dependence of H_v1 gating currents, I introduced mutations in the position D160 of the monomeric CiH_v1 and measured the gating currents produced by them. I found that mutants D160C, D160A, D160Q, and D160N produced gating currents with only a small contribution of ion currents (**Fig. 3.13**). Mutants D160C and D160A produced small gating currents with slow kinetics and Q-V curves that saturate at high voltages, making them unsuitable for my goal. On the contrary, mutants D160Q and D160N showed larger gating currents with faster kinetics. Despite this, all D160 mutants showed pH-dependent gating currents with the characteristics shown in **Fig. 3.4**. I decided to work with the D160N mutant. The side chains of aspartate and asparagine differ only in the charge, so this mutant is probably the channel that most closely resembles the wild type.

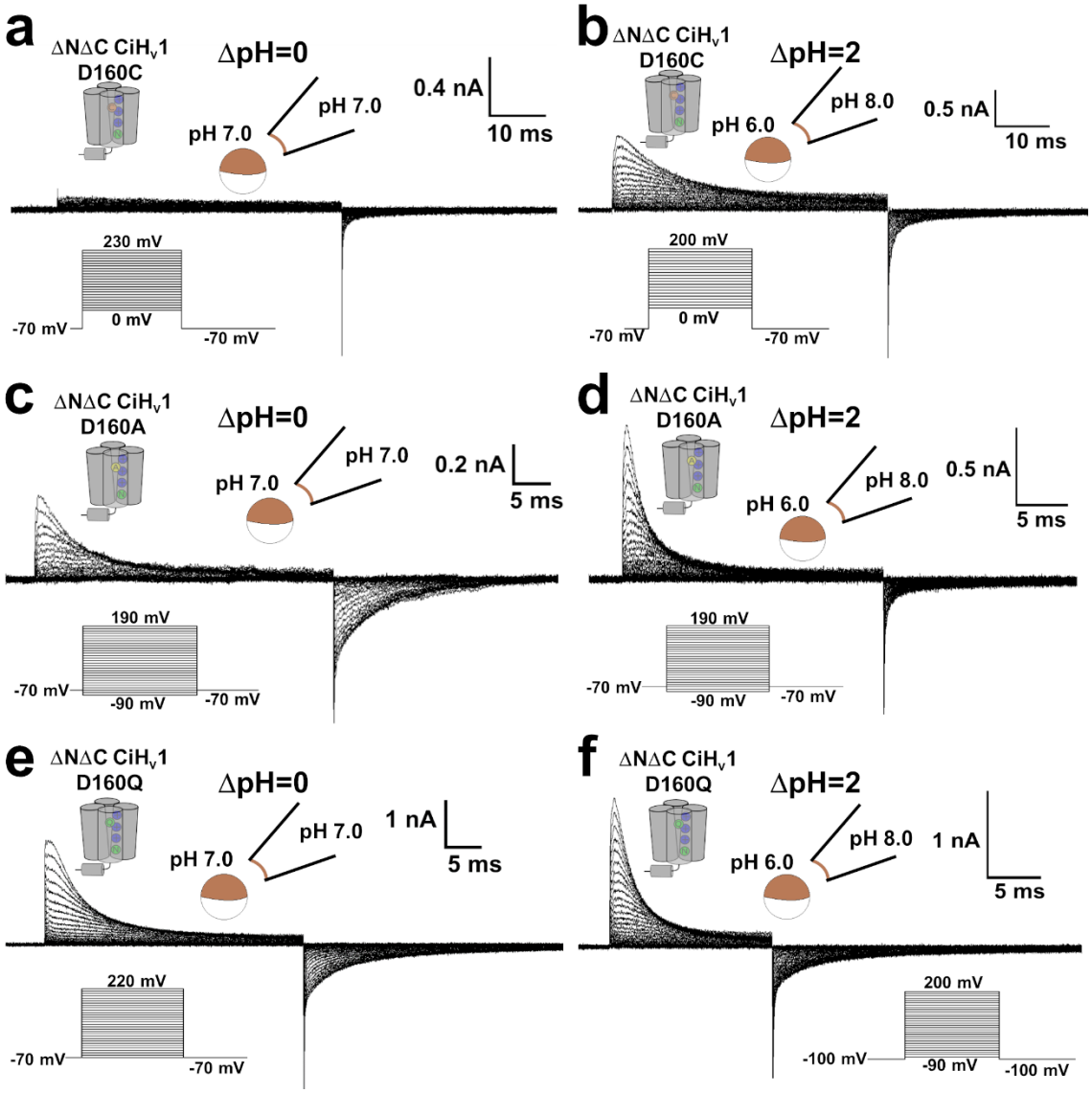

Figure 3.13. Non-conducting monomeric D160 H_v1 mutants produced gating currents. Currents produced by the monomeric H_v1 mutants (a, b) D160C, (c, d) D160A, and (e, f) D160Q. Representative recordings at ΔpH=0 (pH_{in}/pH_{out}=7/7; a, c, and e) and ΔpH=2 (pH_{in}/pH_{out}=6/8; b, d, and f) are shown to demonstrate their pH-dependence. A -P/8 subtraction protocol from a sub-holding potential of -70 mV in (b), (d) and (e), -90 mV in (a) and (c), and -100 mV in (f) was applied.

Although the equivalent D112N mutation in the hH_v1 dimer produces anionic selective currents (Musset et al., 2011; Ramsey et al., 2010), the D160N CiH_v1 dimer does not produce detectable ion currents (Mony et al., 2015). I was able to measure gating currents

in the dimeric D160N CiH$_v$1 mutant at high ΔpH, but the main current component was small and slow (**Fig. 3.14**).

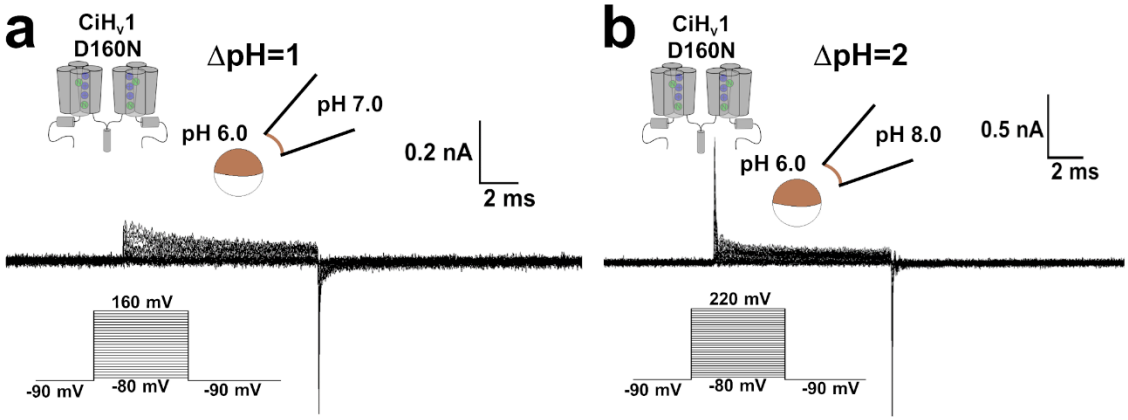

Figure 3.14. Dimeric D160N H$_v$1 mutant produced gating currents. Currents produced by the dimeric D160N H$_v$1 at (a) ΔpH=1 and (b) ΔpH=2. A -P/8 subtraction protocol from a sub-holding potential of -90 mV was applied.

The non-conducting phenotype of some H$_v$1 selectivity filter mutations indicates that they alter the channel opening. This claim is supported by the loss of a fluorescence signal component related to channel opening of the dimeric CiH$_v$1 D160C mutant labeled in S4 (Chamberlin et al., 2015), and the slow fluorescence changes of D160N mutant labeled in S1 (Mony et al., 2015). My data suggest that this alteration increased the energy needed to activate the VSD. The monomeric conducting channel's G-V curves were not preceded in the voltage axis by the Q-V curves of the D160N mutant. Moreover, the D160N mutant Q-V curve is shifted to more positive voltages compared to the N264R mutant curve ($V_{0.5}$=55 mV at symmetrical pH 7) (Carmona et al., 2018). A similar shift on the fluorescence-voltage (F-V) curves has been reported for the D160N mutant compared with wild-type dimers labeled in S4 (Mony et al., 2015). These shifts suggest that the H$_v$1 VSD active states are stabilized by electrostatic interactions between the negatively charged D160 in S1 and the positively gating charges in S4. This interaction has been

proposed previously for the open channel by measuring H_v1 ion currents (Berger and Isacoff, 2011), fluorescence (Chamberlin et al., 2015; Mony et al., 2015), and modeling (Chamberlin et al., 2014; Chamberlin et al., 2015; Geragotelis et al., 2020; Gianti et al., 2016; Kulleperuma et al., 2013; Lee et al., 2018; van Keulen et al., 2017). Therefore, the H_v1 selectivity filter is also related to the channel opening and the VSD activation.

3.5.4 Molecular mechanism of pH sensitivity in H_v1

The direction of the ΔpH-dependent Q-V shifts suggests that the electric field across the membrane sensed by the protein is being changed. This change could be produced by an alteration of the local surface potential by the ΔpH. A proton gradient can change the surface potential by screening the negative charges on the membrane surface (Frankenhaeuser and Hodgkin, 1957; Hille, 1968), similar to increasing the ionic strength by monovalent or divalent cations (Gilbert and Ehrenstein, 1970; Hahin and Campbell, 1983; Hille et al., 1975). For the case of protons, probably a covalent bonding to the negative surface charges could occur according to the Gouy-Chapman-Stern theory (Moczydlowski et al., 1985). The negative surface charges are located in the membrane lipids (Cukierman et al., 1988; Moczydlowski et al., 1985), but mainly on the protein surface itself (Cukierman et al., 1988; MacKinnon et al., 1989). Therefore, changes in the surface potential caused by ΔpH can be attributed to a different degree of protonation in the amino acids on the protein surface. A similar model has been proposed to explain the ΔpH dependence of the channel by altering the closed-open equilibrium (DeCoursey, 2018). However, my data showed that this model applied to the R-A equilibrium of the H_v1 VSD.

A low pH_{in} (greater ΔpH) protonates charged amino acids on the H_v1 internal vestibule. This will produce a more positive internal surface potential, destabilizing the R states of

the VSD by disfavoring the internal location of the positive gating charges consisting of arginine residues in S4 (Gonzalez et al., 2010; Gonzalez et al., 2013). Following the same reasoning, when a high pH_{out} value increases ΔpH, external deprotonations will produce a more negative external surface potential, stabilizing the VSD A states. However, my data suggest that in this case, ΔG^* must also decrease. Therefore, the stabilization of the A states by high pH_{out} has to be accompanied by other modifications, such as decreasing the highest energy barrier or destabilizing the R states by an allosteric effect.

The different internal and external pH dependence mechanisms in H_v1 is in agreement with the known channel modifications that alter this property. Changes in the internal surface potential could explain the pH_{in} dependence alterations (Berger et al., 2017; Cherny et al., 2018) since the modifications are located on the channel's inner side. However, it is harder to explain the alteration of the pH_{out} dependence by W207 in hH_v1 (Cherny et al., 2015) only by a change in the external surface potential because tryptophan does not contain a protonatable side chain. This difficulty requires an additional mechanism to explain the pH_{out} dependence similar to my proposal discussed above. Therefore, although pH modulates the H_v1 VSD in a complicated state-dependent manner, my simplified model can explain most of the results related to the channel pH dependency.

3.6 References

Alvarez, O., Castillo, K., Carmona, E., Gonzalez, C., and Latorre, R. 2019. Methods for Investigating TRP Channel Gating, *Methods Mol Biol* 1987, 167-185.

Armstrong, C.M., and Bezanilla, F. 1973. Currents related to movement of the gating particles of the sodium channels, *Nature* 242, 459-461.

Barish, M.E., and Baud, C. 1984. A voltage-gated hydrogen ion current in the oocyte membrane of the axolotl, Ambystoma, *J Physiol* 352, 243-263.

Berger, T.K., Fussholler, D.M., Goodwin, N., Bonigk, W., Muller, A., Dokani Khesroshahi, N., Brenker, C., Wachten, D., Krause, E., Kaupp, U.B., and Strunker, T. 2017. Post-translational cleavage of Hv1 in human sperm tunes pH- and voltage-dependent gating, *J Physiol* 595, 1533-1546.

Berger, T.K., and Isacoff, E.Y. 2011. The pore of the voltage-gated proton channel, *Neuron* 72, 991-1000.

Bernheim, L., Krause, R.M., Baroffio, A., Hamann, M., Kaelin, A., and Bader, C.R. 1993. A voltage-dependent proton current in cultured human skeletal muscle myotubes, *J Physiol* 470, 313-333.

Bezanilla, F. 2018. Gating currents, *J Gen Physiol* 150, 911-932.

Bezanilla, F., Taylor, R.E., and Fernandez, J.M. 1982. Distribution and kinetics of membrane dielectric polarization. 1. Long-term inactivation of gating currents, *J Gen Physiol* 79, 21-40.

Boonamnaj, P., and Sompornpisut, P. 2019. Effect of Ionization State on Voltage-Sensor Structure in Resting State of the Hv1 Channel, *J Phys Chem B* 123, 2864-2873.

Bruening-Wright, A., and Larsson, H.P. 2007. Slow conformational changes of the voltage sensor during the mode shift in hyperpolarization-activated cyclic-nucleotide-gated channels, *J Neurosci* 27, 270-278.

Byerly, L., Meech, R., and Moody, W., Jr. 1984. Rapidly activating hydrogen ion currents in perfused neurones of the snail, Lymnaea stagnalis, *J Physiol* 351, 199-216.

Carmona, E.M., Larsson, H.P., Neely, A., Alvarez, O., Latorre, R., and Gonzalez, C. 2018. Gating charge displacement in a monomeric voltage-gated proton (Hv1) channel, *Proceedings of the National Academy of Sciences of the United States of America* 115, 9240-9245.

Chamberlin, A., Qiu, F., Rebolledo, S., Wang, Y., Noskov, S.Y., and Larsson, H.P. 2014. Hydrophobic plug functions as a gate in voltage-gated proton channels, *Proceedings of the National Academy of Sciences of the United States of America* 111, E273-282.

Chamberlin, A., Qiu, F., Wang, Y., Noskov, S.Y., and Larsson, H.P. 2015. Mapping the gating and permeation pathways in the voltage-gated proton channel Hv1, *J Mol Biol* 427, 131-145.

Cherny, V.V., Markin, V.S., and DeCoursey, T.E. 1995. The voltage-activated hydrogen ion conductance in rat alveolar epithelial cells is determined by the pH gradient, *J Gen Physiol* 105, 861-896.

Cherny, V.V., Morgan, D., Musset, B., Chaves, G., Smith, S.M., and DeCoursey, T.E. 2015. Tryptophan 207 is crucial to the unique properties of the human voltage-gated proton channel, hHV1, *J Gen Physiol* 146, 343-356.

Cherny, V.V., Morgan, D., Thomas, S., Smith, S.M.E., and DeCoursey, T.E. 2018. Histidine(168) is crucial for DeltapH-dependent gating of the human voltage-gated proton channel, hHV1, *J Gen Physiol* 150, 851-862.

Cherny, V.V., Murphy, R., Sokolov, V., Levis, R.A., and DeCoursey, T.E. 2003. Properties of single voltage-gated proton channels in human eosinophils estimated by noise analysis and by direct measurement, *J Gen Physiol* 121, 615-628.

Cukierman, S., Zinkand, W.C., French, R.J., and Krueger, B.K. 1988. Effects of membrane surface charge and calcium on the gating of rat brain sodium channels in planar bilayers, *J Gen Physiol* 92, 431-447.

De La Rosa, V., and Ramsey, I.S. 2018. Gating Currents in Hv1 Proton Channels, *Biophysical Journal* 114, 124a.

DeCoursey, T.E. 1991. Hydrogen ion currents in rat alveolar epithelial cells, *Biophys J* 60, 1243-1253.

DeCoursey, T.E. 2018. Voltage and pH sensing by the voltage-gated proton channel, HV1, *J R Soc Interface* 15.

DeCoursey, T.E., and Cherny, V.V. 1994. Voltage-activated hydrogen ion currents, *J Membr Biol* 141, 203-223.

DeCoursey, T.E., Cherny, V.V., Zhou, W., and Thomas, L.L. 2000. Simultaneous activation of NADPH oxidase-related proton and electron currents in human neutrophils, *Proceedings of the National Academy of Sciences of the United States of America* 97, 6885-6889.

Frankenhaeuser, B., and Hodgkin, A.L. 1957. The action of calcium on the electrical properties of squid axons, *J Physiol* 137, 218-244.

Geragotelis, A.D., Wood, M.L., Goddeke, H., Hong, L., Webster, P.D., Wong, E.K., Freites, J.A., Tombola, F., and Tobias, D.J. 2020. Voltage-dependent structural models of the human Hv1 proton channel from long-timescale molecular dynamics simulations, *Proceedings of the National Academy of Sciences of the United States of America* 117, 13490-13498.

Gianti, E., Delemotte, L., Klein, M.L., and Carnevale, V. 2016. On the role of water density fluctuations in the inhibition of a proton channel, *Proceedings of the National Academy of Sciences of the United States of America* 113, E8359-E8368.

Gilbert, D.L., and Ehrenstein, G. 1970. Use of a fixed charge model to determine the pK of the negative sites on the external membrane surface, *J Gen Physiol* 55, 822-825.

Gonzalez, C., Koch, H.P., Drum, B.M., and Larsson, H.P. 2010. Strong cooperativity between subunits in voltage-gated proton channels, *Nat Struct Mol Biol* 17, 51-56.

Gonzalez, C., Rebolledo, S., Perez, M.E., and Larsson, H.P. 2013. Molecular mechanism of voltage sensing in voltage-gated proton channels, *J Gen Physiol* 141, 275-285.

Hahin, R., and Campbell, D.T. 1983. Simple shifts in the voltage dependence of sodium channel gating caused by divalent cations, *J Gen Physiol* 82, 785-805.

Hille, B. 1968. Charges and potentials at the nerve surface. Divalent ions and pH, *J Gen Physiol* 51, 221-236.

Hille, B. 2001. Ionic Channels of Excitable Membranes Sunderland, Massachusetts, U.S.A., Sinauer Associates.

Hille, B., Woodhull, A.M., and Shapiro, B.I. 1975. Negative surface charge near sodium channels of nerve: divalent ions, monovalent ions, and pH, *Philos Trans R Soc Lond B Biol Sci* 270, 301-318.

Kapus, A., Romanek, R., Qu, A.Y., Rotstein, O.D., and Grinstein, S. 1993. A pH-sensitive and voltage-dependent proton conductance in the plasma membrane of macrophages, *J Gen Physiol* 102, 729-760.

Keynes, R.D., and Rojas, E. 1973. Characteristics of the sodium gating current in the squid giant axon, *J Physiol* 233, 28P-30P.

Koch, H.P., Kurokawa, T., Okochi, Y., Sasaki, M., Okamura, Y., and Larsson, H.P. 2008. Multimeric nature of voltage-gated proton channels, *Proceedings of the National Academy of Sciences* 105, 9111-9116.

Kulleperuma, K., Smith, S.M., Morgan, D., Musset, B., Holyoake, J., Chakrabarti, N., Cherny, V.V., DeCoursey, T.E., and Pomes, R. 2013. Construction and validation of a homology model of the human voltage-gated proton channel hHV1, *J Gen Physiol* 141, 445-465.

Lee, M., Bai, C., Feliks, M., Alhadeff, R., and Warshel, A. 2018. On the control of the proton current in the voltage-gated proton channel Hv1, *Proceedings of the National Academy of Sciences of the United States of America* 115, 10321-10326.

Lee, S.Y., Letts, J.A., and Mackinnon, R. 2008. Dimeric subunit stoichiometry of the human voltage-dependent proton channel Hv1, *Proceedings of the National Academy of Sciences of the United States of America* 105, 7692-7695.

MacKinnon, R., Latorre, R., and Miller, C. 1989. Role of surface electrostatics in the operation of a high-conductance Ca2+-activated K+ channel, *Biochemistry* 28, 8092-8099.

Moczydlowski, E., Alvarez, O., Vergara, C., and Latorre, R. 1985. Effect of phospholipid surface charge on the conductance and gating of a Ca2+-activated K+ channel in planar lipid bilayers, *J Membr Biol* 83, 273-282.

Mony, L., Berger, T.K., and Isacoff, E.Y. 2015. A specialized molecular motion opens the Hv1 voltage-gated proton channel, *Nat Struct Mol Biol* 22, 283-290.

Musset, B., Smith, S.M., Rajan, S., Morgan, D., Cherny, V.V., and Decoursey, T.E. 2011. Aspartate 112 is the selectivity filter of the human voltage-gated proton channel, *Nature* 480, 273-277.

Okochi, Y., Sasaki, M., Iwasaki, H., and Okamura, Y. 2009. Voltage-gated proton channel is expressed on phagosomes, *Biochem Biophys Res Commun* 382, 274-279.

Qiu, F., Chamberlin, A., Watkins, B.M., Ionescu, A., Perez, M.E., Barro-Soria, R., Gonzalez, C., Noskov, S.Y., and Larsson, H.P. 2016. Molecular mechanism of Zn2+ inhibition of a voltage-gated proton channel, *Proceedings of the National Academy of Sciences of the United States of America* 113, E5962-E5971.

Qiu, F., Rebolledo, S., Gonzalez, C., and Larsson, H.P. 2013. Subunit interactions during cooperative opening of voltage-gated proton channels, *Neuron* 77, 288-298.

Ramsey, I.S., Mokrab, Y., Carvacho, I., Sands, Z.A., Sansom, M.S.P., and Clapham, D.E. 2010. An aqueous H+ permeation pathway in the voltage-gated proton channel Hv1, *Nat Struct Mol Biol* 17, 869-875.

Ramsey, I.S., Moran, M.M., Chong, J.A., and Clapham, D.E. 2006. A voltage-gated proton-selective channel lacking the pore domain, *Nature* 440, 1213-1216.

Ramsey, I.S., Ruchti, E., Kaczmarek, J.S., and Clapham, D.E. 2009. Hv1 proton channels are required for high-level NADPH oxidase-dependent superoxide production during the phagocyte respiratory burst, *Proceedings of the National Academy of Sciences of the United States of America* 106, 7642-7647.

Sasaki, M., Takagi, M., and Okamura, Y. 2006. A voltage sensor-domain protein is a voltage-gated proton channel, *Science* 312, 589-592.

Tombola, F., Ulbrich, M.H., and Isacoff, E.Y. 2008. The voltage-gated proton channel Hv1 has two pores, each controlled by one voltage sensor, *Neuron* 58, 546-556.

Tombola, F., Ulbrich, M.H., Kohout, S.C., and Isacoff, E.Y. 2010. The opening of the two pores of the Hv1 voltage-gated proton channel is tuned by cooperativity, *Nat Struct Mol Biol* 17, 44-50.

van Keulen, S.C., Gianti, E., Carnevale, V., Klein, M.L., Rothlisberger, U., and Delemotte, L. 2017. Does Proton Conduction in the Voltage-Gated H(+) Channel hHv1 Involve Grotthuss-Like Hopping via Acidic Residues?, *J Phys Chem B* 121, 3340-3351.

Villalba-Galea, C.A. 2014. Hv1 proton channel opening is preceded by a voltage-independent transition, *Biophys J* 107, 1564-1572.

Villalba-Galea, C.A., Sandtner, W., Starace, D.M., and Bezanilla, F. 2008. S4-based voltage sensors have three major conformations, *Proceedings of the National Academy of Sciences of the United States of America* 105, 17600-17607.

CHAPTER 4

GENERAL DISCUSSION AND CONCLUSIONS

4.1 The monomeric channel as a H_v1 simple model

The unique structural and biophysical characteristics of the voltage-gated proton channel (H_v1) make it an interesting protein to study. H_v1 is a homodimer with subunits of around 32 kDa in human H_v1 (hH_v1) and 38 kDa in *Ciona intestinalis* H_v1 (CiH_v1). The protein has an intracellular N-terminal domain of variable length between different species, a voltage sensor domain (VSD) of four transmembrane helices (from S1 to S4), and an intracellular C-terminal domain (Ramsey et al., 2006; Sasaki et al., 2006). The amino acid sequence of the N-terminal domain is predicted to fold as an intrinsically disordered protein, but its function is unknown. The C-terminal domain forms a coiled-coil between subunits, which stabilize the dimer (Fujiwara et al., 2012; Li et al., 2010). Finally, the transmembrane domain forms the VSD of the protein. H_v1 structure is straightforward compared to other voltage-gated ion channels. The basic architecture of these proteins includes four repetitions of a VSD coupled to a pore domain (helices S5 and S6) (Catterall, 1995; Hille, 2001). Despite its structural simplicity, H_v1 contains a highly selective permeation pathway for protons, a VSD, and pH sensors. The H_v1 sensors modulate the opening of the permeation pathway, so the channel gating is voltage- and pH-dependent (Cherny et al., 1995). However, the molecular mechanisms that explain how each of these processes works in the protein and how they modulate each other are still poorly understood. The problem is unique compared with other ion channels since the processes are localized in the same structural domain for H_v1. For other channels, voltage sensing, ligand binding, and permeation are localized in different protein domains (Hille, 2001). One important strategy to gain a better understanding of H_v1 gating is to

study the structure to explain the function. However, progress in the study of the H_v1 structure has been poor. The only crystal structure available of the channel is a chimera consisting of the VSD of the mouse H_v1 with a replacement of one portion of the S2 and S3 helices by the voltage-sensing phosphatase (VSP), and the C-terminal domain by the coiled-coil of the yeast transcription factor GCN4 (Takeshita et al., 2014). Although this structure constituted an advance in the field, it has a series of caveats: chimeric channel formed a trimer instead of a dimer, crystals were formed with the inhibitor Zn^{2+} bound to the protein, and resolution of the structure was too low to localize the amino acid positions (3.45 Å) (Takeshita et al., 2014). Recently, a nuclear magnetic resonance (NMR) structure of a monomeric hH_v1 was obtained (Bayrhuber et al., 2019). In this case, the structure model was build using 100 different conformers. However, the NMR structure was obtained in the presence of Zn^{2+} (Bayrhuber et al., 2019). The presence of Zn^{2+} in both structures is problematic since this Hv1 inhibitor changes the channel (Qiu et al., 2016). Due to the little structural information, H_v1 gating has been studied mainly using electrophysiology. These studies have revealed the unique properties of Hv1, including its voltage- and pH-dependent gating (DeCoursey, 2018), high selectivity for protons (Berger and Isacoff, 2011; Musset et al., 2011), small unitary conductance (Cherny et al., 2003), and cooperativity of opening (Gonzalez et al., 2010; Tombola et al., 2010). As all these properties are present simultaneously in the native H_v1 channel, it has been difficult to find each of these biophysical properties' molecular mechanisms. I proposed that a better approach to understand the basic mechanisms of H_v1 gating is to use the simple monomeric channel. In this channel, the N- and C-terminal domain are removed by deleting the first 128 amino acids and introducing a stop codon replacing the valine 270 in CiH_v1. The resultant channel is a monomer that produced robust voltage- and pH-dependent currents with faster kinetics of activation (Koch et al., 2008). Faster channel

activation is probably caused by suppressing the channel cooperativity through the deletion of the coiled-coil structure (Gonzalez et al., 2010; Koch et al., 2008). Although there was a basic characterization of this channel in the literature (Gonzalez et al., 2010; Koch et al., 2008), a more detailed study was needed to validate this channel as a model to study H_v1 gating. Undoubtedly, this is one of the contributions of this thesis to the H_v1 community. I characterized the channel voltage dependence, pH dependence, and selectivity. I found that all these hallmark properties of H_v1 are maintained in the monomeric channel, demonstrating that this is a simple model for understanding H_v1 gating. The knowledge gained with the monomeric channel can be used later to understand the more complex native channel. This strategy to understand ion channels is not new in the field. The *Shaker* potassium channel, one of the best characterized voltage-gated ion channels, has used a construct with a deletion of the residues 6 to 46 in the N-terminal domain (ShH4-IR) to study the channel properties (Aggarwal and MacKinnon, 1996; Bezanilla et al., 1994; Gonzalez et al., 2005; Gonzalez et al., 2000, 2001; Hoshi et al., 1994; Larsson et al., 1996; Perozo et al., 1993; Perozo et al., 1992; Perozo et al., 1994; Stefani et al., 1994; Yellen et al., 1991; Zagotta et al., 1994a; Zagotta et al., 1994b). This deletion in *Shaker* removes the fast N-type inactivation (Hoshi et al., 1990), simplifying the interpretation of the results just as the monomeric H_v1 simplifies the interpretation of results by removal of the cooperativity. In conclusion, I proposed and validated the monomeric channel as a model to understand the fundamental questions regarding H_v1 gating. I took the first steps in this new approach studying H_v1 gating currents, which is possible only in the monomeric channel.

4.2 Gating currents of H_v1

Understanding the molecular mechanisms of gating in ion channels allows manipulating the channel's physiological and pathophysiological role. In order to change the protein

function, a detailed picture of how the protein work is needed. To accomplish this for voltage-gated ion channels, a series of functional measurements can be done: macroscopic ionic currents, single-channel recordings, and gating currents. Ion fluxes produce macroscopic ionic currents and single-channel recordings through the channel's pore, so these measurements mainly contain information of the channel's open states or closed states near the open conformations (Hille, 2001). The missing information of the closed states can be obtained from gating currents, which are the direct measurement of the VSD movements during activation and deactivation (Almers, 1978; Armstrong and Bezanilla, 1973; Bezanilla, 2018; Keynes and Rojas, 1973). Unfortunately, H_v1 studies have almost exclusively used macroscopic ionic currents. The extremely small magnitude of H_v1 single-channel currents has limited its use (Cherny et al., 2003). On the other hand, H_v1 gating currents measurements remained elusive due to the slow channel activation, the inability to remove protons from the solution, and the absence of blockers suppressing proton permeation without modifying the VSD movements. Despite this, H_v1 VSD movements had been studied by indirect methodologies including accessibility assays and voltage-clamp fluorometry (VCF) (Gonzalez et al., 2010; Gonzalez et al., 2013; Mony et al., 2015; Qiu et al., 2013). Although these studies contributed to the advancement of H_v1 understanding, the direct measurement of the VSD movements was still needed. This thesis contributed to achieving the measurement of H_v1 gating currents. I used the monomeric channel as a simplified model of H_v1 VSD because the activation of this channel is faster than the native dimeric channel. Although the best model to study H_v1 VSD movements would be the wild type monomeric channel, the presence of proton currents in this channel contaminated gating currents. Therefore, I introduced two independent mutations: N264R and D160N. The monomeric N264R H_v1 mutant is a low-conducting channel, while the monomeric D160N H_v1 is a non-conducting channel. First,

I used the N264R mutant to demonstrate that the initial transient currents produced by this channel fulfilled the requirements of truly gating currents (Almers, 1978): (i) to be part of an asymmetric component of the capacitive currents; (ii) to show saturation of the displaced charge at high voltages; (iii) to have voltage-dependent kinetics; and (iv) to show equal charge displaced during activation and deactivation. The D160N mutant also fulfilled these requirements, but the most detailed demonstration was published using the N264R mutant (Carmona et al., 2018). Although the use of the monomeric N264R mutant was the first approach to study H_v1 gating currents, the model had some limitations. First, as the N264R mutant is a low-conducting channel, I had to isolate the gating currents from the small proton current using a mathematical approach. Secondly, and most importantly, the N264R mutation introduced trapping of the gating charge. The deactivation of this mutant VSD is so slow that most of the OFF-gating current was below the detection limit. Despite this, the conductance-voltage (G-V) curve of the N264R mutant had the same voltage dependence as the wild type channel, suggesting this is a good model to study the coupling between the VSD and the permeation pathway in H_v1. Later, when I wanted to study the pH dependence of Hv1 gating currents, the low-conducting N264R mutant was not useful since the proton currents heavily contaminated gating currents. I solved this problem by introducing mutations in the selectivity filter, D160, which had been reported to produce non-conducting channels without disrupting the VSD movements (Berger and Isacoff, 2011; Chamberlin et al., 2015; Musset et al., 2011). Some of these mutants produced isolated gating currents with the same components of gating charge displacement shown by the monomeric N264R channel. I performed a detailed study of the monomeric D160N mutant channel since this mutation imposed fewer alterations to the channel. This second mutant channel is a good model for studying the H_v1 VSD in the absence of its permeation pathway, which was I needed

to study the pH dependence. The discovery of this new model contributes significantly to the voltage-gated ion channel community since this is the first time the VSD H_v1 movements can be measured directly from isolated gating currents. The monomeric D160N will be one of the reference models to study gating currents in H_v1 as the non-conducting W434F mutant of the *Shaker* potassium channel became one of the reference models to study gating currents in the absence of potassium currents (Perozo et al., 1993). However, in potassium channels, there are other tools to eliminate or decrease ionic currents, including potassium removal or pharmacological approaches (Bezanilla, 2018), which is not the case for the proton currents in H_v1.

Using the new models to measure H_v1 gating currents, I showed new features of the channel's VSD movements. Gating currents of the monomeric H_v1 had the same components for both models (N264R and D160N mutants), validating the results obtained since two independent mutations produced similar outcomes. The shape of the H_v1 gating currents immediately revealed the unique movements of the VSD during activation and deactivation, differing markedly from gating currents from sodium and potassium voltage-gated ion channels (Bezanilla, 2018). H_v1 ON-gating currents have a faster component followed by a slower one, which showed a rising phase. The proportion of these components changed when the prepulse voltage changes, producing a marked Cole-Moore effect on gating currents. The OFF-gating current also has a very fast component, followed by a slower one. Although the amplitude of the OFF-gating current faster component is much higher than the slower component, the last one displaced most of the charge during deactivation. All these characteristics and the detailed analysis I performed showed that the H_v1 VSD goes through many different conformational states during its movements, which constitute an unexpected complexity for this small protein. Undoubtedly, this thesis has taken the first steps through a series of exciting discoveries

about the molecular mechanisms of H_v1 gating. Two of the more fundamental questions in H_v1 are related to the coupling of the voltage dependence with both the permeation pathway opening and the pH sensing in the channel. I have started this quest to discover the secrets of the unique H_v1 gating mechanisms.

4.3 Coupling between the voltage sensor and the permeation pathway in H_v1

Voltage-gated ion channels change the opening probability in response to changes in the transmembrane voltage (Hille, 2001). This regulation is possible because these proteins can sense the electric field established across the membrane and couple this sensing process to the opening of the permeation pathway. This process must be related to the protein structure to understand its molecular mechanism. Remarkable advances have been made in this topic since the discovery of the first primary sequence of these type of proteins corresponding to the voltage-gated sodium channel in 1984 (Noda et al., 1984), and followed by the *Shaker* voltage-gated potassium channel (Tempel et al., 1987) and the alpha-1 subunit of the voltage-gated calcium channel (Tanabe et al., 1987). All these channels share a typical architecture consisting of four repetitions of six transmembrane helices (from S1 to S6). The VSD is formed by transmembrane helices from S1 to S4, while the pore domain is formed by transmembrane helices S5 and S6 (Hille, 2001). Therefore, the voltage sensing and the permeation pathway in these channels are in different structural domains of the protein. These processes can also be measured independently by gating currents and ionic currents for the VSD movements and the pore opening, respectively (Armstrong and Bezanilla, 1973; Bezanilla, 2000; Keynes and Rojas, 1973). During the last years, the coupling between the VSD and the pore domain has been studied in voltage-gated ion channels using these measurements. Although the detailed mechanism is still unknown, it has been demonstrated that the S4-S5 linker and non-covalent interactions between S4 and S5 are essential to couple the voltage sensing

and the pore opening (Blunck and Batulan, 2012; Carvalho-de-Souza and Bezanilla, 2019; Chowdhury et al., 2014; Fernandez-Marino et al., 2018; Muroi et al., 2010). The H_v1 primary sequence discovery showed that this channel has a different mechanism since it does not have a pore domain (Ramsey et al., 2006; Sasaki et al., 2006). Therefore, the coupling of the H_v1 VSD and permeation pathway is unique among voltage-gated ion channels since both the voltage sensing and the permeation pathway opening occurred in the same structural domain. The understanding of this coupling in H_v1 requires first studying both processes independently. Due to the similarity of the H_v1 VSD with other voltage-gated ion channels, the H_v1 voltage dependence has been studied more than the proton permeation. The H_v1 VSD is a four transmembrane structure (from S1 to S4) with three conserved arginine residues in S4. These positively charged amino acids produced the channel voltage dependence (Gonzalez et al., 2013). Using accessibility assays and VCF, it has been demonstrated that there are changes in S1 and S4 during the VSD activation (Gonzalez et al., 2010; Mony et al., 2015; Qiu et al., 2013). S4 changes are related to voltage sensing, while S1 changes are correlated with the permeation pathway opening (Mony et al., 2015).

On the other hand, the Hv1 permeation is less understood. The channel is highly selective to protons (Cherny et al., 1995). The permeation pathway determinants are contained in the VSD since deletions of the N- and C-terminal domains produced monomeric channels that still conduct protons selectively (Koch et al., 2008). Additionally, the opening of the permeation pathways in the H_v1 dimer requires the activation of the two VSDs resulting in a cooperative gating (Gonzalez et al., 2010; Tombola et al., 2010). Two models have been proposed to explain the molecular mechanism of permeation in H_v1. The first one proposed a water wire in the channel used for protons to translocate through the membrane (Bennett and Ramsey, 2017), while the second one proposed protons are

transferred through amino acid residues of the protein (DeCoursey, 2017). The first proposal is based experimentally on the inability to suppress currents by single mutations and computational modeling (Ramsey et al., 2010), while the second model has experimental support from different approaches: the demonstration that part of the selectivity filter of the channel is an aspartate located in S1 (Berger and Isacoff, 2011; Musset et al., 2011), the larger isotope effect of H_v1 current amplitude (DeCoursey and Cherny, 1997), and the high-temperature dependence of gating and permeation (DeCoursey and Cherny, 1998; Kuno et al., 2009). Although I still do not know the detailed molecular mechanisms of selectivity and opening in H_v1, they can be studied directly through recording the channel macroscopic ionic currents. However, a similar direct measurement of the VSD has not been possible until now for the case of the H_v1, since it involves gating currents.

The measurement of H_v1 gating currents in this thesis allows me to investigate the coupling between the VSD and the permeation pathway in this channel. Although proton currents contaminated gating currents in the wild type monomeric H_v1, I solved this issue by measuring the monomeric mutants N264R and D160N. N264R mutant is a low-conducting mutant, so it is a better model to study the coupling between the VSD and the permeation pathway of H_v1. Additionally, the G-V curve of this mutant is like the monomeric conducting channel curve, suggesting that the permeation pathway opening is not significantly altered with the introduction of the N264R mutation. As the VSD and the permeation pathway of the Hv1 are in the same structural domain, it was tempting to speculate that in the monomeric channel, the VSD activation and channel opening occurred simultaneously. This last possibility would mean that the monomeric Hv1 follows a two-state model. In this case, the Q-V and G-V curves of the channel should overlap. However, in the N264R monomeric H_v1 mutant, the $V_{0.5}$ of the G-V and Q-V curves were

107 and 55 mV, respectively, demonstrating that the VSD activation and the channel opening occurs in more than one step. Therefore, the gating charge's displacement occurs before the permeation pathway opening (around 88% of the charge has been displaced when the opening probability is 0.5). Moreover, the multiple components of the H_v1 gating currents evidenced that the VSD conformational changes occur before the opening of the channel. I expect that channel opening will occur when the VSD reached one of the last states during activation. The Cole-Moore shift of the proton currents in the monomeric conducting channel confirmed the existence of more than one closed state in this channel.

The second mutant I used to measure H_v1 gating currents was the monomeric D160N channel. As the D160 corresponds to the selectivity filter of the CiH_v1, the introduction of this change produced a non-conducting channel (Berger and Isacoff, 2011; Chamberlin et al., 2015; Musset et al., 2011). The gating currents of this mutant channel maintain the same components of the N264R mutant, indicating that the suppression of the permeation pathway does not alter the VSD movements. However, the mutant Q-V curve was shifted to the right compared to the monomeric N264R mutant in the same experimental conditions, ($V_{0.5}$ of 138 mV for the non-conducting channel and 55 mV for the low-conducting mutant) (Carmona et al., 2018). I propose that this Q-V curve shift is produced by the absence of the permeation pathway in the D160N mutant. Therefore, the channel opening favors the voltage sensor activation in H_v1. To calculate an approximate magnitude of this energy, we calculated the median voltage of activation from the Q-V curves (Chowdhury and Chanda, 2012), which resulted in 61 and 133 mV for the N264R and D160N mutants, respectively. Assuming a maximum charge per channel of 3.0 elementary charge (Gonzalez et al., 2010; Gonzalez et al., 2013), the free-energy difference between both mutants would be around 21 kJ/mole. Interestingly, the

free-energy for the protonation of the aspartate side chain is around 22 kJ/mole (pK_a=3.90) (Voet and Voet, 2010). This calculation suggests that the negative charge of the aspartate 160 decreases the energy needed to activate the VSD in the monomeric H_v1. As this residue has been demonstrated to have a crucial role in proton permeation (Berger and Isacoff, 2011; Musset et al., 2011), these energy changes of the VSD movements in the mutant channels suggests D160 is essential coupling the voltage dependence with the permeation pathway opening in the monomeric H_v1 channel. However, more structural studies are needed to confirm this as the aspartate pK_a value can be modulated by the protein environment. In conclusion, the monomeric H_v1 activation involved several closed states before reaching the open state. Consequently, VSD activation and channel opening are kinetically different, despite occurring in the same structural domain. Finally, I propose that the channel's selectivity filter D160 is crucial to couple the VSD activation with the channel opening in H_v1.

4.4 Coupling between the voltage sensor and ΔpH in H_v1

Although the most studied stimulus that modified the open probability of voltage-gated ion channels is the electric field established across the membrane, other stimuli can modify the channel open probability (Hille, 2001). Proton concentration, quantified by the pH, is one of these modifiers. A decrease of the intracellular pH or an increase of the extracellular pH tends to favor the channel opening and the kinetics of activation in a reversible manner for a variety of voltage-gated channels including voltage-gated potassium channels (Carbone et al., 1978; Carbone et al., 1981; Deutsch and Lee, 1989; Hedrich et al., 1995; Mozhayeva and Naumov, 1970; Schauf and Davis, 1976; Shrager, 1974), voltage-gated sodium channels (Campbell and Hahin, 1984; Carbone et al., 1978; Carbone et al., 1981; Ehrenstein and Fishman, 1971; Hille, 1968; Hille et al., 1975;

Nonner et al., 1980; Schauf and Davis, 1976; Zhang and Siegelbaum, 1991) and voltage-gated calcium channels (Iijima et al., 1986; Klockner and Isenberg, 1994; Krafte and Kass, 1988). These results have been explained by the existence of a local surface potential produced by negative charges on the membrane's surface. Thus the total electrical potential across the membrane would be the sum of this surface potential and the imposed potential established between bulk solutions (Frankenhaeuser and Hodgkin, 1957; Hille, 2001; Hille et al., 1975). Protons would alter the local surface potential by screening this surface negative charge forming an electrical double layer according to the Gouy-Chapman-Stern theory, similar to the effect of increasing the ionic strength by monovalent or divalent cations (Frankenhaeuser and Hodgkin, 1957; Gilbert and Ehrenstein, 1970; Hahin and Campbell, 1983; Hille et al., 1975). It is well known that the negative surface charges of the membrane screened by positive cations are in the lipids of the bilayer (Cukierman et al., 1988; Moczydlowski et al., 1985), but mainly in the protein surface itself (Cukierman et al., 1988; MacKinnon et al., 1989). In particular, changes in the surface potential caused by pH have been attributed to protonation of the channel amino acids. These protonatable residues would be the pH sensors in the proteins. Histidine residues located close to the pore are extracellular pH sensors in the voltage-gated potassium channels Kv1.4 (Ishii et al., 2001), Kv1.5 (Kehl et al., 2002; Kwan et al., 2006; Steidl and Yool, 1999; Trapani and Korn, 2003), KCNQ2/3 (Kv7.2/3) (Prole et al., 2003), the plant potassium channel KST1 (Hoth et al., 1997), and voltage-gated sodium channels (Jones et al., 2013). On the other hand, aspartate and glutamate are pH sensors in voltage-gated sodium channels (Khan et al., 2002), voltage-gated calcium channels (Chen et al., 1996), and the large-conductance calcium-activated potassium channel Slo1 (Zhou et al., 2018). Although changes in the local surface potential have successfully explained the pH dependence in many voltage-gated ion channels, this theory has its

limitations. The Gouy-Chapman-Stern theory did not consider the dynamics of proteins, so it will fail when screening of the charges occurred in a state-dependent manner. These limitations were noted for the state-dependent binding of cations in voltage-gated potassium and sodium channels (Armstrong and Cota, 1990; Gilly and Armstrong, 1982a, b). Therefore, detailed kinetic studies are necessary to find the specific alteration in the mechanism of activation of ion channels by protons. These studies suggest that pH specifically alters the C-type inactivation in the voltage-gated potassium channels Kv1.4 (Claydon et al., 2000; Claydon et al., 2002), Kv1.5 (Zhang et al., 2003) and *Shaker* (Claydon et al., 2007; Starkus et al., 2003). On the other hand, changes in single-channel sub-conductance states are modulated by pH in the voltage-gated potassium channel KCNQ2/3 (Kv7.2/3) (Prole et al., 2003) and voltage-gated calcium channels (Krafte and Kass, 1988; Pietrobon et al., 1989; Prod'hom et al., 1987, 1989). In summary, although the local surface potential theory explains the general effects of pH in voltage-gated ion channels, other mechanisms are needed to understand the specific effect.

The pH dependency of the H_v1 channel is unique compared to other voltage-gated ion channels since the gating of the channel is modulated by the pH gradient or ΔpH ($pH_{out} - pH_{in}$) established across the membrane (Cherny et al., 1995). The G-V curves of the channel shifted to the left as ΔpH increased so that the H_v1 channel opens only when the membrane voltage is greater than the equilibrium potential for protons obtained from the Nernst equation. Therefore, only Hv1 outward currents are produced, which is important for the channel's physiological function. Kinetics of activation are also shifted according to the ΔpH, so a greater gradient increases the open probability and the rate of channel opening to favor proton extrusion (Cherny et al., 1995). Although some mutations change the pH sensitivity of the H_v1 channel (Berger et al., 2017; Cherny et al., 2015; Cherny et

al., 2018), no mutation completely suppressed neither the internal nor the external pH sensitivity of H_v1 proton currents. This unusual ΔpH dependence makes the molecular mechanism of H_v1 pH sensitivity obscure. I proposed that a better understanding of the pH sensitivity requires a simplification of the model. It is hard to understand the mechanism of action of protons analyzing only proton currents of the native H_v1 since this does not separate the effect of pH on permeation, voltage sensing, and cooperativity. In particular, I would like to separate the coupling of the pH sensor(s) with the VSD and the permeation pathway, which cannot be obtained by measuring only macroscopic proton currents of the H_v1 dimer. To accomplish that goal, a detailed study of the independent effects of pH on the VSD and the permeation pathway would be desirable. Following this reasoning, during this thesis, I validated the monomeric H_v1 channel as a model to study pH dependence in the absence of channel cooperativity. The ΔpH modulates both G-V curves and kinetics of activation in the monomeric channel. Next, to study the effect of pH on the VSD, I introduced a single mutation in one amino acid of the selectivity filter of the H_v1 channel, D160. This mutation produced non-conducting channels allowing me to explore the effect of pH on the VSD movements in absence proton currents. The Q-V curves and the kinetics of the ON-gating currents of the non-conducting channel still shifted according to the ΔpH to favor VSD activation. The energy difference between the Q-V curves when ΔpH increased in two units was around -8 kJ/mol, assuming a two-state model for the VSD activation. Although this energy calculation is not precise since the H_v1 VSD activation involves several states, it suggests a strong coupling between VSD activation and ΔpH. More importantly, my results showed for the first time that ΔpH increased H_v1 channel opening mainly by favoring VSD activation. An increase of the ΔpH involved (i) a decrease of the energy difference between the resting and active states

of the VSD, which will explain the shift of the Q-V curves; and (ii) a decrease of the height of the energy barrier from the slowest transition, which will explain the increase of the kinetics of activation. Both effects can be reproduced if the ΔpH destabilizes the resting states of the H_v1 VSD. This finding has important consequences for the possible molecular mechanism of the pH dependence of H_v1. The most accepted proposal until now to explain this is the so-called counter-charge model (DeCoursey, 2018). In this model, the negatively charged aspartate and glutamate residues in S1, S2, and S3 interact electrostatically with the positive gating charged in S4 (R255, R258, and R261 in CiH_v1). The negative amino acids are located both in the internal and external vestibules of the H_v1 channel. Their charge can be neutralized by protonation of their side chain at low pH values. Therefore, low internal pH value will neutralize the internal negative charges of the channel destabilizing the closed channel (and the VSD resting states). In contrast, low external pH value will stabilize the open channel (and active VSD states) by neutralizing the external negative charges (DeCoursey, 2018). Although not explicitly stated by the author, this model implies that the mechanism explaining the pH dependence of H_v1 is a change of the local surface potential due to the screening of negative charges according to the Gouy-Chapman-Stern theory. However, my data suggest that there would be an additional effect when the external pH value increases because this change produced a decrease of the energetic barrier height from the resting to the active states of the VSD. Therefore, high external pH will produce either a destabilization of the VSD resting states or a decrease in the energy barrier of activation and the stabilization of the VSD active states. In any case, the external pH dependency of H_v1 is not only produced by a stabilization of the VSD active states, as has been proposed in the counter-charge model. Moreover, the Hv1 gating currents kinetics strongly suggests that the pH dependency of VSD movements is state-dependent. In

conclusion, this thesis has contributed to revealing new insights into the molecular mechanisms of the pH dependency of H_v1 channels. The H_v1 VSD has an intrinsic pH dependency allowing it to sense the pH gradient established across the membrane. An increase of the ΔpH (pH_{out} – pH_{in}) decreased the energy difference between the resting and active configurations of the VSD and the height of the higher energy barrier of activation. The simplest explanation of these results is that ΔpH destabilizes the VSD resting states of the H_v1 channel.

4.5 References

Aggarwal, S.K., and MacKinnon, R. 1996. Contribution of the S4 segment to gating charge in the Shaker K+ channel, *Neuron* 16, 1169-1177.

Almers, W. 1978. Gating currents and charge movements in excitable membranes, *Rev Physiol Biochem Pharmacol* 82, 96-190.

Armstrong, C.M., and Bezanilla, F. 1973. Currents related to movement of the gating particles of the sodium channels, *Nature* 242, 459-461.

Armstrong, C.M., and Cota, G. 1990. Modification of sodium channel gating by lanthanum. Some effects that cannot be explained by surface charge theory, *J Gen Physiol* 96, 1129-1140.

Bayrhuber, M., Maslennikov, I., Kwiatkowski, W., Sobol, A., Wierschem, C., Eichmann, C., Frey, L., and Riek, R. 2019. Nuclear Magnetic Resonance Solution Structure and Functional Behavior of the Human Proton Channel, *Biochemistry* 58, 4017-4027.

Bennett, A.L., and Ramsey, I.S. 2017. CrossTalk opposing view: proton transfer in Hv1 utilizes a water wire, and does not require transient protonation of a conserved aspartate in the S1 transmembrane helix, *J Physiol* 595, 6797-6799.

Berger, T.K., Fussholler, D.M., Goodwin, N., Bonigk, W., Muller, A., Dokani Khesroshahi, N., Brenker, C., Wachten, D., Krause, E., Kaupp, U.B., and Strunker, T. 2017. Post-translational cleavage of Hv1 in human sperm tunes pH- and voltage-dependent gating, *J Physiol* 595, 1533-1546.

Berger, T.K., and Isacoff, E.Y. 2011. The pore of the voltage-gated proton channel, *Neuron* 72, 991-1000.

Bezanilla, F. 2000. The voltage sensor in voltage-dependent ion channels, *Physiol Rev* 80, 555-592.

Bezanilla, F. 2018. Gating currents, *J Gen Physiol* 150, 911-932.

Bezanilla, F., Perozo, E., and Stefani, E. 1994. Gating of Shaker K+ channels: II. The components of gating currents and a model of channel activation, *Biophys J* 66, 1011-1021.

Blunck, R., and Batulan, Z. 2012. Mechanism of electromechanical coupling in voltage-gated potassium channels, *Front Pharmacol* 3, 166.

Campbell, D.T., and Hahin, R. 1984. Altered sodium and gating current kinetics in frog skeletal muscle caused by low external pH, *J Gen Physiol* 84, 771-788.

Carbone, E., Fioravanti, R., Prestipino, G., and Wanke, E. 1978. Action of extracellular pH on Na+ and K+ membrane currents in the giant axon of Loligo vulgaris, *J Membr Biol* 43, 295-315.

Carbone, E., Testa, P.L., and Wanke, E. 1981. Intracellular pH and ionic channels in the Loligo vulgaris giant axon, *Biophys J* 35, 393-413.

Carmona, E.M., Larsson, H.P., Neely, A., Alvarez, O., Latorre, R., and Gonzalez, C. 2018. Gating charge displacement in a monomeric voltage-gated proton (Hv1) channel, *Proceedings of the National Academy of Sciences of the United States of America* 115, 9240-9245.

Carvalho-de-Souza, J.L., and Bezanilla, F. 2019. Noncanonical mechanism of voltage sensor coupling to pore revealed by tandem dimers of Shaker, *Nat Commun* 10, 3584.

Catterall, W.A. 1995. Structure and function of voltage-gated ion channels, *Annu Rev Biochem* 64, 493-531.

Chamberlin, A., Qiu, F., Wang, Y., Noskov, S.Y., and Larsson, H.P. 2015. Mapping the gating and permeation pathways in the voltage-gated proton channel Hv1, *J Mol Biol* 427, 131-145.

Chen, X.H., Bezprozvanny, I., and Tsien, R.W. 1996. Molecular basis of proton block of L-type Ca2+ channels, *J Gen Physiol* 108, 363-374.

Cherny, V.V., Markin, V.S., and DeCoursey, T.E. 1995. The voltage-activated hydrogen ion conductance in rat alveolar epithelial cells is determined by the pH gradient, *J Gen Physiol* 105, 861-896.

Cherny, V.V., Morgan, D., Musset, B., Chaves, G., Smith, S.M., and DeCoursey, T.E. 2015. Tryptophan 207 is crucial to the unique properties of the human voltage-gated proton channel, hHV1, *J Gen Physiol* 146, 343-356.

Cherny, V.V., Morgan, D., Thomas, S., Smith, S.M.E., and DeCoursey, T.E. 2018. Histidine(168) is crucial for DeltapH-dependent gating of the human voltage-gated proton channel, hHV1, *J Gen Physiol* 150, 851-862.

Cherny, V.V., Murphy, R., Sokolov, V., Levis, R.A., and DeCoursey, T.E. 2003. Properties of single voltage-gated proton channels in human eosinophils estimated by noise analysis and by direct measurement, *J Gen Physiol* 121, 615-628.

Chowdhury, S., and Chanda, B. 2012. Estimating the voltage-dependent free energy change of ion channels using the median voltage for activation, *J Gen Physiol* 139, 3-17.

Chowdhury, S., Haehnel, B.M., and Chanda, B. 2014. Interfacial gating triad is crucial for electromechanical transduction in voltage-activated potassium channels, *J Gen Physiol* 144, 457-467.

Claydon, T.W., Boyett, M.R., Sivaprasadarao, A., Ishii, K., Owen, J.M., O'Beirne, H.A., Leach, R., Komukai, K., and Orchard, C.H. 2000. Inhibition of the K+ channel kv1.4 by acidosis: protonation of an extracellular histidine slows the recovery from N-type inactivation, *J Physiol* 526 Pt 2, 253-264.

Claydon, T.W., Boyett, M.R., Sivaprasadarao, A., and Orchard, C.H. 2002. Two pore residues mediate acidosis-induced enhancement of C-type inactivation of the Kv1.4 K(+) channel, *Am J Physiol Cell Physiol* 283, C1114-1121.

Claydon, T.W., Vaid, M., Rezazadeh, S., Kwan, D.C., Kehl, S.J., and Fedida, D. 2007. A direct demonstration of closed-state inactivation of K+ channels at low pH, *J Gen Physiol* 129, 437-455.

Cukierman, S., Zinkand, W.C., French, R.J., and Krueger, B.K. 1988. Effects of membrane surface charge and calcium on the gating of rat brain sodium channels in planar bilayers, *J Gen Physiol* 92, 431-447.

DeCoursey, T.E. 2017. CrossTalk proposal: Proton permeation through HV 1 requires transient protonation of a conserved aspartate in the S1 transmembrane helix, *J Physiol* 595, 6793-6795.

DeCoursey, T.E. 2018. Voltage and pH sensing by the voltage-gated proton channel, HV1, *J R Soc Interface* 15.

DeCoursey, T.E., and Cherny, V.V. 1997. Deuterium isotope effects on permeation and gating of proton channels in rat alveolar epithelium, *J Gen Physiol* 109, 415-434.

DeCoursey, T.E., and Cherny, V.V. 1998. Temperature dependence of voltage-gated H+ currents in human neutrophils, rat alveolar epithelial cells, and mammalian phagocytes, *J Gen Physiol* 112, 503-522.

Deutsch, C., and Lee, S.C. 1989. Modulation of K+ currents in human lymphocytes by pH, *J Physiol* 413, 399-413.

Ehrenstein, G., and Fishman, H.M. 1971. Evidence against hydrogen-calcium competition model for activation of electrically excitable membranes, *Nat New Biol* 233, 16-17.

Fernandez-Marino, A.I., Harpole, T.J., Oelstrom, K., Delemotte, L., and Chanda, B. 2018. Gating interaction maps reveal a noncanonical electromechanical coupling mode in the Shaker K(+) channel, *Nat Struct Mol Biol* 25, 320-326.

Frankenhaeuser, B., and Hodgkin, A.L. 1957. The action of calcium on the electrical properties of squid axons, *J Physiol* 137, 218-244.

Fujiwara, Y., Kurokawa, T., Takeshita, K., Kobayashi, M., Okochi, Y., Nakagawa, A., and Okamura, Y. 2012. The cytoplasmic coiled-coil mediates cooperative gating temperature sensitivity in the voltage-gated H(+) channel Hv1, *Nat Commun* 3, 816.

Gilbert, D.L., and Ehrenstein, G. 1970. Use of a fixed charge model to determine the pK of the negative sites on the external membrane surface, *J Gen Physiol* 55, 822-825.

Gilly, W.F., and Armstrong, C.M. 1982a. Divalent cations and the activation kinetics of potassium channels in squid giant axons, *J Gen Physiol* 79, 965-996.

Gilly, W.F., and Armstrong, C.M. 1982b. Slowing of sodium channel opening kinetics in squid axon by extracellular zinc, *J Gen Physiol* 79, 935-964.

Gonzalez, C., Koch, H.P., Drum, B.M., and Larsson, H.P. 2010. Strong cooperativity between subunits in voltage-gated proton channels, *Nat Struct Mol Biol* 17, 51-56.

Gonzalez, C., Morera, F.J., Rosenmann, E., Alvarez, O., and Latorre, R. 2005. S3b amino acid residues do not shuttle across the bilayer in voltage-dependent Shaker K+ channels, *Proceedings of the National Academy of Sciences of the United States of America* 102, 5020-5025.

Gonzalez, C., Rebolledo, S., Perez, M.E., and Larsson, H.P. 2013. Molecular mechanism of voltage sensing in voltage-gated proton channels, *J Gen Physiol* 141, 275-285.

Gonzalez, C., Rosenman, E., Bezanilla, F., Alvarez, O., and Latorre, R. 2000. Modulation of the Shaker K(+) channel gating kinetics by the S3-S4 linker, *J Gen Physiol* 115, 193-208.

Gonzalez, C., Rosenman, E., Bezanilla, F., Alvarez, O., and Latorre, R. 2001. Periodic perturbations in Shaker K+ channel gating kinetics by deletions in the S3-S4

linker, *Proceedings of the National Academy of Sciences of the United States of America* 98, 9617-9623.

Hahin, R., and Campbell, D.T. 1983. Simple shifts in the voltage dependence of sodium channel gating caused by divalent cations, *J Gen Physiol* 82, 785-805.

Hedrich, R., Moran, O., Conti, F., Busch, H., Becker, D., Gambale, F., Dreyer, I., Kuch, A., Neuwinger, K., and Palme, K. 1995. Inward rectifier potassium channels in plants differ from their animal counterparts in response to voltage and channel modulators, *Eur Biophys J* 24, 107-115.

Hille, B. 1968. Charges and potentials at the nerve surface. Divalent ions and pH, *J Gen Physiol* 51, 221-236.

Hille, B. 2001. Ionic Channels of Excitable Membranes Sunderland, Massachusetts, U.S.A., Sinauer Associates.

Hille, B., Woodhull, A.M., and Shapiro, B.I. 1975. Negative surface charge near sodium channels of nerve: divalent ions, monovalent ions, and pH, *Philos Trans R Soc Lond B Biol Sci* 270, 301-318.

Hoshi, T., Zagotta, W.N., and Aldrich, R.W. 1990. Biophysical and molecular mechanisms of Shaker potassium channel inactivation, *Science* 250, 533-538.

Hoshi, T., Zagotta, W.N., and Aldrich, R.W. 1994. Shaker potassium channel gating. I: Transitions near the open state, *J Gen Physiol* 103, 249-278.

Hoth, S., Dreyer, I., Dietrich, P., Becker, D., Muller-Rober, B., and Hedrich, R. 1997. Molecular basis of plant-specific acid activation of K+ uptake channels, *Proceedings of the National Academy of Sciences of the United States of America* 94, 4806-4810.

Iijima, T., Ciani, S., and Hagiwara, S. 1986. Effects of the external pH on Ca channels: experimental studies and theoretical considerations using a two-site, two-ion model, *Proceedings of the National Academy of Sciences of the United States of America* 83, 654-658.

Ishii, K., Nunoki, K., Yamagishi, T., Okada, H., and Taira, N. 2001. Differential sensitivity of Kv1.4, Kv1.2, and their tandem channel to acidic pH: involvement of a histidine residue in high sensitivity to acidic pH, *J Pharmacol Exp Ther* 296, 405-411.

Jones, D.K., Peters, C.H., Allard, C.R., Claydon, T.W., and Ruben, P.C. 2013. Proton sensors in the pore domain of the cardiac voltage-gated sodium channel, *J Biol Chem* 288, 4782-4791.

Kehl, S.J., Eduljee, C., Kwan, D.C., Zhang, S., and Fedida, D. 2002. Molecular determinants of the inhibition of human Kv1.5 potassium currents by external protons and Zn(2+), *J Physiol* 541, 9-24.

Keynes, R.D., and Rojas, E. 1973. Characteristics of the sodium gating current in the squid giant axon, *J Physiol* 233, 28P-30P.

Khan, A., Romantseva, L., Lam, A., Lipkind, G., and Fozzard, H.A. 2002. Role of outer ring carboxylates of the rat skeletal muscle sodium channel pore in proton block, *J Physiol* 543, 71-84.

Klockner, U., and Isenberg, G. 1994. Calcium channel current of vascular smooth muscle cells: extracellular protons modulate gating and single channel conductance, *J Gen Physiol* 103, 665-678.

Koch, H.P., Kurokawa, T., Okochi, Y., Sasaki, M., Okamura, Y., and Larsson, H.P. 2008. Multimeric nature of voltage-gated proton channels, *Proceedings of the National Academy of Sciences* 105, 9111-9116.

Krafte, D.S., and Kass, R.S. 1988. Hydrogen ion modulation of Ca channel current in cardiac ventricular cells. Evidence for multiple mechanisms, *J Gen Physiol* 91, 641-657.

Kuno, M., Ando, H., Morihata, H., Sakai, H., Mori, H., Sawada, M., and Oiki, S. 2009. Temperature dependence of proton permeation through a voltage-gated proton channel, *J Gen Physiol* 134, 191-205.

Kwan, D.C., Fedida, D., and Kehl, S.J. 2006. Single channel analysis reveals different modes of Kv1.5 gating behavior regulated by changes of external pH, *Biophys J* 90, 1212-1222.

Larsson, H.P., Baker, O.S., Dhillon, D.S., and Isacoff, E.Y. 1996. Transmembrane movement of the shaker K+ channel S4, *Neuron* 16, 387-397.

Li, S.J., Zhao, Q., Zhou, Q., Unno, H., Zhai, Y., and Sun, F. 2010. The role and structure of the carboxyl-terminal domain of the human voltage-gated proton channel Hv1, *J Biol Chem* 285, 12047-12054.

MacKinnon, R., Latorre, R., and Miller, C. 1989. Role of surface electrostatics in the operation of a high-conductance Ca2+-activated K+ channel, *Biochemistry* 28, 8092-8099.

Moczydlowski, E., Alvarez, O., Vergara, C., and Latorre, R. 1985. Effect of phospholipid surface charge on the conductance and gating of a Ca2+-activated K+ channel in planar lipid bilayers, *J Membr Biol* 83, 273-282.

Mony, L., Berger, T.K., and Isacoff, E.Y. 2015. A specialized molecular motion opens the Hv1 voltage-gated proton channel, *Nat Struct Mol Biol* 22, 283-290.

Mozhayeva, G.N., and Naumov, A.P. 1970. Effect of surface charge on the steady-state potassium conductance of nodal membrane, *Nature* 228, 164-165.

Muroi, Y., Arcisio-Miranda, M., Chowdhury, S., and Chanda, B. 2010. Molecular determinants of coupling between the domain III voltage sensor and pore of a sodium channel, *Nat Struct Mol Biol* 17, 230-237.

Musset, B., Smith, S.M., Rajan, S., Morgan, D., Cherny, V.V., and Decoursey, T.E. 2011. Aspartate 112 is the selectivity filter of the human voltage-gated proton channel, *Nature* 480, 273-277.

Noda, M., Shimizu, S., Tanabe, T., Takai, T., Kayano, T., Ikeda, T., Takahashi, H., Nakayama, H., Kanaoka, Y., Minamino, N., and et al. 1984. Primary structure of Electrophorus electricus sodium channel deduced from cDNA sequence, *Nature* 312, 121-127.

Nonner, W., Spalding, B.C., and Hille, B. 1980. Low intracellular pH and chemical agents slow inactivation gating in sodium channels of muscle, *Nature* 284, 360-363.

Perozo, E., MacKinnon, R., Bezanilla, F., and Stefani, E. 1993. Gating currents from a nonconducting mutant reveal open-closed conformations in Shaker K+ channels, *Neuron* 11, 353-358.

Perozo, E., Papazian, D.M., Stefani, E., and Bezanilla, F. 1992. Gating currents in Shaker K+ channels. Implications for activation and inactivation models, *Biophys J* 62, 160-168; discussion 169-171.

Perozo, E., Santacruz-Toloza, L., Stefani, E., Bezanilla, F., and Papazian, D.M. 1994. S4 mutations alter gating currents of Shaker K channels, *Biophys J* 66, 345-354.

Pietrobon, D., Prod'hom, B., and Hess, P. 1989. Interactions of protons with single open L-type calcium channels. pH dependence of proton-induced current fluctuations with Cs+, K+, and Na+ as permeant ions, *J Gen Physiol* 94, 1-21.

Prod'hom, B., Pietrobon, D., and Hess, P. 1987. Direct measurement of proton transfer rates to a group controlling the dihydropyridine-sensitive Ca2+ channel, *Nature* 329, 243-246.

Prod'hom, B., Pietrobon, D., and Hess, P. 1989. Interactions of protons with single open L-type calcium channels. Location of protonation site and dependence of proton-induced current fluctuations on concentration and species of permeant ion, *J Gen Physiol* 94, 23-42.

Prole, D.L., Lima, P.A., and Marrion, N.V. 2003. Mechanisms underlying modulation of neuronal KCNQ2/KCNQ3 potassium channels by extracellular protons, *J Gen Physiol* 122, 775-793.

Qiu, F., Chamberlin, A., Watkins, B.M., Ionescu, A., Perez, M.E., Barro-Soria, R., Gonzalez, C., Noskov, S.Y., and Larsson, H.P. 2016. Molecular mechanism of Zn2+ inhibition of a voltage-gated proton channel, *Proceedings of the National Academy of Sciences of the United States of America* 113, E5962-E5971.

Qiu, F., Rebolledo, S., Gonzalez, C., and Larsson, H.P. 2013. Subunit interactions during cooperative opening of voltage-gated proton channels, *Neuron* 77, 288-298.

Ramsey, I.S., Mokrab, Y., Carvacho, I., Sands, Z.A., Sansom, M.S.P., and Clapham, D.E. 2010. An aqueous H+ permeation pathway in the voltage-gated proton channel Hv1, *Nat Struct Mol Biol* 17, 869-875.

Ramsey, I.S., Moran, M.M., Chong, J.A., and Clapham, D.E. 2006. A voltage-gated proton-selective channel lacking the pore domain, *Nature* 440, 1213-1216.

Sasaki, M., Takagi, M., and Okamura, Y. 2006. A voltage sensor-domain protein is a voltage-gated proton channel, *Science* 312, 589-592.

Schauf, C.L., and Davis, F.A. 1976. Sensitivity of the sodium and potassium channels of Myxicola giant axons to changes in external pH, *J Gen Physiol* 67, 185-195.

Shrager, P. 1974. Ionic conductance changes in voltage clamped crayfish axons at low pH, *J Gen Physiol* 64, 666-690.

Starkus, J.G., Varga, Z., Schonherr, R., and Heinemann, S.H. 2003. Mechanisms of the inhibition of Shaker potassium channels by protons, *Pflugers Arch* 447, 44-54.

Stefani, E., Toro, L., Perozo, E., and Bezanilla, F. 1994. Gating of Shaker K+ channels: I. Ionic and gating currents, *Biophys J* 66, 996-1010.

Steidl, J.V., and Yool, A.J. 1999. Differential sensitivity of voltage-gated potassium channels Kv1.5 and Kv1.2 to acidic pH and molecular identification of pH sensor, *Mol Pharmacol* 55, 812-820.

Takeshita, K., Sakata, S., Yamashita, E., Fujiwara, Y., Kawanabe, A., Kurokawa, T., Okochi, Y., Matsuda, M., Narita, H., Okamura, Y., and Nakagawa, A. 2014. X-ray crystal structure of voltage-gated proton channel, *Nat Struct Mol Biol* 21, 352-357.

Tanabe, T., Takeshima, H., Mikami, A., Flockerzi, V., Takahashi, H., Kangawa, K., Kojima, M., Matsuo, H., Hirose, T., and Numa, S. 1987. Primary structure of the receptor for calcium channel blockers from skeletal muscle, *Nature* 328, 313-318.

Tempel, B.L., Papazian, D.M., Schwarz, T.L., Jan, Y.N., and Jan, L.Y. 1987. Sequence of a probable potassium channel component encoded at Shaker locus of Drosophila, *Science* 237, 770-775.

Tombola, F., Ulbrich, M.H., Kohout, S.C., and Isacoff, E.Y. 2010. The opening of the two pores of the Hv1 voltage-gated proton channel is tuned by cooperativity, *Nat Struct Mol Biol* 17, 44-50.

Trapani, J.G., and Korn, S.J. 2003. Effect of external pH on activation of the Kv1.5 potassium channel, *Biophys J* 84, 195-204.

Voet, D., and Voet, J.G. 2010. Biochemistry, 4th Edition, W. Ross MacDonald School Resource Services Library.

Yellen, G., Jurman, M.E., Abramson, T., and MacKinnon, R. 1991. Mutations affecting internal TEA blockade identify the probable pore-forming region of a K+ channel, *Science* 251, 939-942.

Zagotta, W.N., Hoshi, T., and Aldrich, R.W. 1994a. Shaker potassium channel gating. III: Evaluation of kinetic models for activation, *J Gen Physiol* 103, 321-362.

Zagotta, W.N., Hoshi, T., Dittman, J., and Aldrich, R.W. 1994b. Shaker potassium channel gating. II: Transitions in the activation pathway, *J Gen Physiol* 103, 279-319.

Zhang, J.F., and Siegelbaum, S.A. 1991. Effects of external protons on single cardiac sodium channels from guinea pig ventricular myocytes, *J Gen Physiol* 98, 1065-1083.

Zhang, S., Kurata, H.T., Kehl, S.J., and Fedida, D. 2003. Rapid induction of P/C-type inactivation is the mechanism for acid-induced K+ current inhibition, *J Gen Physiol* 121, 215-225.

Zhou, Y., Xia, X.M., and Lingle, C.J. 2018. BK channel inhibition by strong extracellular acidification, *Elife* 7.

PUBLICATIONS

Thesis-related publications

Carmona, E. M., Fernandez, M., Larsson, H. P., Neely, A., Alvarez, O., Latorre, R., & Gonzalez, C. (2020). The pH modulation of the voltage sensor in the voltage-gated proton channel (Hv1). In preparation.

Carmona, E. M., Alvarez, O., Neely, A., Latorre, R., & Gonzalez, C. (2019). pH Dependence of a Monomeric Non-Conducting Voltage-Gated Proton Channel (Hv1). *Biophysical Journal*, 116(3), 302a.

Osvaldo Alvarez, **Emerson Carmona**, Ramon Latorre & Carlos Gonzalez. (2018). A Glimpse into the Permeation Pathway of the Voltage-Dependent Proton Channel (Hv1). Comments on CrossTalk 33: Proton permeation through HV1 requires/does not require transient protonation of a conserved aspartate in the S1 transmembrane helix. *Journal of Physiology*.

Carmona, E. M., Larsson, H. P., Neely, A., Alvarez, O., Latorre, R., & Gonzalez, C. (2018). Gating charge displacement in a monomeric voltage-gated proton (Hv1) channel. *Proceedings of the National Academy of Sciences*, 115(37), 9240-9245.

Carmona, E.M., Baez-Nieto, D., Pupo, A., Castillo, K., Alvarez, O., Neely, A., Latorre R., Gonzalez, C. (2018). Properties of the Voltage-Gated Proton Channel Gating Currents. *Biophysical Journal*, 114(3), 546a.

Other publications

Granados, S. T., Castillo, K., Bravo-Moraga, F., Sepúlveda, R. V., Carrasquel-Ursulaez, W., Rojas, M., **Carmona, E.**, Lorenzo-Ceballos, Y., González-Nilo, F., González, C., Latorre, R., & Torres, Y.P. (2019). The molecular nature of the 17β-Estradiol binding site in the voltage-and Ca 2+-activated K+(BK) channel β1 subunit. *Scientific reports*, 9(1), 9965.

Alvarez O., Castillo K., **Carmona E.**, Gonzalez C., Latorre R. (2019). Methods for Investigating TRP Channel Gating. In: Ferrer-Montiel A., Hucho T. (eds) TRP Channels. *Methods in Molecular Biology*, vol 1987. Humana, New York, NY.

Gating charge displacement in a monomeric voltage-gated proton (H_v1) channel

Emerson M. Carmona[a], H. Peter Larsson[b], Alan Neely[a], Osvaldo Alvarez[a,c], Ramon Latorre[a,1], and Carlos Gonzalez[a,1]

[a]Centro Interdisciplinario de Neurociencia de Valparaíso, Universidad de Valparaíso, 2351319 Valparaíso, Chile; [b]Department of Physiology and Biophysics, University of Miami, Miami, FL 33136; and [c]Departamento de Biología, Facultad de Ciencias, Universidad de Chile, 7800003 Santiago, Chile

Contributed by Ramon Latorre, July 18, 2018 (sent for review June 6, 2018; reviewed by Thomas E. DeCoursey and Francesco Tombola)

The voltage-gated proton (H_v1) channel, a voltage sensor and a conductive pore contained in one structural module, plays important roles in many physiological processes. Voltage sensor movements can be directly detected by measuring gating currents, and a detailed characterization of H_v1 charge displacements during channel activation can help to understand the function of this channel. We succeeded in detecting gating currents in the monomeric form of the *Ciona*-H_v1 channel. To decrease proton currents and better separate gating currents from ion currents, we used the low-conducting H_v1 mutant N264R. Isolated ON-gating currents decayed at increasing rates with increasing membrane depolarization, and the amount of gating charges displaced saturates at high voltages. These are two hallmarks of currents arising from the movement of charged elements within the boundaries of the cell membrane. The kinetic analysis of gating currents revealed a complex time course of the ON-gating current characterized by two peaks and a marked Cole–Moore effect. Both features argue that the voltage sensor undergoes several voltage-dependent conformational changes during activation. However, most of the charge is displaced in a single central transition. Upon voltage sensor activation, the charge is trapped, and only a fast component that carries a small percentage of the total charge is observed in the OFF. We hypothesize that trapping is due to the presence of the arginine side chain in position 264, which acts as a blocking ion. We conclude that the movement of the voltage sensor must proceed through at least five states to account for our experimental data satisfactorily.

Hv1 proton channel | gating currents | trapping | voltage sensor | kinetic model

Voltage-gated proton (H_v1) channels are transmembrane proteins that regulate cellular pH, producing outward proton currents in response to depolarization. Since the discovery of the *Ciona intestinalis*, mouse, and human H_v1 genes in 2006 (1, 2), the relevance of this channel in physiological and pathophysiological processes has increased continuously (3). H_v1 is a voltage-gated ion channel with a unique structure and properties. It is a homodimer (4–6) containing four transmembrane alpha helixes in each subunit (S1 to S4). Both the voltage sensor and the permeation pathway of this channel originate from these four transmembrane segments. The fourth transmembrane helix (S4) contains three conserved arginine residues responsible for the channel voltage sensitivity (7, 8) The intracellular N-terminal domain is variable in both length and sequence among different species. The intracellular C-terminal domain forms a coiled-coil structure necessary for dimer formation (6). H_v1 is voltage- (7) and pH-dependent (9), is highly selective to protons (10), has a small unitary conductance (11), and displays a cooperative gating between subunits (8, 12). However, there are still many open questions regarding the mechanisms of H_v1 activation. In particular, we do not know the details regarding how the gating charges are displaced during activation and how these movements are related to channel opening.

H_v1 voltage sensor movement has been studied principally by two methods: accessibility assays and fluorescence. In the first case, membrane-impermeable thiol-reactive methanethiosulfonate (MTS) probes were used to test the state-dependent accessibility of a cysteine residue introduced into a specific region of the voltage sensor (13). In the case of H_v1, accessibility experiments indicate that both S1 (14) and S4 (7) undergo conformational changes during activation and that there is cooperativity between the subunits of the channel (8). The second approach involves the use of voltage-clamp fluorometry (VCF) (15). In VCF, the conformational changes of the channel are monitored by a fluorescent probe bound to a cysteine introduced into a specific site using mutagenesis (16, 17). VCF experiments revealed two conformational changes during activation (18); following the S4 movement, there is a displacement of S1 associated with the opening of the channel (14). The caveat of these methodologies is that they are indirect approaches to studying the dynamics of the H_v1 voltage sensor. In contrast, gating currents directly report the movement of the voltage-sensing charges across the membrane electric field, making it possible to study the kinetics of this process in detail.

In the *Shaker* voltage-gated potassium channel, gating currents are produced by the movement of arginine residues in the S4 transmembrane segment within the voltage sensor domain (19, 20). Three of these arginine residues are conserved in S4 of H_v1 and were shown to be responsible for the voltage-dependent gating of the channel (7). Since the *Ciona*-H_v1 channels express well in oocytes, it should be possible to record gating currents induced by the activation of this channel. Indeed, preliminary studies on H_v1 gating current have been reported (21–23).

Significance

H_v1 proton channels, since their open probability increases with depolarization and low pH, are fundamental in sustaining the suitable pH gradient for cell survival. Here, we have characterized the gating current elicited by the monomeric mutant proton channel N264R with the aim of understanding the voltage-dependent processes that control channel opening. Gating currents precede ion currents, indicating that a large fraction of gating charge is displaced before H_v1 opening. The voltage sensor displacements are complex and consist of numerous well-defined states. However, most of the charge is displaced in a single transition that probably leads to channel opening. The positively charged arginine in the N264R channel promotes gating charge trapping in addition to blocking the proton currents.

Author contributions: E.M.C., H.P.L., A.N., O.A., R.L., and C.G. designed research; E.M.C. performed research; E.M.C., H.P.L., A.N., O.A., R.L., and C.G. analyzed data; and E.M.C., H.P.L., A.N., O.A., R.L., and C.G. wrote the paper.

Reviewers: T.E.D., Rush University; and F.T., University of California, Irvine.

The authors declare no conflict of interest.

[1]To whom correspondence may be addressed. Email: ramon.latorre@uv.cl or carlos.gonzalezl@uv.cl.

This article contains supporting information online at www.pnas.org/lookup/suppl/doi:10.1073/pnas.1809705115/-/DCSupplemental.

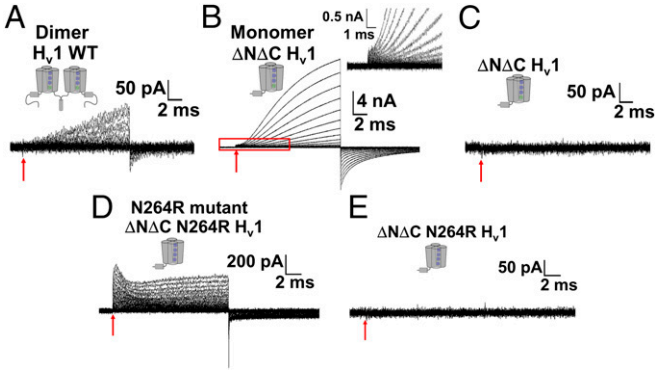

Fig. 1. An early nonlinear capacitive current was detected in the monomeric H_v1. (*A*) Currents produced by the dimeric H_v1 did not show an initial nonlinear capacitive component. (*B*) Currents produced by the monomeric form of the channel presented an initial step (*Inset*) preceding the development of fast proton currents. (*C*) A hyperpolarizing protocol applied to patches expressing the monomeric H_v1 did not produce similar currents. (*D*) Currents produced by the conductance-impaired monomeric H_v1 mutant N264R presented an initial nonlinear transient current followed by the development of proton currents. (*E*) A hyperpolarizing protocol applied to patches expressing the monomeric H_v1 mutant N264R did not produce currents. Superimposed current traces were recorded for membrane voltage steps from −90 to 200 mV in 10-mV increments in *A* and *B*, from −90 to 260 mV in 10-mV increments in *D*, and from −330 to −50 mV in 10-mV increments in *C* and *E*. Red arrows indicate the time at which the voltage pulses were applied. Holding potential was −70 mV. Linear capacitive current was subtracted online using a P/-8 pulse protocol.

Results

H_v1 Gating Currents Are Revealed in Monomeric Channels and Better Resolved in Conductance-Impaired N264R Mutant. To detect H_v1 gating currents, we expressed *C. intestinalis* H_v1 channels in *Xenopus laevis* oocytes and recorded membrane currents in giant patches (inside-out configuration and symmetrical pH = 7.0). In dimeric H_v1, we were unable to resolve any initial transient current consistent with nonlinear capacitive currents. At short times after the onset of the depolarizing pulse, we observed a monotonic development of current free of any transient component (Fig. 1*A*). In contrast, upon depolarization, oocyte membrane patches expressing fast activating monomeric channels displayed an initial current transient that preceded the development of ion currents (Fig. 1*B*). As expected for gating currents, these initial transient currents were absent during hyperpolarizing pulses (Fig. 1*C*). We conclude that our failure to detect gating currents in the dimeric H_v1 channels was because of their slow kinetics and small amplitude.

Since ion currents heavily contaminate the putative gating currents from monomeric H_v1, we resorted to the N264R mutant of monomeric H_v1 that greatly decreases proton currents while retaining voltage sensor movement as assayed by indirect methods (18, 24). At depolarizing voltages, currents recorded from this mutant channel showed an early transient current followed by increasing outward currents (Fig. 1*D*). During repolarization, we could distinguish a rapid transient current, followed by a nearly constant component. Most likely, the transient component is gating charge movement, and the slow component is a mix of ion and gating current (Fig. 1*D*). To corroborate that the ON-transient was due to nonlinear charge movement, we also show that hyperpolarization-evoked currents lack this component (Fig. 1*E*). The following analysis will demonstrate that the early currents in Fig. 1*D* are indeed gating currents.

H_v1 Gating Currents Can Be Isolated from Ion Currents. Isolation of the ON-gating currents was performed numerically, assuming that the currents recorded from monomeric H_v1 mutant (I_{exp}) were the sum of gating (I_g) and ion currents (I_i) (21):

$$I_{exp}(t) = I_g(t) + I_i(t). \quad [1]$$

Gating currents were modeled as a product of an increasing and a decreasing exponential function, corresponding to the rising and decaying phase of the gating currents, respectively:

$$I_g(t) = A\left(1 - e^{-t/\tau_1}\right)e^{-t/\tau_2}, \quad [2]$$

where A is the amplitude and τ_1 and τ_2 are the time constants of the increasing and the decreasing exponential functions, respectively. Ion currents were modeled as an exponential function raised to the power of two with a time constant τ_3, that accounts for the sigmoidal shape of macroscopic current time course from mutant monomeric H_v1 (Fig. 1*B*):

$$I_i(t) = B\left(1 - e^{-t/\tau_3}\right)^2, \quad [3]$$

where B is the amplitude of the ion current component. Fig. 2*A* shows examples of the fitting procedure of the current records at six different voltages. Plots of the isolated gating currents $I_g(t)$ show that both the amplitude and the rate of decay increase with voltage as expected from bona fide gating currents (Fig. 2*B*). The time course of the charge displaced, obtained by integrating $I_g(t)$, is shown in Fig. 2*C*. The time constant of the gating current decay (τ_2) (Eq. **2**) vs. voltage data was fitted assuming that the conformational change of the voltage sensor is well-described by a first-order process: resting-active (A-B) (Fig. 2*D*, open circles). In the A-B two-state model, voltage-dependent time constants and rates are given by the equations

$$\tau(V) = \frac{1}{\alpha(V) + \beta(V)}, \alpha(V) = \alpha_0 e^{\frac{z\delta_\alpha e_0 V}{kT}}, \beta(V) = \beta_0 e^{\frac{-z\delta_\beta e_0 V}{kT}}, \quad [4]$$

where α(V) and β(V) are the forward and backward rates, respectively, and α_0 and β_0 are the rate constants for $V = 0$ mV, $z\delta_\alpha$

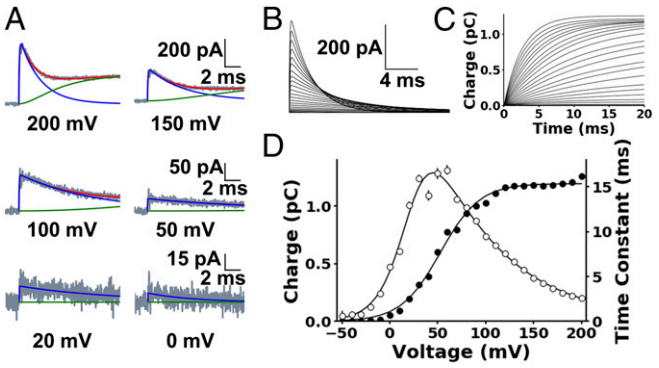

Fig. 2. Isolated ON-gating currents were voltage-dependent. (*A*) Representative experimental currents recorded for the monomeric H_v1 mutant N264R during depolarizations at the indicated voltages (I_{exp}, black traces). They were fitted with Eq. **1** to isolate the ON-gating current (I_g, blue traces) from the ion current (I_i, green traces). Holding potential was −70 mV. (*B*) Superimposed plots of the isolated ON-gating currents for membrane voltage steps from −90 to 200 mV in 10-mV increments. (*C*) Time course of the gating charge displaced obtained integrating the gating currents shown in *B*. (*D*) Time constants of the I_g decay (open circles) and charge displaced as function of voltage [*Q*(*V*) curve, filled circles]. Time constant data were fitted using a two-state model (solid line), where $\alpha_0 = 0.027 \pm 0.002$ ms^{-1}, $\beta_0 = 1.53 \pm 0.01$ ms^{-1}, $z\delta_\alpha = 0.34 \pm 0.02$, and $z\delta_\beta = 1.44 \pm 0.12$. The *Q*(*V*) curve was fitted by a Boltzmann function (solid line, Eq. **5**), where $V_{0.5} = 52.8 \pm 1.1$ mV and $z\delta = 1.23 \pm 0.06$. Error bars are the SD of the parameters obtained in the fitting procedure. The average values of the *Q*(*V*) parameters ($n = 10$) were as follows: $z\delta = 1.05 \pm 0.09$ and $V_{0.5} = 54.8 \pm 7.9$ mV.

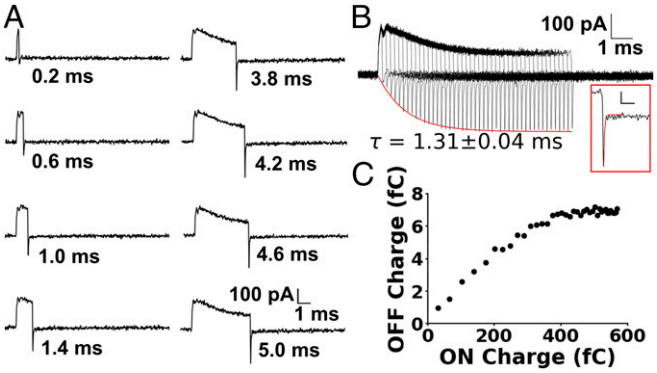

Fig. 3. Gating charge is trapped during voltage sensor activation. (*A*) Currents recorded for a series of depolarizations with different durations. The protocol consisted of a prepulse voltage of −70 mV, followed by a test pulse to 150 mV and repolarization to 0 mV (reversal potential). Depolarization was imposed during the time indicated for each trace. (*B*) Superimposed series of current records produced by short depolarizations from a prepulse voltage of −70 mV, depolarization to 150 mV, and a repolarization to 0 mV. Each trace is separated from the following by a 0.2-ms time increment. The time course of the fast component is described by the red line. (*Inset*) OFF-gating current is well-described by a single exponential of 0.03 ms (red trace). (Scale bars: 50 pA and 0.4 ms.) (*C*) OFF-gating charge as a function of the ON-gating charge for pulses of different durations. OFF charge was calculated multiplying the amplitude of the current by the time constant of decay (0.03 ms) while ON charge was integrated numerically, using the time constant at 150 mV (see text).

and $z\delta_\beta$ describe the voltage dependence of the rates, e_0 is the elementary charge, and k and T have their usual meanings. The parameters that best described the data shown were $\alpha_0 = 0.027 \pm 0.002$ ms^{-1}, $\beta_0 = 1.53 \pm 0.01$ ms^{-1}, $z\delta_\alpha = 0.34 \pm 0.02$, and $z\delta_\beta = 1.44 \pm 0.12$ (Fig. 2*D*, solid line). β(V) is more voltage-dependent than α(V), and, as a result, the bell-shaped time constant vs. voltage plot is asymmetric (Fig. 2*D*).

Charge displaced at each voltage was obtained from the area under the corresponding isolated gating current: i.e., A times τ_2, (Eq. **2** and Fig. 2*D*, filled circles). This $Q(V)$ curve showed a voltage-dependent saturation and was well-fitted using a Boltzmann function:

$$Q(V) = \frac{Q_{max}}{1 + e^{\frac{-z\delta e_0 (V - V_{0.5})}{kT}}}, \qquad [5]$$

with half-activation voltage ($V_{0.5}$) of 52.8 ± 1.1 mV and effective valence ($z\delta$) of 1.23 ± 0.06 (Fig. 2*D*, solid line). For a set of 10 independent experiments, the average values of the parameters were as follows: $z\delta = 1.05 \pm 0.09$ and $V_{0.5} = 54.8 \pm 7.9$ mV (mean ± SEM).

H_v1 Gating Current Kinetics Revealed That a Large Fraction of the Charge Is Trapped. Fig. 2*A* shows that gating currents precede the development of ion currents, giving us a time window to characterize them in more detail. Accordingly, to minimize the activation of ion currents, we measured the OFF-gating currents after very short depolarizations. Furthermore, after the pulse to 150 mV, the membrane potential was returned to the reversal potential of the proton currents (0 mV). Upon returning to 0 mV, we observed a rapid transient with a 0.03-ms time constant (Fig. 3 *A* and *B*, *Inset*). However, the OFF-gating charges displaced during these brief transients were only a minute fraction of that displaced during the ON. This discrepancy indicates that, while dwelling at 150 mV, a large fraction of the charges became trapped in a deep well. The amplitude of the OFF-gating currents increased with the duration of the depolarizing pulse and reached a plateau following an exponential function with a time constant of 1.31 ± 0.04 ms. (Fig. 3*B*). We computed the charge of OFF transient by multiplying the amplitude of the transient by the decay time constant of the spike (τ = 0.03 ms). The time course of the ON-gating current cannot be calculated directly from the current records due to the ion current contamination. To calculate the ON-gating charge, we integrated the current numerically from the beginning of the depolarizing pulse up to 1 ms. From 1 ms on, we integrated the rest of the charge by multiplying the amplitude of the current at 1 ms by the 4-ms time constant of the gating current decay at 150 mV (Fig. 2*D*). With these ON and OFF charges, we built the graph shown in Fig. 3*C*. For long depolarizing pulses, the OFF/ON charge ratio was 7/500 (or 1.4% of the ON).

Trapped H_v1 Gating Charge Is Recovered During Repolarization. We next designed a protocol to recover the ON-gating charges, consisting of two 20-ms depolarization pulses to 150 mV from a holding potential of −70 mV, separated by a sojourn of increasing duration at −70 mV (Fig. 4 *A* and *B*). If the trapped gating charge returns slowly at −70 mV, the recovered charge can be measured during the second depolarizing pulse. At the onset of the second depolarization, a brief spike was recorded, followed by a pedestal of ion current. The spike only appeared after a brief repolarization period: e.g., 2 ms. This ON spike is the mirror image of the OFF spike seen at the onset of the preceding repolarization. With a longer sojourn at −70 mV (50 ms), the ON spike disappeared, and the gating current reached an amplitude comparable with that of the first 20-ms pulse (Fig. 4 *A* and *B*). The origin of the OFF and ON spikes will be explained with a five-state kinetic model (see below). The amount of charge recovered during the second pulse increased following an exponential time course with a time constant of 87.6 ± 7.4 ms (Fig. 4 *B* and *C*). The charge extrapolated at very long times, Q_∞, was 1,566 ± 80 fC (Fig. 4*C*), which compares

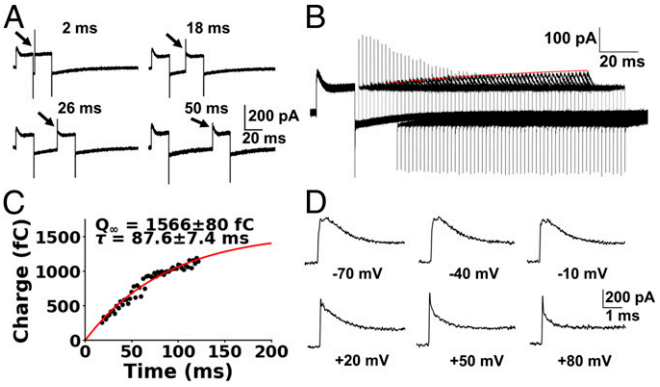

Fig. 4. The OFF-gating charge is recovered slowly. (*A*) ON-gating current recovery protocol for four different times. Two depolarizing pulses from a holding potential of −70 mV to 150 mV were separated by the time indicated. A fast outward gating current appeared at short intervals, and it decreased at longer intervals, while a second slower component appeared at longer intervals (arrows). (*B*) Superimposed currents produced by the ON recovery protocol from a holding potential of −70 mV and depolarization to 150 mV. The interval of time between the depolarizing pulses increased 2 ms between traces. The red line describes the time course of the ON-gating charge recovery. (*C*) The charge displaced during the slow component of the second depolarization as a function of the time interval between the depolarizations. The data were fitted using a single increasing exponential function $Q_\infty[1 - \exp(-t/\tau)]$ where Q_∞ is the exponential amplitude and τ is the time constant. Note that the asymptote of the curve is 1,566 ± 80 fC, meaning that the charge is recovered completely. (*D*) Cole–Moore effect of the ON-gating current when a depolarizing pulse of 200 mV is preceded by the prepulse voltage indicated. Note how the two peaks of current are converted into a single peak of current and the kinetics of decay gets faster as the prepulse voltage becomes more positive.

well with the charge displaced during the ON (1,500 fC). Note that the fast transient current during the ON-gating currents was only present when the repolarization period was short and disappeared at long repolarizations (Fig. 4 *A* and *B*). Moreover, we had consistently observed two peaks and a rising phase in the ON-gating current at 150 mV, when the holding voltages were sufficiently negative (negative voltages in Figs. 3*A* and 4*D*). However, when we increased the holding voltages, only a single peak was detected (positive voltages in Fig. 4*D*). The rate of decay of the gating currents was also affected by the initial conditions, being faster with prepulse voltages above 0 mV (*SI Appendix*, Fig. S1 *A* and *B*). This protocol is equivalent to the well-known Cole–Moore effect (25, 26) and can reveal that the voltage sensor undergoes multiple voltage-dependent transition states (*Discussion*) preceding the voltage sensor activation and channel opening (*SI Appendix*, Fig. S1 *C* and *D*). A Cole–Moore shift in dimeric native H_v1 channels has been reported previously (27). However, our results show that this effect is also present in the monomeric form of the channel, indicating that the monomer also transits through several closed states before channel opening.

Discussion

Gating Current Measurements. The two main difficulties for measuring gating currents in the WT dimeric H_v1 are the slow kinetics of activation (*SI Appendix*, Figs. S2*A* and S3), which possibly is correlated with a slow movement of the voltage sensor, and the inability to eliminate or reduce significantly proton currents through the channels. Here, we used an experimental strategy that enabled us to detect and characterize the H_v1 charge displacement. Since the kinetics of proton currents in the monomeric form of the channel develop much faster than those in the dimer (*SI Appendix*, Figs. S2 and S3), implying a faster increase in the H_v1 voltage-dependent open probability, we expected to find gating currents faster and with larger amplitudes. Also, to minimize the proton currents, we used the monomeric low-conducting mutant N264R (*SI Appendix*, Figs. S2*C* and S3). Notably, the N264R mutant has almost the same voltage dependence as the WT form of H_v1 (*SI Appendix*, Figs. S3 and S4).

Gating currents must obey certain rules demanded by the confined space in which they move. First, the charge versus voltage (Q-V) curve should saturate at high voltages at which all voltage sensors are activated. Second, gating currents should become larger and faster as the voltage is increased: i.e., the gating current kinetics is voltage-dependent (28). Third, all of the charge displaced during the ON must be recovered during the OFF. In the N264R mutant, we isolated the gating currents analytically, and the resulting nonlinear currents displayed kinetics and voltage dependence that satisfied the first two criteria. However, the OFF represented only 1.4% of the ON-gating charges. This phenomenon reminded us of charge immobilization first reported for the sodium channel (29). Here, we prefer to use the concept of trapping since modeling of the gating kinetics data suggests that, upon activation, charge needs to surmount a large barrier to return to its initial configuration (see below).

A Two-State Model Is Not Enough to Recapitulate Gating Charge Displacement in H_v1 Channels. To analyze isolated gating currents, we assumed a two-state model: resting (A)–active (B). However, a closer inspection of the data suggests that the movement of the voltage sensor in monomeric H_v1 is more complex than a two-state process. The first observation that caught our attention was the fact that only a very small fraction of the ON-gating charge was recovered in the OFF (Fig. 3*C*), suggesting that the return of the charge to the resting state is very slow indeed. Actually, the double pulse experiments of Fig. 4 suggest that, to return to the resting state, the voltage sensor needs to undergo at least two transitions: $A \leftrightarrow B_1 \leftrightarrow B_2$, where A is the resting state, and that a large energy barrier separates states A from B_1. The fast transition seen in the OFF is determined by the B_2-to-B_1 transition, and the slow charge return, defined by the 88-ms time constant (Fig. 4*C*), represents the transition from B_1 to A. However, the presence of two peaks in the ON-gating current and the pronounced Cole–Moore effect also suggest that, to reach state B_1, the voltage sensor undergoes first a fast transition defining the first peak A_1-A_2 and a slower transition A_2-A_3 before reaching the B_1 state. Therefore, charge trapping is a consequence of the large energy barrier separating states A_3 from B_1 (see below). Against a two-state model is also the fact that the Boltzmann describing the Q-V curve yields a $z\delta$ close to 1 (Fig. 2), in contrast to the limiting slope experiments that set a lower limit to near three gating charges per monomeric H_v1 channel (8). This discrepancy suggests that there is more than one step involved in the voltage sensor activation (30).

A Five-State Model Reproduced H_v1 Gating Current Features. Taking into account all of the results presented, we propose a sequential model for the movement of the monomeric H_v1 voltage sensor consisting of five states (A_1, A_2, A_3, B_1, and B_2) separated by four transitions (Fig. 5*A* and *SI Appendix*, Fig. S5). States A_1 to A_3 are revealed during H_v1 channel activation (Fig. 4*D* and *SI Appendix*, Fig. S1), and B_1 and B_2 during channel deactivation (Fig. 4 *A* and *B*). Gating currents simulated from our five-state model presented two peaks of currents in the ON and only a fast component in the OFF (Fig. 5*B*), reproducing the experimental currents. Additionally, it can reproduce the transients observed during activation and deactivation and the Cole–Moore effect at different prepulse voltages (Fig. 5 *C*–*E*). Our model shows that the kinetics of the ON-gating current is dominated by the highest energy barrier placed between A_3 and B_1 (32 kJ/mol). Application of a 150-mV

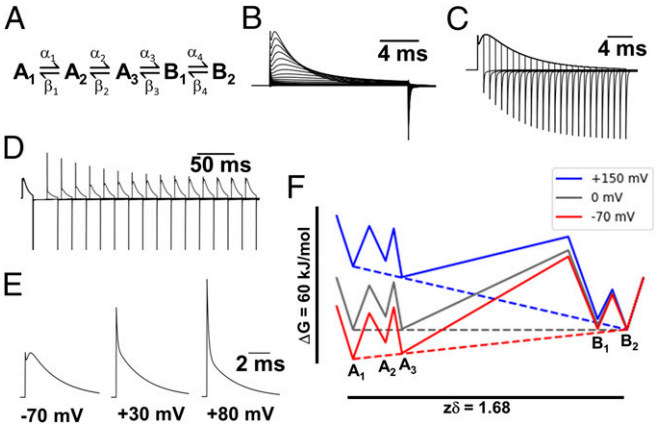

Fig. 5. A five-state model can reproduce the features of the H_v1 gating currents. (*A*) Five-state sequential model used to simulate H_v1 gating currents. Rates and voltage dependence of each transition are given in *SI Appendix*, Table S1. (*B*) Superimposed simulated traces of gating currents produced by the model. A prepulse at −70 mV was followed by a series of voltage steps from −90 to 200 mV in 10-mV increments and repolarization to 0 mV. Note the presence of two peaks during the ON-gating current and the large difference between the gating charge displaced during the ON and OFF components. (*C*) Superimposed simulated traces of depolarizations at 150 mV of increasing duration produced a fast OFF component that increases at short depolarizations to reach a plateau during repolarization at 0 mV, similar to Fig. 3*B*. Holding potential is −70 mV, and the time interval of depolarization increased 1 ms between current traces. (*D*) Superimposed simulated traces of the ON recovery protocol similar to the protocol of Fig. 4*B*. Holding potential is −70 mV, and depolarizations were produced at 150 mV. The time interval between depolarizations increases 20 ms between traces. (*E*) Simulated traces of the ON-gating current produced with a depolarization at 200 mV from a prepulse at the indicated voltage. Note that, similar to the result showed in Fig. 4*D*, the two peaks of current in the ON change to one and the kinetics of decay get faster as the prepulse voltage increases. (*F*) Energy barriers produced by the five-state model at three different voltages.

pulse decreased this energy to 17 kJ/mol, but, upon returning to −70 mV, the charge needed to surmount a 27-kJ/mol barrier height to return from B_1 to the A_3 state (Fig. 5*F*). This activation energy difference predicts an A_3-to-B_1 charge movement at 150 mV to be 27 times faster than the B_1-to-A_3 movement at −70 mV. Our results indicate that the difference between the slow kinetic component of the ON (4 ms) is 22 times faster than the slow OFF component (88 ms) (compare Fig. 2*D* with Fig. 4*C*), which is in reasonable agreement with the calculation using the five-state model.

A New H_v1 Channel Kinetic Model Is Needed. Previously, by a fluorophore attached to the S4 voltage sensor in dimeric H_v1 channels, we revealed two S4 charge movements: The first one precedes channel opening, with S4 charge movements in both subunits independently, and the second one correlates with channel opening, defined as the fluorescence hook (18). To make it compatible with our previous model, only B_2 in the present model would be correlated with an open channel. Then, the hook would be the transition from B_2 to B_1, which is fast and closes the channel, while transition B_1 to A_3 would be the main S4 transition, which is slow. In the kinetic model of dimeric H_v1 proposed by us (18), voltage sensor movement involved three closed and one open state, where the movement of both voltage sensors within the dimer is necessary before the opening of the permeation pathway of each subunit (18). Here, we found that each independent H_v1 voltage sensor transits through different states, suggesting that the movement of charge is more complex than previously thought. The most significative fact is that more than 50% of gating charge displacement, on the monomeric H_v1 channel, occurs before opening (in 5 ms at 150 mV, when the open probability of the monomeric H_v1 channel is only 0.2, 65% of the gating charge has been displaced). Dimer formation confers cooperative gating to H_v1 channels (8). Therefore, it is possible that the displacement of dimeric voltage sensors is different from the monomeric voltage sensors movement.

Molecular Mechanism for Trapping. We envision that the rate-limiting step that keeps the charges from returning to their resting configuration involves a blocked-like phenomenon mediated by the arginine side chain, much like the documented blockade of H_v1 channels by guanidinium reagents (31–33). Moreover, as reported before using the dimeric human H_v1 mutant N214R (34, 35) and mouse mutant N210R (24), we found that the N264R mutant open channel behaves as an inward rectifier (*SI Appendix*, Fig. S6). Blockade by the positively charged arginine located in the internal vestibule of the channel should be relieved by hyperpolarizing voltages, and the mutant channel should behave as an inward rectifier as found experimentally (*SI Appendix*, Fig. S6). We should also consider that the mutation introduced at position 264 can decrease proton currents by changing the electrostatic potential in the neighborhood of the H_v1 channel internal entrance. Although our data indicate that the N264 mutant does not modify the channel voltage dependence (*SI Appendix*, Figs. S3 and S4), measurements of this position accessibility to thiol-modifying agents was shown to be state-dependent. However, structural models suggest that this position is outside the electric field (7, 36), but more experiments are needed to confirm this claim. Finally, the inspection of the proton current recording of the monomeric *Ciona*-N264R mutant suggests that the positively charged guanidinium stabilizes the closed state of the channel, making the channel deactivation slower in the dimeric and monomeric *Ciona*-H_v1 (*SI Appendix*, Figs. S3 and S6), and in the dimeric mouse and human H_v1 containing the equivalent N210R (24) and N214R (35) mutation, respectively. A possible explanation to these findings is that the gating charge is trapped when the channel is activated upon depolarization, and it recovers slowly during the repolarization process, as we showed in this study.

We conclude that trapping is a consequence of the presence of the charged arginine chain in position 264. Given the fast deactivation rate shown by the WT monomeric H_v1 channel, the presence of a neutral asparagine in that position may have the effect of collapsing the barrier that separates states A_3 from B_1.

Methods

Mutagenesis, Transcription, and Sequencing. The single N264R mutation was introduced with a QuikChange kit (Promega Corp.) in a pSP64T-contained *C. intestinalis* H_v1 sequence kindly provided by Yasushi Okamura, Osaka University, Osaka, Japan. The ΔNΔC H_v1 was constructed with a stop codon at Val270 and an initiator methionine replacing Glu129 (6). Primers were designed using the web service QuikChange Primer Design. Mutant DNA was amplified by PCR, checked by sequencing, and then linearized with NotI restriction enzyme. In vitro transcription was performed with an mMESSAGE mMACHINE kit (Ambion) using RNA polymerase SP6. RNA was quantified by absorbance at 260 nm, and its integrity was checked by electrophoresis in 1% agarose gel with ethidium bromide at 0.6 μg/μL.

Oocyte Extraction and RNA Injection. *X. laevis* oocytes were obtained and injected with 50 nL of RNA at a concentration of 1 μg/μL according to previously described methodologies (26).

Electrophysiology. Voltage clamp recordings were performed in inside-out giant patches of oocytes membranes (37). The internal and external solutions contained 100 mM Hepes, 2 mM $MgCl_2$, 1 mM EGTA, and 50 mM *N*-methyl-D-glucamine (NMDG)-methanesulfonate. pH was adjusted with NMDG or methanesulphonate to 7.0. Measurements were performed at room temperature (22 °C). Pipettes of borosilicate capillary glass (1B150F-4; World Precision Instruments) were pulled on a horizontal pipette puller (Sutter Instruments) and fire polished until obtaining a diameter between 15 and 24 μm (resistances of 0.8 to 1.2 MΩ in the bath solution). Data were acquired with an Axopatch 200B amplifier (Axon Instruments). Both the voltage command and current output were filtered at 20 kHz with 8-pole Bessel low-pass filters (Frequency Devices). Analog signals were sampled with a 16-bit A/D converter (Digidata 1440A; Axon Instruments) at 250 kHz. Recordings were filtered off-line at 10 kHz by a digital 8-pole Bessel low-pass filter before analysis. Experiments were performed using Clampex 8 acquisition software (Axon Instruments). Capacitive currents were compensated by analog circuitry, and linear capacitive currents were subtracted using a P/-8 protocol with a subsweep holding potential of −90 mV (38).

Gating Current Simulations. A five-state kinetic model was simulated solving the equation $d\boldsymbol{P}(t)/dt = \boldsymbol{P}(t)\boldsymbol{Q}$, where $\boldsymbol{P}(t)$ is the probability vector of the states and $\boldsymbol{Q}$ is the transition rate matrix. We solved the time dependency of $\boldsymbol{P}(t)$ using the spectral expansion (39). Forward and reverse kinetic constants, $\alpha(V)$ and $\beta(V)$, respectively, were modeled as $\alpha(V) = \alpha_0 \exp(xz\delta e_0 V/kT)$ and $\beta(V) = \beta_0 \exp((x-1)z\delta e_0 V/kT)$, where α_0 and β_0 are the kinetic constants at $V = 0$ mV, $z\delta e_0$ is the charge moved in the transition, x is the fraction of the charge moved from a well to the barrier peak in each forward transition, and k and T have their usual meanings. Gating currents $I_g(t)$ were obtained with the equation $I_g(t) = N\boldsymbol{F}(t)\boldsymbol{Z}$, where N is the number of channels, $\boldsymbol{F}(t)$ is the net occupancy flux of each transition (40), and $\boldsymbol{Z}$ is a vector containing the charge associated to each transition. Parameters used in the model are listed in *SI Appendix*, Table S1.

Note. While this paper was under revision, detection of gating currents in the dimeric human proton channel mutant W207A-N214R (W257A-N264R in *Ciona*-H_v1) was reported (41). The method used by the authors to measure gating currents was stepping to a depolarizing voltage from different holding potentials, which is essentially a "Cole–Moore" protocol. Surprisingly, the gating current data do not show a Cole–Moore effect like the one reported here. This is an unexpected result, considering that the data also indicate that the gating current kinetics is defined by multiple states (41). However, the lack of a well-defined Cole–Moore effect may be due to the fast activation kinetics conferred by the W207A mutation (42).

ACKNOWLEDGMENTS. We thank Dr. David Baez for carrying out some of the initial preliminary experiments. This work was supported by Comisión Nacional de Investigación Científica y Tecnológica (CONICYT)-Programa Formación de Capital Humano Avanzado (PFCHA)/Doctorado Nacional/2017-21170395 (to E.M.C.), Fondo Nacional de Desarrollo Científico y Tecnológico (Fondecyt) Grants ACT 1104, Fondecyt 1180464 (to C.G.), 1150273 (to R.L.), and the US Air Force Office of Scientific Research (AFOSR) under Award FA9550-16-1-0384 (to R.L.). The Centro Interdisciplinario de Neurociencia de Valparaiso is a Millennium Institute supported by the Millennium Scientific Initiative of the Chilean Ministry of Economy, Development, and Tourism (P029-022-F).

1. Sasaki M, Takagi M, Okamura Y (2006) A voltage sensor-domain protein is a voltage-gated proton channel. *Science* 312:589–592.
2. Ramsey IS, Moran MM, Chong JA, Clapham DE (2006) A voltage-gated proton-selective channel lacking the pore domain. *Nature* 440:1213–1216.
3. DeCoursey TE (2018) Voltage and pH sensing by the voltage-gated proton channel, H_V1. *J R Soc Interface* 15:20180108.
4. Lee SY, Letts JA, Mackinnon R (2008) Dimeric subunit stoichiometry of the human voltage-dependent proton channel Hv1. *Proc Natl Acad Sci USA* 105:7692–7695.
5. Tombola F, Ulbrich MH, Isacoff EY (2008) The voltage-gated proton channel Hv1 has two pores, each controlled by one voltage sensor. *Neuron* 58:546–556.
6. Koch HP, et al. (2008) Multimeric nature of voltage-gated proton channels. *Proc Natl Acad Sci USA* 105:9111–9116.
7. Gonzalez C, Rebolledo S, Perez ME, Larsson HP (2013) Molecular mechanism of voltage sensing in voltage-gated proton channels. *J Gen Physiol* 141:275–285.
8. Gonzalez C, Koch HP, Drum BM, Larsson HP (2010) Strong cooperativity between subunits in voltage-gated proton channels. *Nat Struct Mol Biol* 17:51–56.
9. Cherny VV, Markin VS, DeCoursey TE (1995) The voltage-activated hydrogen ion conductance in rat alveolar epithelial cells is determined by the pH gradient. *J Gen Physiol* 105:861–896.
10. Musset B, et al. (2011) Aspartate 112 is the selectivity filter of the human voltage-gated proton channel. *Nature* 480:273–277.
11. Cherny VV, Murphy R, Sokolov V, Levis RA, DeCoursey TE (2003) Properties of single voltage-gated proton channels in human eosinophils estimated by noise analysis and by direct measurement. *J Gen Physiol* 121:615–628.
12. Fujiwara Y, et al. (2012) The cytoplasmic coiled-coil mediates cooperative gating temperature sensitivity in the voltage-gated H(+) channel Hv1. *Nat Commun* 3:816.
13. Larsson HP, Baker OS, Dhillon DS, Isacoff EY (1996) Transmembrane movement of the shaker K+ channel S4. *Neuron* 16:387–397.
14. Mony L, Berger TK, Isacoff EY (2015) A specialized molecular motion opens the Hv1 voltage-gated proton channel. *Nat Struct Mol Biol* 22:283–290.
15. Gandhi CS, Olcese R (2009) The voltage-clamp fluorometry technique. *Potassium Channels: Methods and Protocols*, ed Lippiat JD (Humana, Totowa, NJ), pp 213–231.
16. Cha A, Bezanilla F (1997) Characterizing voltage-dependent conformational changes in the Shaker K+ channel with fluorescence. *Neuron* 19:1127–1140.
17. Mannuzzu LM, Moronne MM, Isacoff EY (1996) Direct physical measure of conformational rearrangement underlying potassium channel gating. *Science* 271:213–216.
18. Qiu F, Rebolledo S, Gonzalez C, Larsson HP (2013) Subunit interactions during cooperative opening of voltage-gated proton channels. *Neuron* 77:288–298.
19. Aggarwal SK, MacKinnon R (1996) Contribution of the S4 segment to gating charge in the Shaker K+ channel. *Neuron* 16:1169–1177.
20. Seoh SA, Sigg D, Papazian DM, Bezanilla F (1996) Voltage-sensing residues in the S2 and S4 segments of the Shaker K+ channel. *Neuron* 16:1159–1167.
21. Baez-Nieto D, et al. (2014) Gating currents of monomeric Hv channel reveals a permeation pathway coupled to the voltage activation. *Biophys J* 106:233a.
22. Carmona EM, et al. (2018) Properties of the voltage-gated proton channel gating currents. *Biophys J* 114(Special Issue 3):546a.
23. De La Rosa V, Ramsey IS (2018) Gating currents in Hv1 proton channels. *Biophys J* 114(Special Issue 3):124a.
24. Sakata S, et al. (2010) Functionality of the voltage-gated proton channel truncated in S4. *Proc Natl Acad Sci USA* 107:2313–2318.
25. Cole KS, Moore JW (1960) Potassium ion current in the squid giant axon: Dynamic characteristic. *Biophys J* 1:1–14.
26. Gonzalez C, Rosenman E, Bezanilla F, Alvarez O, Latorre R (2000) Modulation of the Shaker K(+) channel gating kinetics by the S3-S4 linker. *J Gen Physiol* 115:193–208.
27. DeCoursey TE, Cherny VV (1994) Voltage-activated hydrogen ion currents. *J Membr Biol* 141:203–223.
28. Chandler WK, Rakowski RF, Schneider MF (1976) A non-linear voltage dependent charge movement in frog skeletal muscle. *J Physiol* 254:245–283.
29. Armstrong CM, Bezanilla F (1977) Inactivation of the sodium channel. II. Gating current experiments. *J Gen Physiol* 70:567–590.
30. Bezanilla F, Villalba-Galea CA (2013) The gating charge should not be estimated by fitting a two-state model to a Q-V curve. *J Gen Physiol* 142:575–578.
31. Hong L, Kim IH, Tombola F (2014) Molecular determinants of Hv1 proton channel inhibition by guanidine derivatives. *Proc Natl Acad Sci USA* 111:9971–9976.
32. Hong L, Pathak MM, Kim IH, Ta D, Tombola F (2013) Voltage-sensing domain of voltage-gated proton channel Hv1 shares mechanism of block with pore domains. *Neuron* 77:274–287.
33. Hong L, Singh V, Wulff H, Tombola F (2015) Interrogation of the intersubunit interface of the open Hv1 proton channel with a probe of allosteric coupling. *Sci Rep* 5:14077.
34. Randolph AL, et al. (2016) Proton currents constrain structural models of voltage sensor activation. *eLife* 5:e18017.
35. Ramsey IS, et al. (2010) An aqueous H+ permeation pathway in the voltage-gated proton channel Hv1. *Nat Struct Mol Biol* 17:869–875.
36. Takeshita K, et al. (2014) X-ray crystal structure of voltage-gated proton channel. *Nat Struct Mol Biol* 21:352–357.
37. Hilgemann DW (1995) The giant membrane patch. *Single-Channel Recording*, eds Sakmann B, Neher E (Springer US, Boston), pp 307–327.
38. Armstrong CM, Bezanilla F (1973) Currents related to movement of the gating particles of the sodium channels. *Nature* 242:459–461.
39. Colquhoun D, Hawkes AG (1995) A Q-matrix cookbook. *Single-Channel Recording*, eds Sakmann B, Neher E (Springer US, Boston), pp 589–633.
40. Vandenberg CA, Bezanilla F (1991) A sodium channel gating model based on single channel, macroscopic ionic, and gating currents in the squid giant axon. *Biophys J* 60: 1511–1533.
41. De La Rosa V, Ramsey IS (2018) Gating currents in the Hv1 proton channel. *Biophys J* 114:2844–2854.
42. Cherny VV, et al. (2015) Tryptophan 207 is crucial to the unique properties of the human voltage-gated proton channel, hHV1. *J Gen Physiol* 146:343–356.

Chapter 11

Methods for Investigating TRP Channel Gating

Osvaldo Alvarez, Karen Castillo, Emerson Carmona, Carlos Gonzalez, and Ramon Latorre

Abstract

A complete characterization of temperature -and voltage-activated TRP channel gating requires a precise determination of the absolute probability of opening in a wide range of voltages, temperatures, and agonist concentrations. We have achieved this in the case of the TRPM8 channel expressed in *Xenopus laevis* oocytes. Measurements covered an extensive range of probabilities and unprecedented applied voltages up to 500 mV. In this chapter, we describe animal care protocols of patch-clamp pipette preparation, temperature control methods, and analysis of ionic currents to obtain reliable absolute open channel probabilities.

Key words TRPM8, Xenopus care, Oocytes extraction, Patch clamp, Pipette pulling, Temperature control, Noise analysis, TRP channels, Gating mechanism

1 Introduction

Since TRP channels are polymodal receptors with allosteric gating, the researchers find experimental limitations or barriers trying to characterize channel behavior under the influence of different stimuli. Such as how to obtain an accurate determination of the absolute maximum open probability in a wide range of agonist concentration, temperatures, and voltages. The low voltage dependence of TRP channels forces investigators to apply extremely depolarized voltages to obtain saturation of the conductance–voltage curves. Instantaneous tail current measurement is the ideal procedure to obtain conductance–voltage curves. However, deactivation of TRP channel is often very fast in comparison with the voltage clamp dynamics. How to get an accurate measurement of the time course of deactivation process? How to avoid clamp errors when channels are overexpressed? One of the most satisfying achievements of our group has been to be able to measure the

Electronic supplementary material: The online version of this chapter (https://doi.org/10.1007/978-1-4939-9446-5_11) contains supplementary material, which is available to authorized users.

Antonio Ferrer-Montiel and Tim Hucho (eds.), *TRP Channels: Methods and Protocols*, Methods in Molecular Biology, vol. 1987, https://doi.org/10.1007/978-1-4939-9446-5_11,

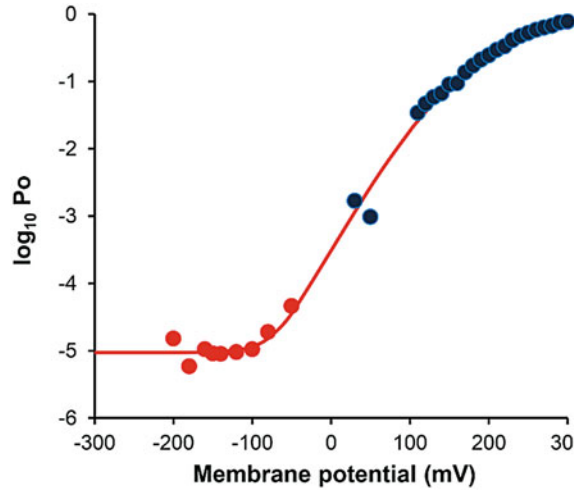

Fig. 1 TRPM8 open channel probability at 28 °C. TRPM8 expressed in *Xenopus laevis* oocytes. We determine the open channel probability from current noise analysis under voltage clamp. Blue dots correspond to tail currents measured at different voltages, normalized by the absolute open channel probability at 260 mV and 28 °C determined using nonstationary noise analysis. Red dots correspond to determinations on *NPo* from noise analysis of currents measured at extreme negative voltages where the open channel probability is minimal

TRPM8 absolute open channel probability (*Po*) when expressed in *Xenopus laevis* oocytes. This determination covered an extensive range of P_O, ranging five order of magnitude in response to applied voltages in an interval expanding −300 to 500 mV [1] (*see* example in Fig. 1). We learned that depolarization is only a partial activator of TRPM8 channels. In the limit of very large depolarization, the P_O turns voltage-independent, and it is 0.41 at 30 °C and increase to 0.91 at 10 °C. *See* Figure 3 in Raddatz et al. [1]. In the limit of very large hyperpolarization, the open channel probability is also voltage-independent. We also discovered that when all the voltage sensors are at rest (large hyperpolarization), cold temperature is a potent activator of TRPM8 channels: it increases dramatically from $9.3\ 10^{-6}$ at 28 °C to $1.2\ 10^{-3}$ at 10 °C. *See* Figure 4 in Raddatz et al. [1]. We were also able to increase the bandwidth of the current measuring system to be able to determine deactivation time constants <50 μs, unveiling two distinct temperature-dependent processes. We explained our findings using a three-tiered allosteric kinetic scheme with two closed levels and one open level. Each tier consisting of 25 states: with 0, 1, 2, 3, or 4 voltage and temperature sensors active. *See* Figure 9 in Raddatz et al. [1]. In this chapter, we will describe how we accomplished this by giving the appropriate details of animal care, oocyte handling, patch-clamp pipette preparation, electronic equipment, temperature control, and analysis of macroscopic and single-channel current records.

2 Materials

2.1 Animal Care and Oocyte Preparation

1. Frog brittle SA05960, Nasco.
2. Recirculating water system (XenopLus, Techniplat, Buguggiate VA, Italy).
3. Water test kit for aquariums (Sera Aqua-Test Box, Sera, Germany).
4. Sera Marin Salt (Sera, Germany).
5. Biological filter for recirculation water.
6. Tricaine solution (0.1%): Dissolve 625 mg of tricaine methanesulfonate 80% in 500 mL dechlorinated water. Neutralize pH to 7–7.5 with NaOH 0.5 M.
7. Povidone–iodine 10% (Betadine).
8. Oocyte Ringer 2 calcium-free buffer (OR2): 82.5 mM NaCl, 2 mM KCl, 1 mM $MgCl_2$, 5 mM HEPES supplemented with 0.3 mg/mL amikacin, 10 U/mL penicillin, and 10 μg/mL streptomycin. Adjust pH to 7.4 and sterilize by filtration. Store at 4 °C.
9. ND96 buffer: 96 mM NaCl, 2 mM KCl, 1.8 mM $CaCl_2$, 1 mM $MgCl_2$, 5 mM HEPES supplemented with 0.3 mg/mL amikacin, 10 U/mL penicillin, and 10 μg/mL streptomycin. For oocyte maintenance after RNA injection, also supplement with 2.5 mM sodium pyruvate. Adjust pH to 7.4 and sterilize by filtration. Store at 4 °C (*see* **Note 1**).
10. Collagenase 1.8 mg/mL: Dissolve 27 mg of collagenase D (from *Clostridium histolyticum*, 11088882001, Roche) in 15 mL OR2.
11. Mini-shaker (Multi Bio 3D, Biosan, Latvian Republic).
12. Sterile N° 11 scalpel blades.
13. Swiss scissors (9 cm), surgery materials are sterilized by autoclave before surgery, unless already sterile.
14. Rat toothed teeth dissecting tissue forceps.
15. Sterile coated VICRYL® (polyglactin 910) suture (Ethicon, USA).
16. Glass petri dishes (100 and 60 mm) sterilized by autoclave.
17. Sterile 50 mL conical tubes.
18. Two Dumont #5 tweezers for vitelline membrane removal.

2.2 RNA Preparation and Injection

1. TRPM8 DNA inserted into a plasmid optimized for heterologous expression in *Xenopus laevis* oocytes (*see* **Note 2**).
2. QIAprep Spin Midiprep Kit (cat # 12143, QIAGEN, Redwood City, CA, USA).

3. QIAquick Gel Extraction Kit (cat# 28704, QIAGEN, Redwood City, CA, USA).
4. *E. coli* XL1-Blue competent cells (Catalog #200249 Stratagene, La Joya, CA, USA).
5. mMESSAGE mMACHINE T7 Ultra kit (cat # AM1344, Thermo Fisher Scientific, Waltham, MA, USA).
6. *Not*I restriction enzyme (cat# R0189S, New England Biolabs, Ipswich, MA, USA).
7. RNase ZAP decontamination solution (cat# AM9780, Thermo Fisher Scientific, Waltham, MA, USA).
8. NANOLITER microinjector (NANOLITER 2010, World Precision Instruments, Sarasota, FL, USA).
9. Glass capillaries (cat# 4878, World Precision Instruments, Sarasota, FL, USA).
10. Micropipette puller (P 97, Sutter Instruments, Novato, CA, USA).
11. Nail scissors.
12. An RNase-free workbench.
13. A UV-sterilized workstation equipped with a precision stereo zoom binocular microscope and a fiber-optics cold light source.

2.3 Electrophysiology

1. Solutions used for electrophysiology. Bath and pipette solutions composition in mM: KMES 140, KCl 2, EGTA 5, HEPES 10, adjusted to pH 7.5 with KOH.
2. Borosilicate glass capillaries (cat # 1B150F-4. World Precision Instruments, Sarasota, FL, USA).
3. Axopatch 200B amplifier (Molecular Devices, Sunnyvale, CA, USA).
4. Micropipette puller (P 97, Sutter Instruments, Novato, CA, USA).
5. Microforge (MF-840 Narishige, Tokio, Japan).
6. 8-pole low pass Bessel filter (cat # 900C9L8L, Frequency Devices, Ottawa, Canada).
7. Antivibration table and Faraday cage.
8. Binocular microscope (PZM, WPI, Sarasota, FL, USA).
9. Micromanipulator (model MX-2, Narishige, Tokyo, Japan).
10. Analog–digital interface NI-PCI-6014 Card (National Instruments).
11. pCLAMP 10 software (Molecular Devices, Sunnyvale, CA, USA).
12. Analysis software [2].
13. Excel software (Microsoft, Redmont, WA, USA).

3 Methods

3.1 Animal Care

A survey on the practices of *Xenopus laevis* maintenance reveals no consistency among husbandry practices for this species [3]. We will share our protocols to maintain animals, even though there are several reports on animal care and oocyte preparation available [4–8].

We used wild-caught animals from local colonies in central Chile. We have maintained frogs in a static facility, which consists of opaque and covered plastic containers of 40 L with 2 to 4 animals. Alternatively, we use a recirculating water system (XenopLus, Techniplat, Buguggiate VA, Italy), and currently, we have frogs in both types of systems. For both cases, we maintain frogs in tanks with 4 L of water per frog. We have both systems located in the same room, at 18 °C and with a 12/12 h light/dark cycle. Frogs are fed twice a week with frog brittle food (cat# SA05960(LM)M, Nasco). Nutritional status of animals is maybe one of the most critical factors to determine oocyte quality [6, 9].

Additionally, an essential factor for frog maintenance is water quality. For the static system, we used tap water left at least 48 h exposed to the air to dechlorination. Dechlorinated water pH is commonly 8–8.5, so we adjusted it to 7.5 with HCl. We check water parameters with a commercial kit for aquariums (Sera Aqua-Test Box, Sera, Germany) once a month. In the static system the water quality parameters are 148–160 mg/L KH (carbonate hardness), less than 0.5 mg/L of NH_4 and NH_3, undetectable levels of nitrate, and nitrite, 303–312 mg/L GH, (general hardness) and pH 7.5. Twice a week, after feeding, we clean the tanks to remove dirt and uneaten food with a brush and dechlorinated water.

In the recirculating system, we maintain 2–3 animals in dark plastic cages of 13.4 L. Water is dechlorinated by a double filter, maintained at 18 °C, 1100 μS conductivity, and pH 7.5 using Sera Marin Salt (Sera, Germany) and $NaHCO_3$. A biological filter keeps low-toxic nitrogen levels, while a carbon mechanic filter and UV radiation conserve cleaning of the water.

3.2 Oocyte Preparation

We obtain oocytes from *Xenopus laevis* frog as previously described [10]. Frogs are anesthetized by immersion in 0.1% tricaine, and the lobules that contain the oocytes are extracted using fine tweezers through a small abdominal incision (≤1 cm). Frogs are left to recover for 60 days before a new surgery for oocytes extraction. Additionally, each frog is used for a maximum of four times to obtain its oocytes.

1. Anesthetize the animal in 500 mL of fresh 0.1% tricaine solution, by leaving it for 30 min or until legs movement is absent when stretched.

2. Remove animal from the anesthetic and lay it with the abdomen facing up over a paper towel. Rub the frog abdomen with a swab of povidone–iodine. Place a plastic film (food wrap) on the frog abdomen, and apply on it another swab of povidone–iodine to maintain germ-free conditions during surgery, because the skin of the animal is a potential source of microorganisms contamination (*see* **Note 4**).
3. Open a 1 cm diagonal incision in one of the sides of the abdomen using a sterile scalpel, and extract two or three lobules using rat-toothed teeth dissecting tissue forceps. Place the lobules in a 50 mL conical tube with cold OR2 buffer. Remove the plastic film and suture the incision in the animal, first joining the muscle, and then the skin. Clean the closed wound with povidone–iodine and leave the frog in a new tank, with low water level for recovery for 24 h before returning it to the tank with the other animals (*see* **Note 5**).
4. We process the lobule the same day of surgery and have obtained excellent results to record single and macroscopic channel currents. Remove the external matrix to expose the oocytes, and wash it five times with OR2 buffer on a glass petri dish. Separate the grouped oocytes contained in the lobule in small pieces of 8–12 oocytes using fine tweezers, to improve the access of collagenase to remove the follicular membrane. Transfer the dispersed lobules to a 50 mL conical tube with fresh OR2 buffer using a sterile plastic pipette. Wash the oocytes five times with new OR2 buffer applying a manual rotation of the container.
5. In a 50 mL Falcon tube, incubate 10 mL of oocytes adding 5 mL of 1.8 mg/mL collagenase prepared in the OR2 buffer at 18 °C. Shake the oocytes at 75 rpm during 60 min using a mini-shaker (Multi Bio 3D, Biosan, Latvian Republic). It is recomended to inspect the oocytes every 15 min, to avoid excessive collagenase treatment. Stop the incubation when most of the oocytes look separated (*see* **Note 6**).
6. Wash oocytes five times with cold OR2 buffer, and then transfer only the isolated oocytes to a new 50 mL tube with OR2 buffer using a 3 mL sterile bulb driven plastic transfer pipette with the tip cut. Eliminate oocyte aggregates because they still could contain collagenase. Additionally, minimize transferring an excess of OR2 buffer along with the oocytes to get rid of collagenase. Wash oocytes with new OR2 buffer until the solution is clear (at least five times) (*see* **Note 7**). Before injection, select oocytes under a stereoscope and if needed remove the rest of follicular membrane that may remain on the oocytes, manually.

7. Transfer isolated oocytes to a new 50 mL conical tube with 30 mL of a cold ND96 buffer using a new sterile plastic pipette. Wash at least ten times with ND96 buffer.
8. Transfer only isolated oocytes to a 100 mm glass petri dish with fresh ND96 using a new 3 mL plastic sterile transfer pipette to select only the isolated oocytes.
9. Select good oocytes under a stereomicroscope. We choose oocytes with folicular membrane completelly removed, but if they still conserve part of the follicular membrane, we manually remove it for injections. Complete follicular membrane removal by passing the oocyte through a cut off micropipette tip of the appropriate diameter. Only good quality oocytes pass this procedure, defective ones will not resist mechanical removal of the follicular membrane. Leave selected oocytes in a 60 mm glass dish with fresh ND96 supplemented with pyruvate, O.N. To maximize expression, stage IV and V oocytes should be chosen, and oocytes should recover from enzymatic treatment for at least 6 h before RNA injection [8] (*see* **Note 8**).
10. For patch-clamp recordings, remove the vitelline membrane using two Dumont #5 tweezers, under a stereo microscope. Transfer the oocyte to a 35 mm culture plate filled with the electrophysiological recording solution. Under stereomicroscope at high magnification, hold the vitelline membrane with one tweezers. With the second tweezers grasp the vitelline membrane near the first one, and separate the tweezers to get rid of the vitelline membrane entirely (*see* **Note 9**).

3.3 RNA Preparation

For expressing TRPM8 ion channels in *Xenopus laevis* oocytes, we use the pBSTA plasmid that is a construct optimized for this purpose [11, 12]. Plasmid pBSTA contains the T7 promoter, and multiple cloning regions for DNA insertion, as well as noncoding 3′ and 5′ β-globin sequences and poly(A) tail [11]. These features significantly increase the expression and stability of exogenous RNAs in oocytes [13]. We subcloned the rat TRPM8 cDNA (provided by Dr. David Julius, UCSF Physiology), into the pBSTA plasmid provided by Dr. Ligia Toro (UCLA Brain Research Institute).

3.4 Procedure for RNA Preparation

1. Amplify the pBSTA-rTRPM8 plasmid transforming *E. coli* XL1-Blue competent cells (Stratagene, La Joya, CA, USA) using heat shock, following recommended protocol (www.chem-agilent.com/pdf/strata/200229.pdf).
2. Extract and purify the DNA from the transformed cells following the QIAprep kit protocol instructions (www.qiagen.com/handbooks).

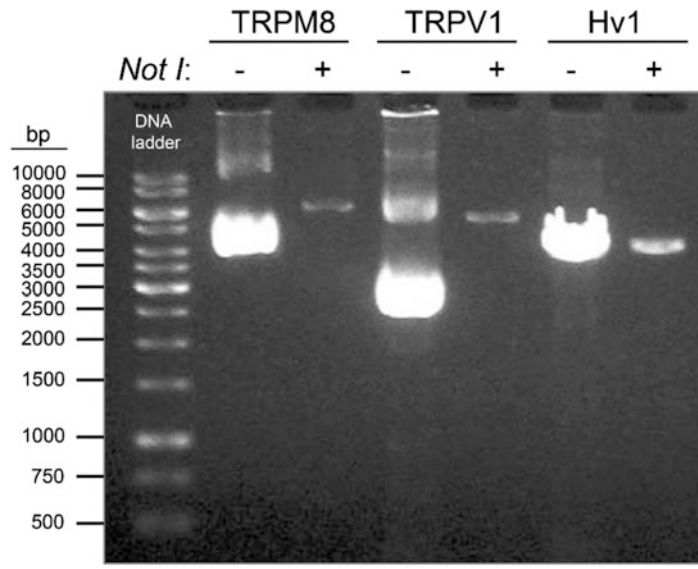

Fig. 2 Gel electrophoresis for TRPM8, TRPV1, and Hv1 channels before (−) and after (+) digestion with *Not*I restriction enzyme (New England Biolabs, cat# R0189S, Ipswich, MA, USA), used to linearize the DNA. Once linearized, DNA is ready for use in vitro transcription to obtain RNAs for *Xenopus laevis* oocytes injection to do electrical recordings. The electrophoresis on a 1% agarose gel prepared in buffer TAE (Tris-acetate-EDTA) complemented with ethidium bromide (Sigma-Aldrich, cat# E1510, MO-USA) to visualize the DNA sample bands on a UV transilluminator. At the left, a DNA ladder of 1 kb (Fermentas, cat# SM0311, MA-USA) is loaded to check out the expected molecular size of nonlinearized versus linearized DNAs

3. Quantify the concentration of the plasmid containing the DNA of interest by measuring absorbance at 260 nm and linearize it with *Not*I restriction enzyme.
   (a) Incubate 10 μg of DNA with *NotI*, O.N. at 37 °C.
   (b) Check linearization by electrophoresis on a 1% agarose gel and compare with those nonlinearized DNAs, look for a single band that migrates less than nonlinearized DNA as illustrated in Fig. 2.
4. Clean the linearized DNA to improve transcription efficacy, using the QIAquick Gel Extraction Kit protocol (www.qiagen.com/handbooks).
5. Use 1 μg of clean linearized DNA obtained in **step 4** for the in vitro transcription with mMESSAGE mMACHINE T7 Ultra kit, following the protocol of Ambion. (https://www.thermofisher.com/order/catalog/product/AM1340) (*see* **Note 10**).

Using this methodology, we obtain between 5 and 15 μg/μL of RNA transcripts. For TRP transcripts, we dilute the RNA to 3 μg/μ

L, which is our RNA stock. From this, aliquots of 1 or 2 μL of 1:100, 1:500, or 1:1000 dilutions are used to inject the oocytes, depending on electrophysiological requirements such as macroscopic or single channel recordings. We store RNA stock and aliquots at −80 °C until used.

3.5 Procedure for RNA Injection

We follow injection procedure we outlined previously [10]. We inject 50 nL of RNA per oocytes, at the desire dilution using a nanoliter microinjector (NANOLITER 2010, World Precision Instruments, MA, USA) in a UV-sterilized workstation equipped with a precision stereo zoom binocular microscope and a fiber optics cold light source. We used glass micropipettes (cat# 4878, World Precision Instruments, FL, USA), pulled in a P-97 micropipette puller (Sutter Instruments, CA USA) to obtain long and thin micropipettes as shown in Fig. 3. Glass capillaries (cat# 4878, World Precision Instruments, FL USA). Then we cut the tip of the micropipette (with a small scissor) to obtain a bevel at the tip with a diameter of 15–30 μm. This custom-made injection needle is backfilled with RNAse free mineral oil and then forward filled with the cRNA of the ion channel of interest. We put 1–2 μL of RNA in a small piece of Parafilm, and RNA is drawn into the needle using the microinjector. Typically, we inject several (10–30) oocytes with 50 nL of RNA each in a few minutes. We maintain the injected oocytes in ND-96 solution at 18 °C. After 3–5 days; oocytes are ready to use for electrical recordings in a temperature-controlled microscope stage mounted in a patch-clamp setup.

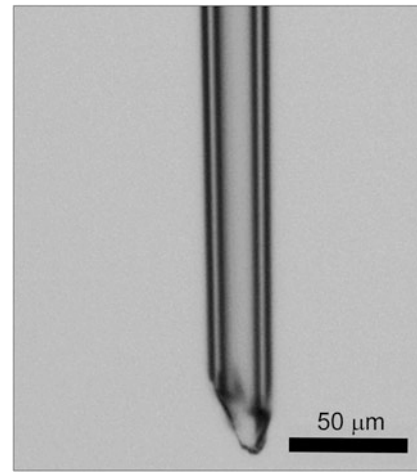

Fig. 3 Photograph of an RNA injection needle tip. Glass capillaries are drawn using a Sutter P-97 horizontal Flaming/Brown micropipette puller and cut using a small scissors to make the bevel

3.6 Patch-Clamp Pipettes Manufacture for Giant Patches

To achieve 40 kHz bandwidth, low noise and a large number of channels per patch we use cell-attached macro patches [14]. We draw the patch pipettes in a horizontal puller from borosilicate glass capillaries using the following parameters: (*see* **Note 11**). Stretched pipettes are fire polished using a microforge (Narishige), under a microscope. Tips are fire polished up to obtain the desired shape and diameter (>15 μm) for our electrophysiological demands (*see* Fig. 4 and **Note 12**).

3.7 Electronic Equipment

We used the Axopatch 200B amplifier in electrochemistry mode. In this configuration, the membrane voltage range is ±1 V. Capacitive current decay with a time constant of 5 μs that is six times faster than the fastest TRPM8 tail transient components (*see* Figure 1 in Raddatz et al. [1]). Analog current data stream was low-pass filtered at 40 kHz, sample and digitized at 5 μs per sample, and stored for

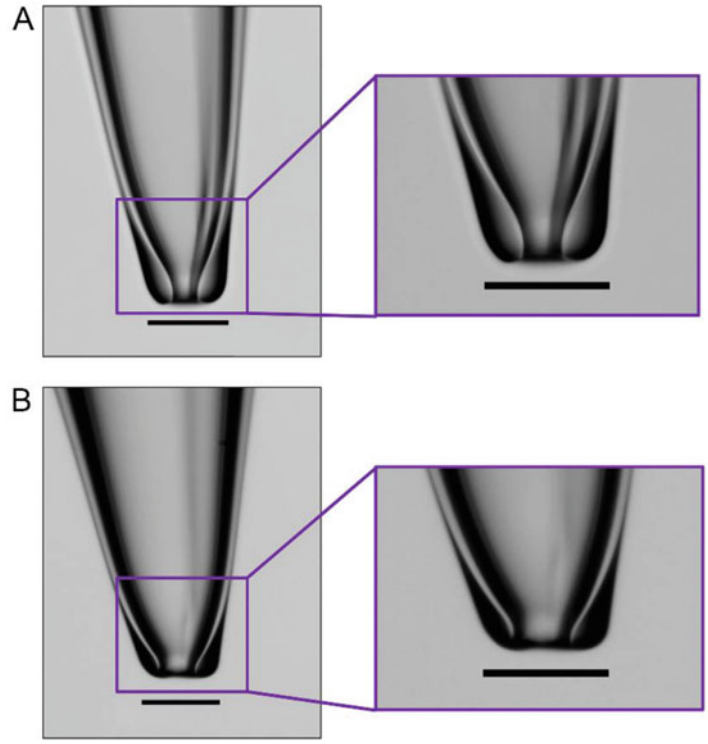

Fig. 4 Photographs of two macro patch pipettes tips drawn using a Sutter P-97 Flaming/Brown micropipette puller, and fire polished using the Narishige PM-840 microforge. Panel **a** shows a pipette with an approximate diameter of 15 μm, and on the right, we show a magnification. Panel **b** shows a pipette with a higher diameter of approximately 21 μm. The scale bar is 50 μm for all pictures. Pipette resistance, when filled with 150 mM NaCl, is 880 kΩ for 10 μm, 380 kΩ for 15 μm, and 188 kΩ for 24 μm. Borosilicate glass capillaries (1B150F-4. World Precision Instruments, Sarasota, FL, USA)

off-line analysis. We use Clampfit 10 software (Molecular Devices) for voltage pulses generation and data acquisition (*see* **Note 13**).

3.8 Temperature Control

TRPM8 channels are cold sensors; the open channel probability depends strongly on temperature what critically demands a tight control of this variable. In 2008 we constructed from scratch an electronic temperature controller based on temperature detection using a thermistor and withdrawing heat using a Peltier element driven by a power amplifier. The smart logic of the system, an implementation of a proportional, integral and differential controller, resides in an Arduino board featuring an ATmega328 microprocessor. The recording chamber, made in our laboratory, consisted of a glazed aluminum block with an excavation for the 250 μL oocyte bath, located above a heating–cooling Peltier element. This arrangement makes efficient heat transfer from the chamber to the Peltier element. A hollow brass heat sink is situated under the Peltier element and cooled by water circulation. Since the recording chamber is opaque, illumination comes from the top. *See* Fig. 5a for an illustration our oocyte thermoregulated recording chamber and temperature control performance. The feedback system is maintained at the temperature set value ±0.2 °C, and temperature settled in less than 1 min for 2 °C temperature jumps (*see* an illustration in Fig. 5b).

3.9 Electrophysiological Data Analysis

We recorded currents elicited by TRPM8 channels using the patch clamp technique on the cell-attached configuration. Figure 4 shows photographs of two pipette tips suitable for the macro patch. Bath and pipette solutions are the same and contain 2 mM KCl. Silver–silver chloride electrodes in the bath and into the pipette are in contact with 2 mM Cl^-, for symmetric electrode potential. We assume that the oocyte resting potential is zero (*see* **Note 14**).

3.9.1 Counting the Number of Channels from Macroscopic Current in the Patch

We used the nonstationary noise analysis procedure to count the number of channels in the patch membrane to obtain a precise estimation of the probability to find the channel in the open state. Upon membrane depolarization up to 260 mV from a holding potential of −50 mV, the current relaxes to a steady state value. We recorded the time course of the current rise in a set of 100 sweeps at the same membrane potential. For each time point of the data records, (isochrones) we calculate the mean ($<I>$) and the variance (σ^2) of the current over the entire set of sweeps (*see* **Note 15**). A plot of σ^2 vs. $<I>$ is a parabola [15, 16] of the form:

$$\sigma^2 = i\langle I\rangle - \frac{\langle I^2\rangle}{N} \tag{1}$$

In Eq. 1, i is the single-channel current and N is the number of channels present in the patch.

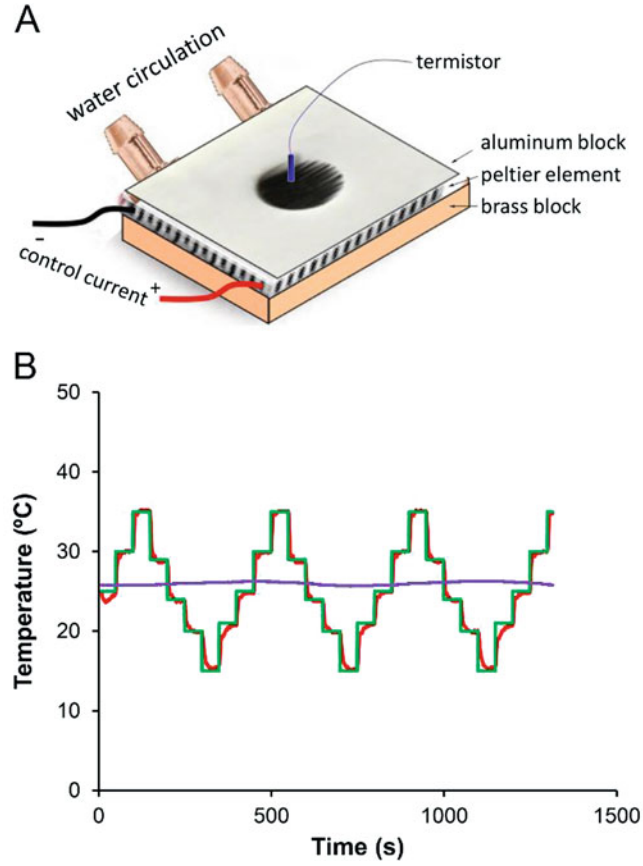

Fig. 5 Oocyte thermoregulated chamber and temperature control. (**a**) The figure illustrates the recording chamber fabricated with an aluminum block that has a ~200 μL excavation machined to home the oocyte bath. A thin layer of nail enamel covers the upper aluminum surface for electrical insulation. Beneath a Peltier element, there is a hollow brass block for water circulation. Heat-conducting compound on both surfaces of the Peltier element provides excellent heat transfer. A microprocessor (Arduino Uno board) electronic control system drives current through the Peltier element (Ferrotec Bedford, NH, USA). The thermistor (QTI Sensing Solutions, Boise, Idaho, USA) senses the temperature and informs the controller. Heat conductive compound facilitates heat transfer between the elements. Water circulation through the hollow brass block dissipates the heat. (**b**) This graph shows the temperature control performance. The green line is the temperature set point, and the red trace is the actual oocyte chamber temperature measured by the thermistor. The purple line is the room temperature measured using a digital thermometer

We use the Solver complement of Microsoft Excel to find i and N. Data weighs need correction (data binning) before using Solver for equal representation of all mean currents. In Fig. 6, we show the effect of the weighing on the resulting parabola fitted, as well as one practical solution to the problem (*see* **Note 16**). Note that the first

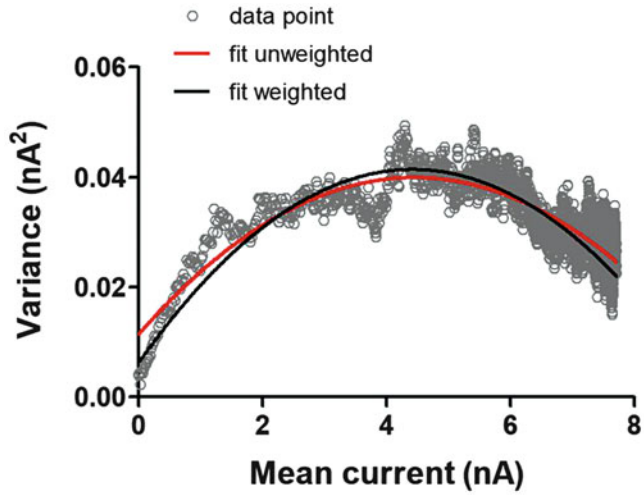

Fig. 6 Noise analysis of variance versus mean-current plots. The scattered curve is the variance vs. mean current plot. As the current grows along an exponential time course, data points get crowded as the curve approaches the asymptotic steady-state value, as shown in the graph. Unweighted curve fitting results in the parabola drawn on red. This curve misses the points taken at lower mean currents. We count the number of samples in 0.1 nA bins along the current axis, and we divide the squared errors by this count before minimizing the sum of squares. This weighting procedure results in a better representation of the experimental data, as we show in the black parabola. These data belong to TRPM8 noise recordings taken at 260 mV and 20 °C. The results of the weighted curve fitting are $i = 16$ pA for the single-channel current, $N = 557$ the number of channels in the patch, and $P_0 = 0.87$. The results of the unweighted analysis are $i = 13$ pA, $N = 700$, and $P_0 = 0.86$

derivative of the variance is $i\text{-}2/N$. Therefore, it is equal to i in the limit of $<I> \rightarrow 0$. Also, the maximum of the variance occurs at $<I>/iN = ½$, when the derivative is zero and occurs when exactly one-half of the channels are open (maximum noise).

We calculate the open channel probability, P_O, at a given voltage by dividing mean current by the unitary channel current times the number of channels in the patch:

$$P_O = \frac{\langle I \rangle}{iN} \tag{2}$$

This procedure is applicable for temperature and voltages where $P_O > 0.5$. Using this method, we learned that for TRPM8 the maximum absolute open channel probability obtained at a very high positive potential, never reaches 1.0, and it is lower the higher the temperature [1]. To determine the open channel probability for $P_O < 0.5$ we measured the instantaneous tail current after depolarization to different voltages and constructed the $G_{tail}/G_{tail,max}$ vs. voltage relationship (*see* **Note 17**). We obtain the P_O vs. voltage

plot was by scaling the $G_{tail}/G_{tail,max}$ vs. voltage plot by the absolute P_O determined at a known voltage using Eq. 2 (*see* Figures 2 and 3 in Raddatz et al. [1]).

3.9.2 Determination of the Open Channel Probability at Extremely Low P_O

Using the methods described above, we determined the open channel probabilities plotted in blue symbols in Fig. 1. We calculated the red points, for very low open *Po*, using noise analysis of the current recorded at negative voltages. It is interesting to look for these P_Os to find out what is the temperature effect when the TRPM8 voltage sensors are at rest. We found that in this voltage regime lowering the temperature increases the open probability several orders of magnitude (*see* Figure 4 in Raddatz et al. [1]). Since P_O at negative voltages is very low, P_O can be determined using the Poisson distribution [17].

$$P_k = \frac{(NP_O)^k}{k!} e^{-NP_O} \tag{3}$$

In Eq. 3, P_k is the probability of finding k open channels in a membrane with N channels with a given P_O. Knowing the N and i, we calculated the probability density function of the current, PDF. The probability density function is the sum of Gaussian distributions to I, with center values on the current i_k carried by k open channels with $k = 0, 1, 2\ldots$up to 9 possible open channels, an area equal to P_k (Eq. 3) and a standard deviation $\sigma^2{}_k$ [1].

$$\text{PDF} = \sum_0^9 \frac{P_K}{\sigma_k\sqrt{2\pi}} e^{-\frac{(I-ik)^2}{2\sigma_k^2}} \tag{4}$$

The standard deviation σ_k is the sum of the standard deviation of the closed channel, σ_0, and k times the standard deviation of the open channel; σ_1. For $k = 0$ we used a skewed Gaussian distribution [18, 19] to account for the distribution for the asymmetry caused by the effect of the acquisition system on the channels closing [20]. To perform the calculations more accessible, we used the Excel built-in functions to calculate the Poisson, the normal, and the skewed normal distributions (*see* Fig. 7). As a supplemental material, we release a copy of the Excel spreadsheet with the code to calculate the PDF and the application to determine NP_O in a real experiment (NPo calculation.xlxs). We will search for P_O constructing the PDF in Eq. 4, with a *Po* such that makes this PDF equal to the experimentally determined PDF on a real membrane. The raw data used to construct the experimental PDF look like the record we show in Fig. 4 taken at 20 °C and −130 mV. An all points histogram of the frequency of finding a given current, I, was compiled by Clampfit (pClamp 10 software, Molecular Devices). The experimental PDF is the normalization of this histogram to have an integral = 1.0. We showed the result of this calculation on Fig. 4 in Raddatz et al. [1]. The P_O values calculated using this procedure are the red symbols in Fig. 1.

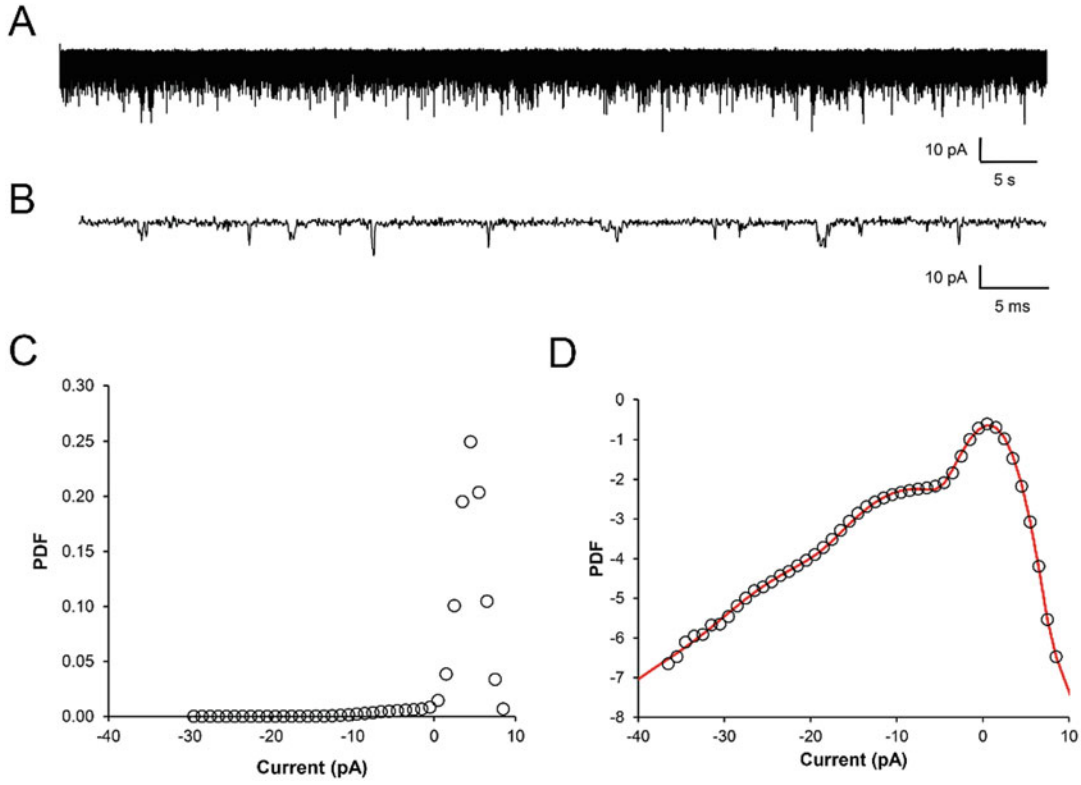

Fig. 7 Representative recordings of TRPM8 currents used to calculate NP_O at extremely low probability. (**a**) 90 s of a record of TRPM8 current fluctuations recorded at 20 °C and −130 mV. (**b**) Expanded view of a section of the record showed in *A*. (**c**) A normalized histogram of the baseline corrected current recorded during the full 90 s shown in *A*, with 1 pA bin width, created by Clampfit 10.3. (**d**) Normalized histogram plotted on logarithmic scale, red line is the best PDF computed using Eqs. 3 and 4, $NPo = 0.056$ and single-channel current −7.8 pA, $\sigma^2_0 = 2.1$ pA^2, $\sigma^2_1 = 1.6$ pA^2, and $\alpha = -1.3$. Plots were drawn using Microsoft Excel 2016 and curve fitting was performed by Solver Excel complement. *See* also Excel program *NPo calculation.xlxs* released as Electronic Supplemental Material

4 Notes

1. Avoid storage of ND96 supplemented with pyruvate for extended periods of time due to pyruvate polymerization and degradation.
2. We use plasmid pBSTA to express TRPM8 and TRPV1, but we pSP64T worked better for the expression of Hv1. For other ion channels such as BK, we use pGEM plasmid.
3. We have used either wild-caught animals from central Chile or bought from Nasco (https://www.enasco.com) and found no difference in oocyte quality.

4. Performing surgery under antiseptic conditions is crucial since one of the reasons of poor quality oocytes is contamination with multidrug-resistant bacteria or fungi [21, 22].
5. Oocytes are sensitive to high temperatures, so we avoid handling them over 18 °C for extended periods.
6. Prolonged collagenase treatment will reduce oocyte quality and RNA expression [8]. Never exceed 1 h.
7. Collagenase removal. Repeated washing steps are necessary before to transfer oocytes from calcium-free OR2 to ND96. It is crucial to remove collagenase since enzyme activity increases many times in the presence of calcium, which is absent in OR2 buffer, but it is present in the ND96 buffer.
8. We pay particular attention to the clean conditions of the surgery and oocyte cleaning to avoid microorganism contamination of the frog and of the oocytes, which decreases their quality. We choose collagenase D (from *Clostridium histolyticum*, 11088882001, Roche) because present the lower activity compared to other collagenases we tested, and allow us to improve oocytes quality fulfilling our experimental requirements. During selection, we examined the membrane quality of the oocytes when they pass through a micropipette tip of the appropriate diameter. These modifications have increased our number of experimental success.
9. Vitelline membrane removal. Please note that we do not use hypertonic solutions to remove the vitelline oocyte membrane because this osmotic difference activates endogenous mechanosensitive ion channels [23–25].
10. An RNase free workstation and materials are very important to prepare RNA and maintain its integrity for oocytes injection. Carry out all steps involving transcription and RNA manipulation using gloves in an RNase-free bench dedicated for this purpose only. We wipe a cleaning solution all materials needed to do these steps including pipettes. For this purpose, we use RNase ZAP decontamination solution (cat# AM9780, Thermo Fisher Scientific, MA USA).
11. Temperature is determined automatically by the ramp program of the puller, according to filament resistance and glass capillary type.
12. Glup preparation, invented by Dr. Enrico Stefani. Mix 3 mL light mineral oil with 10 cm^2 Parafilm cut into small pieces. Heat the mixture to dissolve Parafilm obtaining a transparent preparation is achieved, then wait to room temperature solution and add the 2 mL of heavy mineral oil. After filling the patch-clamp pipette with the recording solution, immerse the pipette tip into Glup preparation with, for better patch clamp

seal [10]. (A good Glup should not change the original pipette resistance.).

13. Pulse duration must be as short as possible, to preserve membrane stability. We use pulse protocol with different durations: short pulses for extreme depolarization.
14. The pipette electrode is at room temperature, but the bath electrode is at different controlled temperatures. Therefore, the applied potentials need correction for temperature since the standard potential, E^0, of the Ag/AgCl electrode is temperature dependent [26]. $E^0 = 0.23695 - 4.8564 \cdot 10^{-4} t - 3.4205 \cdot 10^{-6} t^2 - 5.869 \cdot 10^{-9} t^3$. E^0 is in volts and the equation is good for $0 < t < 95$ °C. According to this equation the electrode asymmetry will be −11 mV at 0 °C, −6 mV at 10 °C, 0 mV at 20 °C, +7 mV at 30 °C, and +14 mV at 40 °C.
15. We calculate the variance using a method based on the differences between successive points along the isochrones [10, 27, 28]. This procedure is coded in analysis a computer program [2] gently provided by Dr. Francisco Bezanilla (University of Chicago).
16. Curve fitting minimizes the sum of squares of the residuals, that is, the difference between the experimental and the calculated values. To make sure to represent all the mean current values equally, we separated the mean current axis in 0.1 nA intervals and counted the number of samples in each bean. The weight applied to each squared error is the reciprocal value of the number of samples on each bean times the theoretical value of the parabola (*see* also Fig. 6).
17. We measure the G/G_{max} from the tail currents after depolarization to different voltages rather than from the steady-state condition. As shown by Diaz et al. and Cox et al. [29, 30] the tail current method avoids the artifacts introduced by slow and fast blocks.

Acknowledgments

We thank Miss Luisa Soto for excellent technical assistance, and Dr. Juan Pablo Castillo for his help to the noise analysis method. This work was supported by FONDECYT Grants 1150273 and 1190293 (to R.L.), 1180464 (to C.G.), 1180999 (to K.C), CONICYT-PFCHA/Doctorado Nacional/2017-21170395 (to E.C.). The Centro Interdisciplinario de Neurociencia de Valparaíso is a Millennium Institute (P09-022-F). This work was partially supported by the Air Force Office of Scientific Research under award number FA9550-16-1-0384 to R.L.

References

1. Raddatz N, Castillo JP, Gonzalez C et al (2014) Temperature and voltage coupling to channel opening in transient receptor potential Melastatin 8 (TRPM8). J Biol Chem 289:35438–35454. https://doi.org/10.1074/jbc.M114.612713
2. Starace DM, Bezanilla F (2004) A proton pore in a potassium channel voltage sensor reveals a focused electric field. Nature 427:548–553
3. Major N, Wassersug RJ (1998) Survey of current techniques in the care and maintenance of the African clawed frog (*Xenopus laevis*). Contemp Top Lab Anim Sci 37:57–60
4. Goldin AL (1992) Maintenance of Xenopus laevis and oocyte injection. Methods Enzymol 207:266–279
5. Reed BT (2005) Guidance on the housing and care of the African clawed frog (*Xenopus laevis*). Research animals department - RSPCA. Southwater, Horsham, West Sussex, UK
6. Green SL (2009) The laboratory Xenopus sp. CRC Press, Boca Raton, FL
7. Wu M, Gerhart J (1991) Raising Xenopus in the laboratory. Methods Cell Biol 36:3–18
8. Smith LD, Xu WL, Varnold RL (1991) Oogenesis and oocyte isolation. Methods Cell Biol 36:45–60
9. Alexander S, Bellerby C (1935) The effect of captivity upon the reproductive cycle of the South African clawed toad (*Xenopus laevis*). J Exp Biol 12(4):306–314
10. Morera F, Vargas G, González C et al (2007) Ion-Channel reconstitution. In: Dopico AM (ed) Methods in molecular biology, vol methods in membrane lipids, vol vol 400. Humana Press Inc., Totowa, NJ
11. Shih OM, Smith RD, Toro L et al (1998) High-level expression and detection of ion channels in Xenopus oocytes. Methods Enzymol 294:529–556
12. Goldin AL, Simkawa K (1992) Preparation of RNA for injection into Xenopus oocytes. Methods Enzymol 207:279–297
13. Krieg PA, Melton DA (1984) Functional messenger RNAs are produced by SP6 in vitro transcription of cloned cDNAs. Nucleic Acids Res 12:7057–7070
14. Stühmer W, Methfessel C, Sakmann B et al (1987) Patch clamp characterization of sodium channels expressed from rat brain cDNA. Eur Biophys J 13:131–138
15. Alvarez O, Gonzalez C, Latorre R (2002) Counting channels: a tutorial guide on ion channel fluctuation analysis. Adv Physiol Educ 26:327–341
16. Sigworth FJ (1980) The variance of sodium current fluctuations at the node of Ranvier. J Physiol 307:97–129
17. Poisson SD (1837) Probabilité des jugements en matière criminelle et en matière civile, précédées des règles générales du calcul des probabilitiés. Bachelie, Paris
18. Azzalini A (1985) A class of distributions which includes the normal ones. Scand J Stat 12:171–178
19. Ashour SK, Abdel-hameed MA (2010) Approximate skew normal distribution. J Adv Res 1:341–350
20. Yellen G (1984) Ionic permeation and blockade in Ca^{2+}-activated K^+ channels of bovine chromaffin cells. J Gen Physiol 84:157–186. https://doi.org/10.1085/jgp.84.2.157
21. Elsner HA, Honck HH, Willmann F et al (2000) Poor quality of oocytes from *Xenopus laevis* used in laboratory experiments: prevention by use of antiseptic surgical technique and antibiotic supplementation. Comp Med 50 (2):206–211
22. OConnell D, Mruk K, Rocheleau JM et al (2011) *Xenopus laevis* oocytes infected with multi-drug-resistant bacteria: implications for electrical recordings. J Gen Physiol 138 (2):271–277. https://doi.org/10.1085/jgp.201110661
23. Maroto R, Raso A, Wood TG et al (2005) TRPC1 forms the stretch-activated cation channel in vertebrate cells. Nat Cell Biol 7 (2):179–185. https://doi.org/10.1038/ncb1218
24. Yang XC, Sachs F (1990) Characterization of stretch-activated ion channels in Xenopus oocytes. J Physiol 431:103–122
25. Zhang Y, Hamill OP (2000) Calcium-, voltage- and osmotic stress-sensitive currents in Xenopus oocytes and their relationship to single mechanically gated channels. J Physiol 523 (Pt 1):83–99
26. Bard AJ, Parson R, Jordan J (1985) Standard potentials in aqueous solution. Marcel Dekker, Inc, New York
27. Heinemann SH, Conti F (1993) Nonstationary noise analysis and application to patch

clamp recordings. Methods Enzymol 207:131–148

28. Sigg D, Stefani E, Bezanilla F (1994) Gating current noise produced by elementary transitions in shaker potassium channels. Science 264:578–582
29. Cox DH, Cui J, Aldrich RW (1997) Separation of gating properties from permeation and block in *mslo* large conductance Ca-activated K channels. J Gen Physiol 109:633–646
30. Diaz F, Wallner M, Stefani E, Toro L et al (1996) Interaction of internal Ba^{2+} with a cloned Ca^{2+}-dependent K^{+} (hslo) channel from smooth muscle. J Gen Physiol (3):399–407. https://doi.org/10.1085/jgp.107.3.399